Surface Photovoltage Studies on Copper Gallium Selenide and Metal Oxides for Photoelectrochemical and Photocatalytic Solar Energy Conversion

By

YE CHENG

DISSERTATION

Submitted in partial satisfaction of the requirements for the degree of

DOCTOR OF PHILOSOPHY

in

Chemistry

in the

OFFICE OF GRADUATE STUDIES

of the

UNIVERSITY OF CALIFORNIA

DAVIS

Approved:

Frank E. Osterloh, Chair

Susan M. Kauzlarich

Jesús M. Velázquez

Committee in Charge

2022

Acknowledgements

Support for surface photovoltage measurements was provided by the U.S. Department of Energy, Office of Science, Office of Basic Energy Sciences, under award number DOE-SC0015329.

First and foremost, I would like to express my deepest gratitude to my advisor, Professor Frank Osterloh, for his invaluable guidance and continuous support throughout my PhD journey. I wanted to thank him for taking me into his research group, introducing me to the world of solar water splitting, and guiding me to grow as a graduate researcher. His immense knowledge, enthusiasm, honesty, and availability have supported me through six years of my academic research and graduate life. I am sincerely grateful for his mentorship. The experience I have gained through this journey is invaluable, and it would continuously encourage me in my future endeavors.

Besides, I would like to thank Professor Susan Kauzlarich and Professor Jesus Velazquez for their helpful advice during my PhD studies and for their services in my Dissertation Committee. I am also grateful to our research collaborators, Professor Julia Zaikina and Dr. Sangki Hong (Iowa State University), Professor Wouter Maijenburg and Dr. Behzad Mahmoudi (Martin Luther University Halle-Wittenberg, Germany), and Professor Roland Marschall (University of Bayreuth, Germany).

In addition, I would like to thank all the Osterloh group members, past and present. Special thanks to Dr. Zeqiong Zhao, Dr. Ruirui Han, Dr. Zongkai Wu, Dr. Rachel Doughty, Dr. Alex De Denko and Dr. Benjamin Nail for their guidance, selfless help, and continuous support. Many thanks to Samutr Assavachin and Chengcan Xiao for their warm emotional support. Their encouragement and companies during the journey are much appreciated. Many thanks to Hervin Errol Mendoza, Kathleen Becker, Anna Kundmann, Dr. Sahar Daemi and Dr. Sherdil Khan for their helpful discussion, beneficial collaboration, and kind support. I want to thank my undergraduate student Nhu Dang for her time and effort input. I also appreciate the support from Dr. Yaohang Gu, Dr. Zhiming Bai, Dr. Mauricio Alves De Melo Jr., Li Wang, Tatiana Mamani, Cassondra Brayfield, and Maria Kanwal.

I would also like to thank my friends, Dr. Yiqing Xia, Xiandong Meng, Dr. Binhan Hao, Dr. Zheng Ju and Dr. Jianheng Li for their companies during the graduate journey at UC Davis.

My acknowledgements would not be complete without thanking my mom Jiumei Ye and my dad Fangwu Cheng. Thank you for always standing by me and encouraging me to explore the world, I would never have made these accomplishments without your effort, support, and love.

Finally, thanks to my loving partner, Xuan Li, for your love and support over the past four years. It was my incredibly good fortune to meet you and love you, with our life journey crossing and joining together at Davis. Thank you for giving me another wonderful home. Your efforts have not gone unnoticed, and I have much to be thankful for.

Surface Photovoltage Studies on Copper Gallium Selenide and Metal Oxides for Photoelectrochemical and Photocatalytic Solar Energy Conversion

Abstract

Photoelectrochemical (PEC) and photocatalytic (PC) water splitting are potentially promising ways to achieve solar energy conversion with renewable hydrogen fuel to meet the growing global energy demand. However, solar to hydrogen efficiencies achieved in current systems are still far behind the target value to make the technology economically viable. In order to increase the efficiencies, developing narrow bandgap photocatalyst and deeper understanding of the photophysics is of great importance. Therefore, this dissertation focuses on study of photochemical charge separation and transport in copper gallium selenide and metal oxides semiconductor materials as a function of light intensity, photon energy and chemical environment. We hope the results from this study can promote the development of PEC and PC water splitting systems.

Chapter 2 employs liquid surface photovoltage (SPV) measurements combined with open circuit potential (OCP) measurements to investigate quasi-Fermi level splitting (QFLS) in $CuGa_3Se_5$ thin film photocathodes. Studies with different electrolyte contacts show that Fermi level pinning 0.5 eV above the valence band is the cause for the voltage loss during photoelectrochemical water and methyl viologen reduction. The effect of back contacts and CdS surface passivation layer on the QFLS of $CuGa_3Se_5$ thin film are also discussed. This work demonstrates a new approach to obtaining absolute minority carrier potentials in semiconductor/liquid junctions and identifying charge selective contacts and passivation layers.

Chapter 3 examines copper gallium selenide (CGSe) as a particulate photocatalyst for proton reduction. P-type CGSe particles were synthesized via solid-state method. With cocatalyst and sacrificial donor, $CuGa_3Se_5$ showed only mild activity for hydrogen evolution. Surface photovoltage spectroscopy (SPS) is used to monitor photochemical charge separation and transport in these materials for the first

time. The early photovoltage onset in SPS confirms interface/surface states in $CuGa_3Se_5$ particle films. SPS is also applied to study the effect of substrate/back contacts and electron transport layers on photochemical charge separation. A molybdenum back contact induced better charge carrier separation than fluorine-doped tin oxide (FTO). Nickel and TiO_2 were identified as electron selective contacts.

Chapter 4 employs surface photovoltage spectroscopy (SPS) and photoelectrochemical (PEC) methods to study the photochemistry of the metavanadates (CuV_2O_6, ZnV_2O_6 and $Zn_4V_2O_9$). SPS verifies the existence of sub bandgap states of V^{4+} in the vanadates and their negative effect on the photovoltage and the PEC performance. Additionally, photochemical charge separation and the role of the space charge region (SCR) in $CaFe_2O_4$ particle films are investigated.

Table of Contents

Acknowledgements ii

Abstract iv

Table of Contents vi

List of Abbreviations viii

Chapter 1 Introduction 1

Fuel from Water Splitting 1

Photocatalytic Water Splitting 2

Photoelectrochemical (PEC) Water Splitting, Photovoltage and Quasi-Fermi Levels 6

Surface Photovoltage (SPV) 11

References 16

Chapter 2 Liquid Surface Photovoltage Reveals Effects of Substrates and Passivation Layers on Quasi-Fermi Level Splitting of $CuGa_3Se_5$ Thin Film Photocathodes for Proton and Methyl Viologen Reduction 27

Introduction 27

Results and Discussion 30

Conclusions 47

Experimental Section 48

Appendix 50

References 52

Chapter 3 Factors Limiting p-type Copper Gallium Selenide as a Particulate Photocatalyst for Hydrogen Evolution 58

Introduction 58

Results and Discussion 60

Conclusions 75

Experimental Section 76

Appendix 79

References 79

Chapter 4 Surface Photovoltage Spectroscopy and Photoelectrochemical Studies on Metavanadates (CuV_2O_6, ZnV_2O_6 and $Zn_4V_2O_9$) and Calcium Ferrite ($CaFe_2O_4$) 86

Introduction 86

Results and Discussion 87

Conclusions 94

Experimental Section 95

Appendix 97

References 100

List of Abbreviations

AQY	apparent quantum yield
CBD	chemical bath deposition
CGSe	copper gallium selenide; refers to $CuGa_3Se_5$ specifically in Chapter 2
CPD	contact potential difference
EDX	energy dispersive X-ray spectroscopy
E_f	Fermi energy
$E_{f,\,n}$	quasi-Fermi energy of electrons
$E_{f,\,p}$	quasi-Fermi energy of holes
E_G	bandgap energy
LSV	linear sweep voltammetry
NHE	normal hydrogen electrode
OCP	open circuit potential
PEC	photoelectrochemical
PXRD	powder X-ray diffraction
QFLS	quasi-Fermi lever splitting
RHE	reversible hydrogen electrode
SCR	space charge region
SEM	scanning electron microscopy
SPS	surface photovoltage spectroscopy
SPV	surface photovoltage
STH	solar-to-hydrogen conversion efficiency
V_{ph}	photovoltage

Chapter 1 Introduction

Fuel from Water Splitting

The ongoing increase in global energy demand and the unprecedented impact of human activity on climate change have made the development of carbon-neutral energy sources ever more critical. With solar as a renewable and the most abundant energy source and hydrogen as a clean and versatile energy carrier, solar water splitting is a promising way to counter the climate change and energy crisis.[1-2] Solar water splitting, using solar energy to split water into hydrogen and oxygen gas (**Eq 1.1**), with the solar energy stored in the bond rearrangement. Fujishima and Honda first demonstrated this in 1970s with an illuminated single-crystal TiO_2 electrode.[3]

$$H_2O(l) \rightarrow H_2(g) + \tfrac{1}{2} O_2(g) \qquad \Delta G^0 = +237\ kJ \cdot mol^{-1} \qquad (1.1)$$

Solar water splitting can be generally categorized into three types: photovoltaic-assisted electrolysis (PV-E), particulate photocatalysis (PC), and photoelectrochemical (PEC) water splitting. The PV-E approach is at a much higher technological readiness level due to the maturity of both PV and electrolyzer technologies.[4] A technoeconomic analysis in 2016 by Shaner el at. pointed out that this process is not cost-competitive with electrolysis powered by nuclear or thermal power plants using present-day technology, even taking into account that such systems have shown solar-to-hydrogen (STH) conversion efficiencies higher than 20%.[5] Considering that lower technological maturity offers ample space for innovation, PEC and particulate photocatalysts (PC) systems are predicted to be more promising for the long-term goal of achieving hydrogen production costs competitive with fossil-fuel derived hydrogen.[2, 4-5] In the technoeconomic analysis conducted by Pinaud et al. in 2013, the baseline levelized cost of hydrogen production by those systems are calculated.[6] It was estimated to be \$1.60 -3.20 kg^{-1} for particle suspension systems (assuming STH values of 5-10% and an expected lifetime of 5 years) and \$4.10-10.40 kg^{-1} for PEC systems (assuming STH values of 10-15% and an expected lifetime of 10 years). With the targeted hydrogen price of 2.10 kg^{-1} set by the U.S. Department of Energy, particulate

photocatalytic systems show the potential to meet the requirements because of the low material, construction and operation cost.[7] Recently, the Domen group reported safe photocatalytic solar hydrogen production from water on a 100-m^2 array of panel reactors based on modified Al:$SrTiO_3$ particulate photocatalyst over several months with autonomous recovery of hydrogen from the moist gas product mixture using a commercial polyimide membrane, with maximum STH of 0.76%.[8] While the project successfully demonstrated safe and large-scale photocatalytic water splitting with gas collection and separation, the obtained STH is still behind the target value. To make the technology economically viable, improving the STH efficiency and photocatalyst stability are part of the essential steps. So, deeper understanding and more rational design and construction of highly efficient water-splitting photocatalysts are needed.[9-10]

Photocatalytic Water Splitting

Overall water splitting consists of a proton reduction half reaction and an oxygen evolution half reaction:

Hydrogen evolution reaction (HER): $2H^+ + 2e^- \rightarrow H_2$ 0 V vs RHE (1.2)

Oxygen evolution reaction (OER): $H_2O \rightarrow ½\ O_2 + 2H^+ + 2e^-$ + 1.23 V vs RHE (1.3)

Overall water splitting: $H_2O \rightarrow H_2 + ½\ O_2$ −1.23 V (1.4)

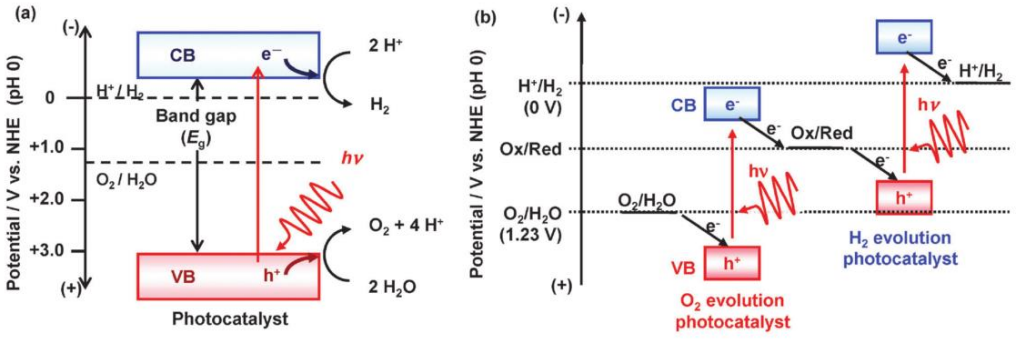

Figure 1.1 Energy diagrams of photocatalytic water splitting based on (a) one-step excitation and (b) two-step excitation (Z-scheme). Reprinted with permission from ref.[11] Copyright 2014, Royal Society of Chemistry.

Photocatalytic systems can employ single- or dual-absorber (tandem/ Z-scheme) systems to split water (**Figure 1.1**). In the single-absorber system, the HER and OER reactions occur on the same particle, whereas in the dual-absorber system, the H_2 evolution photocatalyst (HEP) and O_2 evolution photocatalyst (OEP) are connected in series with reversible redox shuttles or solid interface.[11] Upon absorption of a photon with energy greater than the bandgap, an electron is excited from the valence band to the conduction band, generating an electron-hole pair. The electron diffuses from the conduction band to the reduction cocatalyst, where the HER takes place, and the hole diffuses from the valence band to the oxidation cocatalyst, where the OER takes place. For the single-absorber system, the conduction and valence bands of the semiconductor must straddle the thermodynamic potentials for both HER and OER reactions to accomplish overall water splitting (**Figure 1.1a**). In the dual-particle system, the constraints are relaxed, as the voltages of both HEP and OEP sum to provide the driving force for overall water splitting (**Figure 1.1b**). This allows the utilization of photocatalysts with smaller bandgaps to harvest more solar irradiation.

Researchers from the Domen lab currently hold the record efficiency (STH exceeding 1.0%) on particle tandem systems with their photocatalyst sheet comprising HEP of La and Rh co-doped $SrTiO_3$ and OEP of Mo doped $BiVO_4$ embedded in gold or carbon layer.[12-13] Their Cr_2O_3/Ru modified $SrTiO_3$:La,Rh/C/$BiVO_4$:Mo photocatalyst sheet achieved an STH of 1.0% during unassisted overall pure-water (pH 6.8) splitting at a temperature of 331 K and a pressure of 91 kPa, which are close to practical operating conditions.[13] The apparent quantum yield (AQY) of the system was reported to be 26% at a wavelength of 419 nm.

To meet the target STH of 10%, there is high demand for the development of narrow bandgap materials with an operable wavelength range up to 600–700 nm together with an AQY of 40–60%.[10] Some particulate photocatalysts such as (oxy)nitrides and (oxy)chalcogenides were shown to be applicable to water splitting under visible light.[14-19] However, the efficiency in such materials is currently very low. For example, $LaMg_{1/3}Ta_{2/3}O_2N$ with appropriate surface modifications splits water under

irradiation at wavelengths up to 600 nm, while the AQY value is only 0.18% at 440 nm.[15-16] In addition, improvement in the lifetimes of these photocatalytic systems is needed.

It appears that particulate semiconductor materials with narrow band gaps are typically poorly crystallized and often defective due to the synthesis difficulty.[2] This results in a high concentration of defect states, which generally enhance the charge recombination and deteriorate the photocatalysis performance. Several of the main desired requirements for utilizing those materials are synthesis methods giving well-crystallized materials with low bulk defect densities, effective engineering of the photocatalysts/cocatalysts interfaces and surface modification methods to passivate surface defects. For example, the Domen group reported a particulate solid solution of zinc selenide and copper gallium selenide (ZnSe:CGSe) that evolves H_2 efficiently and is responsive to visible light up to 725 nm.[20] With the preparation of single-crystalline particles and the rational assembly of Ni-Ru composite cocatalysts, an AQY of 13.7% was obtained at 420 nm during a sacrificial H_2 evolution reaction, which is approximately 27 times higher than the value they previously reported for this material (0.5% at 420 nm),[21] representing the highest AQY yet obtained using a 700 nm-class photocatalyst.

In 2020, almost unity internal quantum efficiency (at 350-360 nm) was achieved in a modified Al-doped $SrTiO_3$ photocatalyst, by applying aluminum doping for defect suppression,[22-24] flux treatment to improve the crystallinity,[22, 25] facet engineering with selective deposition of HER and OER cocatalysts, and a Cr_2O_3 shell to inhibit the backward reaction,[26] thus demonstrating the feasibility of overall water splitting free from charge recombination losses.[27] With this finding by the Domen group as a shot in the arm and emerging research worldwide in this field, we believe that efficient charge separation and transport (AQY >20%) could be achieved in a broader range of materials in the near future. To promote the development, more profound understanding of the charge separation processes in semiconductors materials is of great importance. This work will attempt to address these issues by providing information about charge separation and transport within semiconductor films and particles.

In Chapter 3, we examine copper gallium selenide (CGSe) as a particle photocatalyst. CGSe is a wide bandgap (~ 1.5-1.9 eV) material, that belongs to the class of chalcopyrite $Cu(In,Ga)(Se,S)_2$ (CIGS) absorbers, which feature tunable band structure and high absorption coefficients.[28-31] While showing promising PEC performance,[32-33] there is only one report on the use of CGSe as HER photocatalysts (7 $\mu mol \cdot h^{-1}$ H_2 evolution for $CuGa_5Se_8$ with sulfide and sulfite ions as sacrificial electron donors.)[19] This is only a small fraction of the theoretical performance of this material. Questions still remain about the charge separation abilities in these materials. To study these questions, this work will employ surface photovoltage spectroscopy (SPS) to observe the carrier dynamics in these materials and to gain more information about the defect states. The use of charge selective contacts to promote carrier separation will also be examined for the particle films.

In Chapter 4, photochemical charge separation of metavanadates (CuV_2O_6, ZnV_2O_6 and $Zn_4V_2O_9$) and $CaFe_2O_4$ was investigated. Because of their low cost and chemical stability, transition metal oxide are receiving increasing interest for the application of PEC water splitting.[34-37] With suitable band edge positions for PEC water oxidation, photochemistry of metavanadates (CuV_2O_6, ZnV_2O_6 and $Zn_4V_2O_9$), that synthesized via a deep eutectic solvent (DES) synthesis route,[38-39] will be studied with SPS and PEC method. Similarly, p-type $CaFe_2O_4$ with a bandgap of 1.9 eV belongs to the class of ferrites, which is recently been explored owing to their abundance, nontoxicity, and intrinsic stability in aqueous solutions.[40] Because the conduction band edge of $CaFe_2O_4$ is more reducing than water reduction potential, it has been investigated for PEC water reduction.[41-43] However, the achieved PEC performance is much limited by the high charge recombination rate of the $CaFe_2O_4$,[44] and only one photocatalytic hydrogen evolution of $CaFe_2O_4$ particle suspensions (with methanol sacrificial donor, AQY 1.57 %) can be found in the literature.[45] Therefore, this work will employ SPS to study the photophysics of $CaFe_2O_4$ that was synthesized by a facile solution-based microwave reaction method.[46] Observations of the space charge region in the particle films will be discussed.

Photoelectrochemical (PEC) Water Splitting, Photovoltage and Quasi-Fermi Levels

While the particle photocatalytic systems may be more cost effective in the long term, it was argued that thin film-based PEC technology that leverages current semiconductor manufacturing knowledge is likely to succeed in the medium term (~10 years).[4] Because the underlying photophysics are shared among systems, insights gained in one field can benefit the other.[47] For thin-film-based systems, the illumination conditions can be more easily controlled, and there is more flexibility in spectroscopic and operando (non-equilibrium) characterizations.[48] This allow us to characterize the materials using various techniques to understand each material's underlying photophysical and photochemical properties, thereby providing opportunities for rapidly improving efficiency and stability.

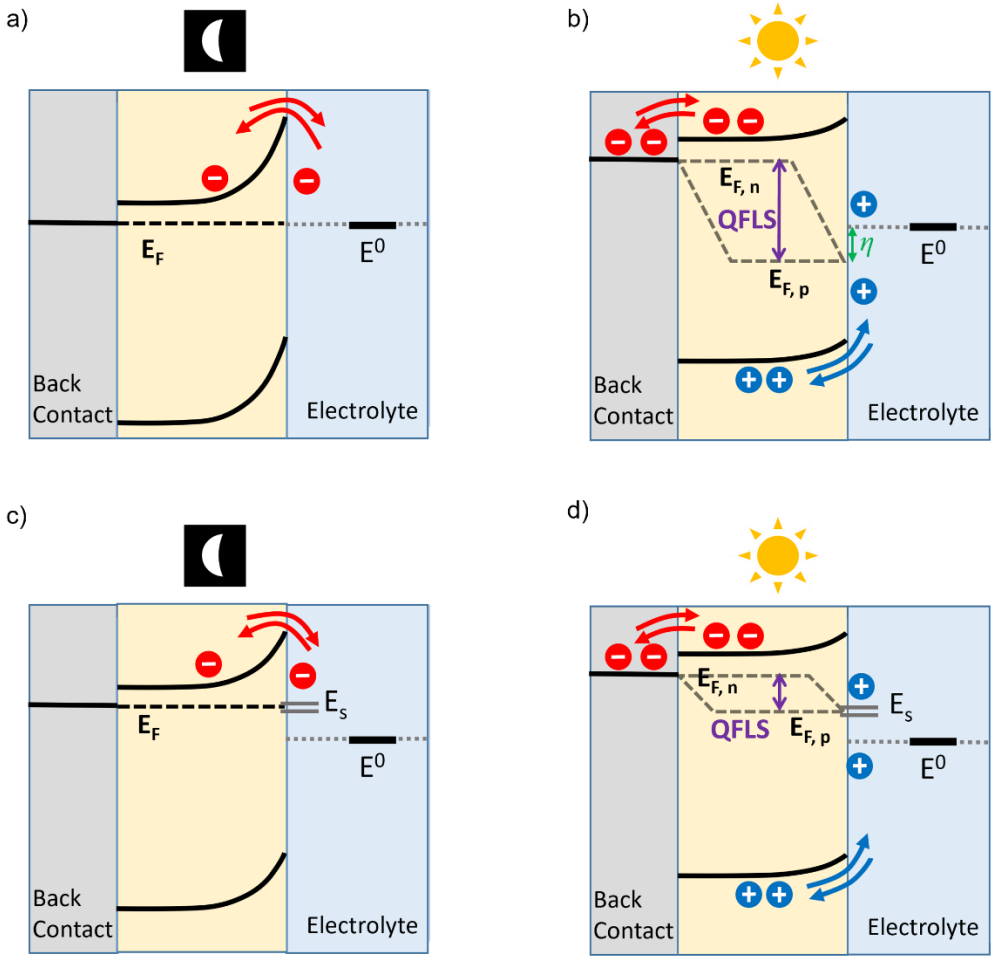

Figure 1.2 Energetics and charge carrier dynamics of a p-type semiconductor-liquid junction, in the dark and under illumination. Quasi-Fermi levels, $E_{F,n}$ and $E_{F,p}$, are shown together with the standard reduction potentials of the solution E^0 and the surface states E_s. (a)(b) In the ideal case of $E_{F,dark} = E^0$, the band bending is controlled by electrolyte potential in the dark. QFLS: quasi-Fermi level splitting under illumination. $\eta = E_{F,p} - E^0$, serves as extra driving force that overcomes the kinetic overpotential. (c)(d) Surface states pinning the E_F in the dark and controlling the band bending. Surface states serve as electron hole recombination centers under illumination, thus limiting the QFLS.

The performance of a photoelectrode depends critically on the nature of the semiconductor/liquid junction. For the ideal case, Fermi level (E_F) of the semiconductor is fixed to the electrochemical potential of contacting electrolytes at dark equilibrium (**Figure 1.2a**). Upon illumination (**Figure 1.2b**), the electron and hole concentrations at the semiconductor/liquid junction are under quasi-equilibrium conditions. The electrochemical potentials of the electrons and holes are expressed by their quasi-Fermi levels ($E_{F,n}$ and $E_{F,p}$), the difference of which, the quasi-Fermi level splitting (QFLS), corresponds to the photovoltage (V_{ph}) of the semiconductor liquid junction.[49-51] As addressed by Lewis and coworkers, this quasi-equilibrium is governed by several kinetic processes at the junction as shown in **Figure 1.3**, with description in the figure legend.[52-53]

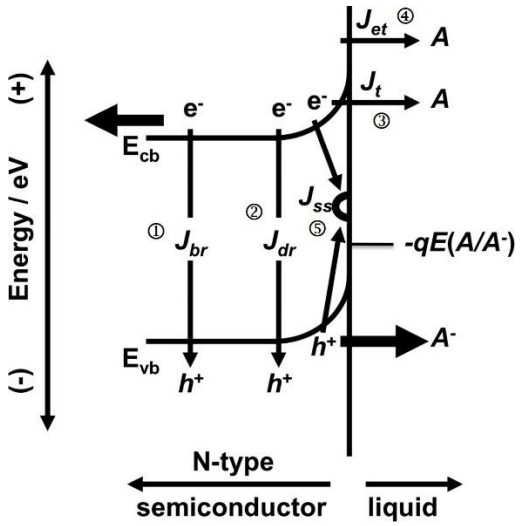

Figure 1.3 Schematic of a typical n-type semiconduction/liquid junction under illumination, showing the recombination pathways (thin arrows) for photoexcited carriers. These are ① recombination in the bulk (J_{br}), ② recombination in the depletion-region (J_{dr}), ③ tunneling through the electric potential barrier near the surface (J_t), ④ thermionic emission (J_{et}), and ⑤ recombination at surface defect states (J_{ss}). Electron collection by the back contact and hole collection by the redox couple are processes that contribute positively to device efficiency (depicted by thick black arrows). Adapted with permission from ref.[52-53] Copyright 2005, American Chemical Society.

It was pointed out that when any of these recombination rates are significant, the photovoltage will be limited.[52] One of the most recognized phenomena cause by the surface states is Fermi level pinning,[54] which has been documented for many semiconductors electrodes.[55-60] This results in $E_{F,\ dark}$ pinned to the surface states level, and controls the band bending (**Figure 1.2c**). These trap states could also act as recombination center, thus limiting the QFLS under illumination (**Figure 1.2d**). This will be further discussed in detail in Chapter 2 which describes QFLS results for $CuGa_3Se_5$ thin film photocathodes.

The performance of photoelectrodes is usually characterized with (applied) potential-current measurements under light illumination, as shown in **Figure 1.4** for a photocathode and photoanode.[52] For an ideal (no overpotential) but photo-inactive anode, electrochemical water oxidation will start when the applied potential is more positive than 1.23 V_{RHE} (grey curve on the right side in **Figure 1.4**). When a photoanode is used under illumination, the generated photovoltage will contribute thermodynamically and it requires less applied potential to oxidize water, thus leading to a cathodic shift of the current-potential curve (blue curve in **Figure 1.4**). Same principle works for the photocathode. A dual-absorber 'tandem' PEC device combines the separate electrodes in series.[61-62] In this arrangement photocathode and photoanode contribute additive photovoltages that drives the PEC overall water splitting. It is also worth to point out that overall water splitting activity of a tandem particle PC system is strongly correlated with the activity of the photocatalyst as a (particle-based) photoelectrode rather than as suspended

photocatalyst with sacrificial agent, as indicated by researchers in the Domen group with several studies on oxysulfide-based or metal selenide-based photocatalyst sheet systems.[19, 21, 63-64]

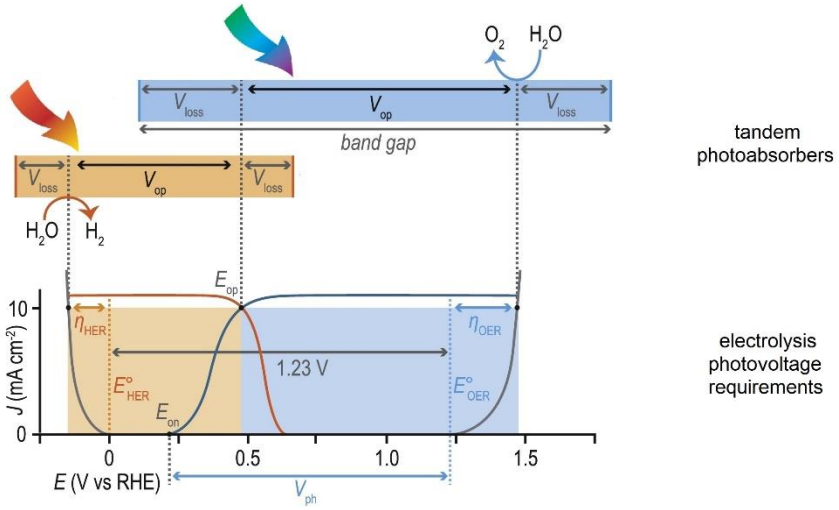

Figure 1.4 (a) Schematic relating band gaps and photovoltages in an idealized two-absorber tandem PEC device in which the photoanode is the top absorber. Free energy losses in each absorber (V_{loss}) and catalytic overpotentials for each half-reaction (η) are fundamental loss pathways. Current-potential curves for electrocatalysts (grey) and an idealized PEC photoanode (blue) and photocathode (orange) are shown with their relative power contributions (shaded areas) in an ideal tandem. Adapted with permission from ref.[61] Copyright 2017, Elsevier.

To assess the energy conversion efficiency of the system, it is crucial to understand the photovoltage, as a key property, of the individual photoelectrodes. However, the true photovoltage (V_{ph}), or quasi-Fermi level splitting (QFLS) energy at a single electrode is difficult to measure experimentally because of the lack of a direct electric contact to the semiconductor-liquid interface. Instead, the convention is to estimate the photovoltage from the difference between the photocurrent onset potential (E_{on}) and the Nernst potential for the targeted redox reaction (E^0, 0 V_{RHE} for HER and 1.23 V_{RHE} for OER), as shown in **Figure 1.4a**. This analysis ignores catalytic overpotentials (η). This brings some errors, especially for photoanodes due to the large η for oxygen evolution.[65] In addition, the determination of E_{on} is not always applicable, or sometime can be arbitrary, for systems that have competing redox

process, like photo corrosion, happening at the correspond potential.[52] Another method to estimate the V_{ph} is to measure the voltage difference of the illuminated photoelectrode versus a counter electrode in a electrochemical cell.[52] However, this method assumes that both electrodes are in rapid charge transfer equilibria with a certain redox couple in the electrolyte, which is not applicable when slow redox couples (H^+/H_2, O_2/H_2O) encountered or when there are multiple redox couples involved.[66] The catalytic overpotentials are also ignored in this method.

As mentioned, difficulties to measure the true V_{ph}, or QFLS, mainly originate from the accessibility of the quasi-Fermi level of the minority carriers (e.g., $E_{F,\,p}$ for a n-type semiconductor) due to the lack of a direct electrical connection to the solid-liquid interface. These limitations have been addressed and partially solved by Boettcher and coworkers. They introduced dual-working-electrode (DWE) techniques and/or applied atomic force microscopy (AFM) to the electrochemical measurements with demonstration on TiO_2, hematite, $BiVO_4$ and Si based photoelectrode.[67-72] Through surface deposition of a thin, electrolyte-permeable gold layer, which is the second working electrode, the local electrochemical potential of the surface is measured by a second potentiostat as one approach.[67-68] In another approach, potential-sensing electrochemical atomic force microscopy (PS-EC-AFM) is used in contact with the catalyst layer.[69-72] This allows the direct measurement of surface electrochemical potential in heterogeneous electrochemical systems in operando. Though examined examples in above studies all have redox-active Ni, Co or Fe based (co)catalysts on electrode surface, the authors noted that the measurement techniques will work equally well on any catalytic material that is electronically conductive and therefore amenable to potential sensing.[71]

Recently our group developed an alternative, contact-less and non-invasive method for the determination of the QFLS, using liquid surface photovoltage (SPV) spectroscopy on $BiVO_4$, GaP and $CuGa_3Se_5$ photoelectrodes (unpublished results). In Chapter 2, this technique will be applied to $CuGa_3Se_5$ thin films. This material recently emerged as a promising wide bandgap (~1.84 eV) absorber for the top cell (photocathode for HER) in tandem PEC devices.[73-76] While high photocurrent (~12 $mA \cdot cm^{-2}$ at -1

V_{RHE}) with excellent stability (17 days) were achieved,[73] the reported photo-onsets of bare $CuGa_3Se_5$ photocathodes are less positive than 0.3 V_{RHE},[73, 76] which represents a substantial photovoltage loss. In order to study the origin of the voltage loss this work employs photoelectrochemical measurements together with liquid SPV on thin film $CuGa_3Se_5$ photocathodes in contact with different electrolytes, back contacts and a CdS passivation layer.

Surface Photovoltage (SPV)

The surface photovoltage (SPV) method is known as a highly sensitive and non-destructive technique for semiconductor characterizations that relies on analyzing illumination induced changes in the surface voltage.[77-78] Starting from the work of Brattain and Bardeen in the late 1940s and early 1950s,[79-80] it was further developed in the early 1970s, when systematic research on the effects of sub-bandgap illumination on the surface voltage took place by Harry Gatos and Jacek Lagowski at MIT.[81] Since then, SPV has been used as a comprehensive source of surface and bulk information on various semiconductors and semiconductor interfaces.

One of the most widely used experimental methods to carry out SPV measurements is the vibrating Kelvin probe (VKP) technique.[77-78] **Figure 1.5** shows a photo of the experiment set-up in this study and a schematic configuration of the vibrating Kelvin probe surface photovoltage (VKP-SPV) measurement. In VKP-SPV, the contact potential difference (CPD) is measured between a sample and a semi-transparent gold Kelvin probe placed approximately 1-2 mm above the sample.

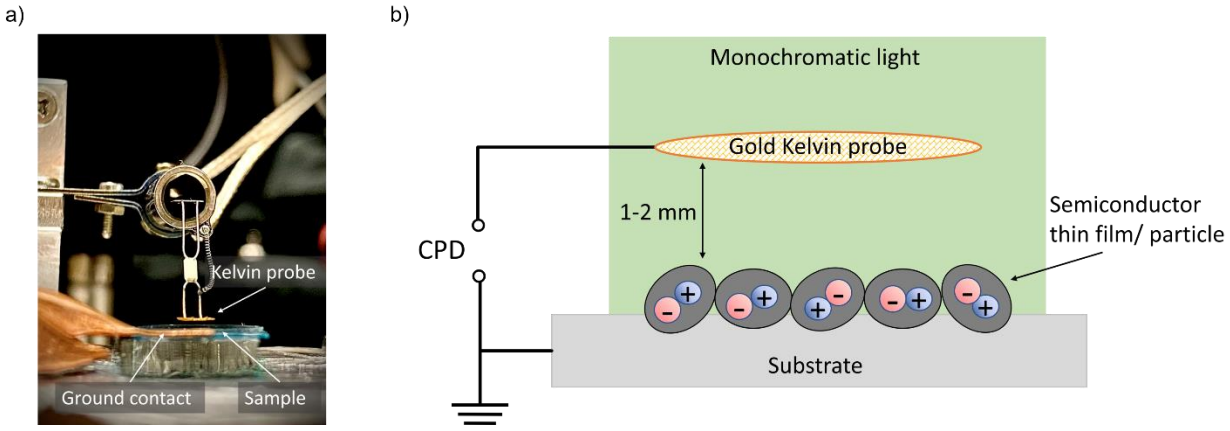

Figure 1.5 Vibrating Kelvin probe surface photovoltage (VKP-SPV) measurement. (a) Photo and (b) schematic of the measurement configuration. CPD: contact potential difference. SPV = ΔCPD = CPD (light) – CPD (dark).

The principle of the Kelvin probe technique is illustrated in **Figure 1.6** and described as following. Initially, the bare sample electrode and the reference electrode (gold Kelvin probe) are characterized by their work functions W_s and W_{ref}, respectively (**Figures 1.6a**). When the sample and reference electrodes are electrically connected (**Figure 1.6b**), electrons flow from the electrode with the lower to the electrode with the higher work function. The Fermi energies of the sample ($E_{F,\,s}$) and reference ($E_{F,\,ref}$) electrodes change until one common Fermi energy (E_F) is established. The two electrodes then no longer have the same local vacuum level (electric potential or Galvani potential). The corresponding potential drop between the two electrodes equals the contact potential difference (CPD).

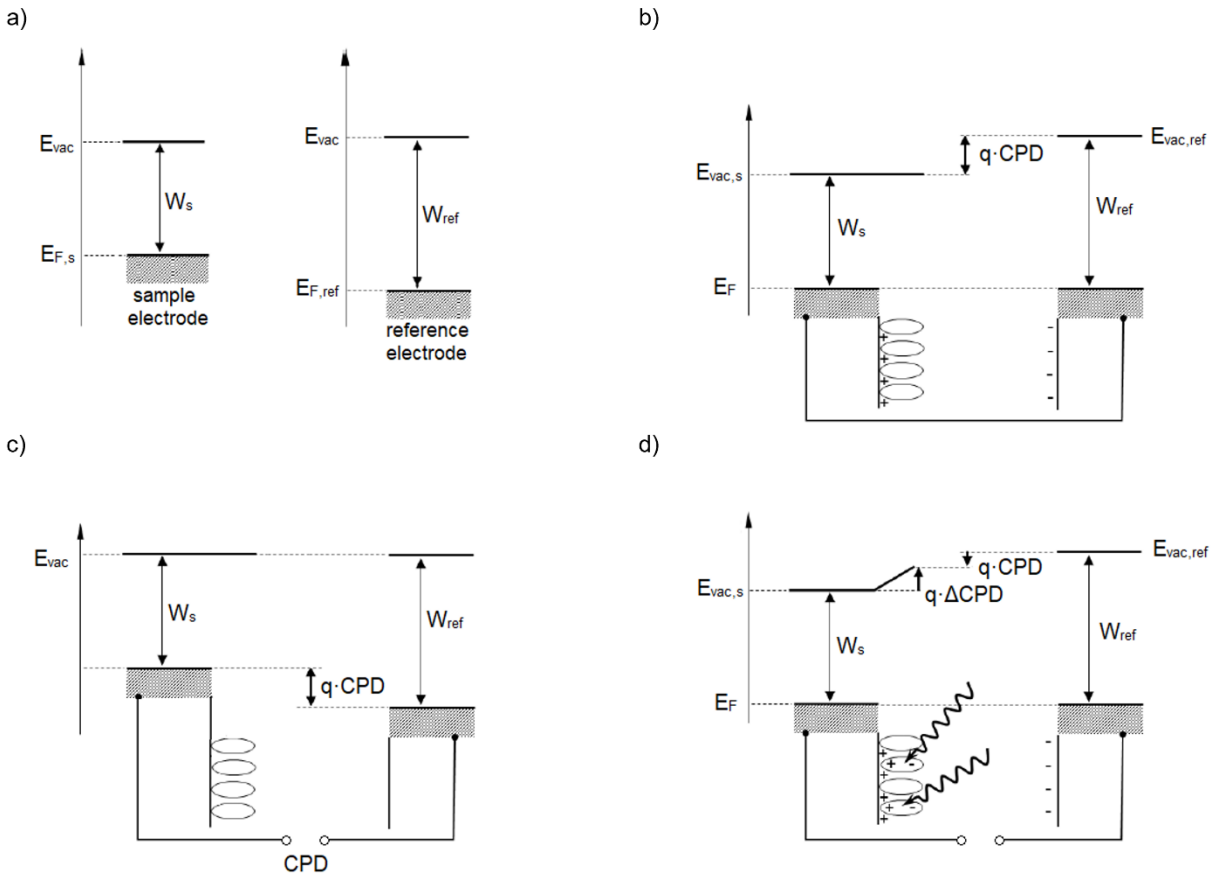

Figure 1.6 Schematic diagram of energies illustrating the CPD measurements in the VKP-SPV technique. (a) Isolated bare sample electrode and reference electrode (Kelvin probe). (b) Electrically connected sample and reference electrodes. (c) Sample and reference electrodes connected through a DC bias equal and opposite to the contact potential difference. (d) Electrically connected (photoactive) sample and reference electrodes under illumination. ΔCPD denotes the change of the CPD due to the separation of photogenerated charge carriers in space. Figures are adapted with permission from reference.[77] Copyright 2020, World Scientific Publishing Co., Inc.

The CPD value is measured experimentally by vibrating the Kelvin probe and following the small AC current that flows between the two electrodes, resulting from the changing capacitance of the sample-probe configuration. Through application of an external DC bias, equal and opposite to the CPD (**Figure. 1.6c**), the AC current becomes zero, and the CPD can be observed from the necessary bias voltage.

In SPV, the light induced CPD change under illumination is the main interest. When the sample is illuminated, photogenerated charge carriers are separated in space, for example, photogenerated holes and electrons move towards the sample substrate and the sample surface, respectively (**Figure 1.6d**). This creates an electrostatic potential in the region of the photoactive layer, which changes the work function of the sample electrode. This results in a CPD change (ΔCPD) compared to the dark condition, with the surface photovoltage (SPV) determined as:

$$SPV = \Delta CPD = CPD\ (light) - CPD\ (dark)$$

As the SPV signal is caused by the photogenerated charge carriers via light absorption and their following spatial redistribution, the technique is sensitive not only to the 'surface', but to the entire surface space charge region (via super- or sub-bandgap absorption), to the quasi-neutral bulk (via the Dember effect) and even to buried interfaces located within the sample.[78]

One specific SPV method variant is surface photovoltage spectroscopy (SPS), in which SPV is monitored as a function of incident photon energy.[82] Through analysis of the spectra, useful information about the semiconductor properties can be extracted. These properties include, but are not limited to, bandgap, majority carrier type, and its (surface and bulk) defect states. This provides essential information to construct surface and interface band diagrams of semiconductors.

SPS has been used in the Osterloh lab since 2013 to study the photochemical charge separation in water splitting semiconductor photocatalysts.[24, 83-91] For example, Jing Zhao et al. used SPS to investigate the charge transfer processes in nanocrystal $HCa_2Nb_3O_{10}$ films; variations in the density of states of the nanocrystals were observed, as well as effects resulting from surface defects, molecular adsorbates, and interfacial electron transfer barriers.[84] Their study on the CdSe quantum dots further demonstrated the ability of SPS to measure built-in voltages, space charge region (SCR) thickness and sub-band gap states in drop-cast quantum dot films.[85] A more systematic SPS study on the SCR in nano- and microparticle of $SrTiO_3$ and GaAs on gold substrate was carried out by Rachel Doughty et al.; they found that the observed depletion layer width in particle films exceeded the theoretical value by 1~3 orders of

magnitude, which is attributed to the surface states that controls band bending and photochemical charge separation.[86] SPS is especially useful for studying the mid-gap states induced or suppressed in doped semiconductors. For example, studies by Xiaoqing Ma et al. used SPS to locate the dopant levels and defect states in transition metal doped $SrTiO_3$.[87-88] SPS studies on Al-doped $SrTiO_3$ nanocrystals by Zeqiong Zhao et al. confirmed that aluminum doping enhances photochemical charge separation and reduces electron and hole trapping from the elimination of Ti^{3+} states.[24, 89] SPS could also be used in the study of heterostructures. For example, a study by Zongkai Wu et al. used SPS to investigate photochemical charge transfer at the interfaces of Cu_2O and $BiVO_4$ nanoparticles; they found evidence for tandem excitation, demonstrating the possibility of a water splitting system based on a $BiVO_4$-Cu_2O direct contact particle tandem.[90] SPS was also utilized in the study of charge transfer in dye-sensitized solar cells (DSSC) by Ruirui Han et al.; they found that efficiency and reversibility of electron transfer at the conductive substrate - electron transfer layer - dye interface are essential for DSSC performance.[91] Ferroelectric enhanced charge separation was studied with SPS by Samutr Assavachin et al. as well; anomalous surface photovoltage up to -6.3 V was observed in Cr-doped $SrTiO_3$ nanocrystals.[92]

As mentioned above, our group developed a liquid SPV method recently (unpublished results). The measurement configuration is very similar to the vacuum SPV (**Figure 1.5**), except for the addition of a liquid electrolyte drop plus a piece of microscope glass on the sample electrode and beneath the Kelvin probe. Because the semiconductor is in contact with the electrolyte, the SPV signal is different from those measured in vacuum,[77-78] and reports on quasi-Fermi level splitting (QFLS) of the semiconductor/liquid junction.

In Chapter 2, the liquid SPV technique is applied to $CuGa_3Se_5$ thin film photocathodes in order to examine the reason for the photovoltage loss observed with $CuGa_3Se_5$/liquid contacts. The effects of the electrolyte, substrate, and surface passivation layer on the QFLS will be described. This provides new insight into the factors that limit the performance of this photoelectrode material. In Chapter 3 of this work, we use SPS to examine the photochemical charge separation properties in copper gallium selenide

(CGSe) particle films with various charge selective contacts/layers. Through detailed analysis of the spectra, we identify the energy levels of the surface states in CGSe particles and reveal the possible reason for the low H_2 evolution activity. SPS results with different charge selective contacts/layers provide ideas for optimizing the photocatalyst in future work. In Chapter 4 of this work, SPS is used to observe charge separation in zinc-rich metavanadate ($Zn_4V_2O_9$) and calcium ferrite ($CaFe_2O_4$) particle films. Here, SPS is used to observe the sub-band gap states in $Zn_4V_2O_9$, which is correlated with its photoelectrochemical performance. We also use SPS to observe charge separation and space charge region in $CaFe_2O_4$ particle films with various thicknesses. This contributes to a better understanding of photochemical charge separation in chalcopyrite and metal oxide semiconductor photoelectrodes and photocatalysts systems and promotes their use for solar fuel generation.

References

1. Kim, J. H.; Hansora, D.; Sharma, P.; Jang, J.-W.; Lee, J. S., Toward practical solar hydrogen production – an artificial photosynthetic leaf-to-farm challenge. *Chemical Society Reviews* **2019,** *48* (7), 1908-1971.

2. Hisatomi, T.; Domen, K., Reaction systems for solar hydrogen production via water splitting with particulate semiconductor photocatalysts. *Nature Catalysis* **2019,** *2* (5), 387-399.

3. Fujishima, A.; Honda, K., Electrochemical Photolysis of Water at a Semiconductor Electrode. *Nature* **1972,** *238* (5358), 37-38.

4. Ardo, S.; Fernandez Rivas, D.; Modestino, M. A.; Schulze Greiving, V.; Abdi, F. F.; Alarcon Llado, E.; Artero, V.; Ayers, K.; Battaglia, C.; Becker, J.-P.; Bederak, D.; Berger, A.; Buda, F.; Chinello, E.; Dam, B.; Di Palma, V.; Edvinsson, T.; Fujii, K.; Gardeniers, H.; Geerlings, H.; H. Hashemi, S. M.; Haussener, S.; Houle, F.; Huskens, J.; James, B. D.; Konrad, K.; Kudo, A.; Kunturu, P. P.; Lohse, D.; Mei, B.; Miller, E. L.; Moore, G. F.; Muller, J.; Orchard, K. L.; Rosser, T. E.; Saadi, F. H.; Schüttauf, J.-W.; Seger, B.; Sheehan, S. W.; Smith, W. A.; Spurgeon, J.; Tang, M. H.; van de Krol, R.; Vesborg, P. C.

K.; Westerik, P., Pathways to electrochemical solar-hydrogen technologies. *Energy & Environmental Science* **2018,** *11* (10), 2768-2783.

5. Shaner, M. R.; Atwater, H. A.; Lewis, N. S.; McFarland, E. W., A comparative technoeconomic analysis of renewable hydrogen production using solar energy. *Energy & Environmental Science* **2016,** *9* (7), 2354-2371.

6. Pinaud, B. A.; Benck, J. D.; Seitz, L. C.; Forman, A. J.; Chen, Z.; Deutsch, T. G.; James, B. D.; Baum, K. N.; Baum, G. N.; Ardo, S.; Wang, H.; Miller, E.; Jaramillo, T. F., Technical and economic feasibility of centralized facilities for solar hydrogen production via photocatalysis and photoelectrochemistry. *Energy & Environmental Science* **2013,** *6* (7), 1983-2002.

7. Fabian, D. M.; Hu, S.; Singh, N.; Houle, F. A.; Hisatomi, T.; Domen, K.; Osterloh, F. E.; Ardo, S., Particle suspension reactors and materials for solar-driven water splitting. *Energy & Environmental Science* **2015,** *8* (10), 2825-2850.

8. Nishiyama, H.; Yamada, T.; Nakabayashi, M.; Maehara, Y.; Yamaguchi, M.; Kuromiya, Y.; Nagatsuma, Y.; Tokudome, H.; Akiyama, S.; Watanabe, T.; Narushima, R.; Okunaka, S.; Shibata, N.; Takata, T.; Hisatomi, T.; Domen, K., Photocatalytic solar hydrogen production from water on a 100-m^2 scale. *Nature* **2021,** *598* (7880), 304-307.

9. Takata, T.; Domen, K., Particulate Photocatalysts for Water Splitting: Recent Advances and Future Prospects. *ACS Energy Letters* **2019,** *4* (2), 542-549.

10. Chen, S.; Takata, T.; Domen, K., Particulate photocatalysts for overall water splitting. *Nature Reviews Materials* **2017,** *2*, 17050.

11. Hisatomi, T.; Kubota, J.; Domen, K., Recent advances in semiconductors for photocatalytic and photoelectrochemical water splitting. *Chemical Society Reviews* **2014,** *43* (22), 7520-7535.

12. Wang, Q.; Hisatomi, T.; Jia, Q.; Tokudome, H.; Zhong, M.; Wang, C.; Pan, Z.; Takata, T.; Nakabayashi, M.; Shibata, N.; Li, Y.; Sharp, I. D.; Kudo, A.; Yamada, T.; Domen, K., Scalable water splitting on particulate photocatalyst sheets with a solar-to-hydrogen energy conversion efficiency exceeding 1. *Nature Materials* **2016,** *15* (6), 611-5.

13. Wang, Q.; Hisatomi, T.; Suzuki, Y.; Pan, Z.; Seo, J.; Katayama, M.; Minegishi, T.; Nishiyama, H.; Takata, T.; Seki, K.; Kudo, A.; Yamada, T.; Domen, K., Particulate Photocatalyst Sheets Based on Carbon Conductor Layer for Efficient Z-Scheme Pure-Water Splitting at Ambient Pressure. *Journal of the American Chemical Society* **2017,** *139* (4), 1675-1683.

14. Hisatomi, T.; Yamamoto, T.; Wang, Q.; Nakanishi, T.; Higashi, T.; Katayama, M.; Minegishi, T.; Domen, K., Particulate photocatalyst sheets based on non-oxide semiconductor materials for water splitting under visible light irradiation. *Catalysis Science & Technology* **2018,** *8* (15), 3918-3925.

15. Pan, C.; Takata, T.; Nakabayashi, M.; Matsumoto, T.; Shibata, N.; Ikuhara, Y.; Domen, K., A Complex Perovskite-Type Oxynitride: The First Photocatalyst for Water Splitting Operable at up to 600 nm. *Angewandte Chemie International Edition* **2015,** *54* (10), 2955-2959.

16. Pan, C.; Takata, T.; Domen, K., Overall Water Splitting on the Transition-Metal Oxynitride Photocatalyst $LaMg_{1/3}Ta_{2/3}O_2N$ over a Large Portion of the Visible-Light Spectrum. *Chemistry – A European Journal* **2016,** *22* (5), 1854-1862.

17. Iwashina, K.; Iwase, A.; Ng, Y. H.; Amal, R.; Kudo, A., Z-Schematic Water Splitting into H_2 and O_2 Using Metal Sulfide as a Hydrogen-Evolving Photocatalyst and Reduced Graphene Oxide as a Solid-State Electron Mediator. *Journal of the American Chemical Society* **2015,** *137* (2), 604-607.

18. Ma, G.; Chen, S.; Kuang, Y.; Akiyama, S.; Hisatomi, T.; Nakabayashi, M.; Shibata, N.; Katayama, M.; Minegishi, T.; Domen, K., Visible Light-Driven Z-Scheme Water Splitting Using Oxysulfide H_2 Evolution Photocatalysts. *The Journal of Physical Chemistry Letters* **2016,** *7* (19), 3892-3896.

19. Chen, S.; Hisatomi, T.; Ma, G.; Wang, Z.; Pan, Z.; Takata, T.; Domen, K., Metal selenides for photocatalytic Z-scheme pure water splitting mediated by reduced graphene oxide. *Chinese Journal of Catalysis* **2019,** *40* (11), 1668-1672.

20. Chen, S.; Vequizo, J. J. M.; Hisatomi, T.; Nakabayashi, M.; Lin, L.; Wang, Z.; Yamakata, A.; Shibata, N.; Takata, T.; Yamada, T.; Domen, K., Efficient photocatalytic hydrogen evolution on single-crystalline metal selenide particles with suitable cocatalysts. *Chemical Science* **2020,** *11* (25), 6436-6441.

21. Chen, S.; Ma, G.; Wang, Q.; Sun, S.; Hisatomi, T.; Higashi, T.; Wang, Z.; Nakabayashi, M.; Shibata, N.; Pan, Z.; Hayashi, T.; Minegishi, T.; Takata, T.; Domen, K., Metal selenide photocatalysts for visible-light-driven Z-scheme pure water splitting. *Journal of Materials Chemistry A* **2019,** *7* (13), 7415-7422.

22. Ham, Y.; Hisatomi, T.; Goto, Y.; Moriya, Y.; Sakata, Y.; Yamakata, A.; Kubota, J.; Domen, K., Flux-mediated doping of $SrTiO_3$ photocatalysts for efficient overall water splitting. *Journal of Materials Chemistry A* **2016,** *4* (8), 3027-3033.

23. Takata, T.; Domen, K., Defect Engineering of Photocatalysts by Doping of Aliovalent Metal Cations for Efficient Water Splitting. *The Journal of Physical Chemistry C* **2009,** *113* (45), 19386-19388.

24. Zhao, Z.; Goncalves, R. V.; Barman, S. K.; Willard, E. J.; Byle, E.; Perry, R.; Wu, Z.; Huda, M. N.; Moulé, A. J.; Osterloh, F. E., Electronic structure basis for enhanced overall water splitting photocatalysis with aluminum doped SrTiO3 in natural sunlight. *Energy & Environmental Science* **2019,** *12* (4), 1385-1395.

25. Goto, Y.; Hisatomi, T.; Wang, Q.; Higashi, T.; Ishikiriyama, K.; Maeda, T.; Sakata, Y.; Okunaka, S.; Tokudome, H.; Katayama, M.; Akiyama, S.; Nishiyama, H.; Inoue, Y.; Takewaki, T.; Setoyama, T.; Minegishi, T.; Takata, T.; Yamada, T.; Domen, K., A Particulate Photocatalyst Water-Splitting Panel for Large-Scale Solar Hydrogen Generation. *Joule* **2018,** *2* (3), 509-520.

26. Maeda, K.; Domen, K., Photocatalytic Water Splitting: Recent Progress and Future Challenges. *The Journal of Physical Chemistry Letters* **2010,** *1* (18), 2655-2661.

27. Takata, T.; Jiang, J.; Sakata, Y.; Nakabayashi, M.; Shibata, N.; Nandal, V.; Seki, K.; Hisatomi, T.; Domen, K., Photocatalytic water splitting with a quantum efficiency of almost unity. *Nature* **2020,** *581* (7809), 411-414.

28. Niki, S.; Contreras, M.; Repins, I.; Powalla, M.; Kushiya, K.; Ishizuka, S.; Matsubara, K., CIGS absorbers and processes. *Progress in Photovoltaics: Research and Applications* **2010,** *18* (6), 453-466.

29. Chen, Y.; Feng, X.; Liu, M.; Su, J.; Shen, S., Towards efficient solar-to-hydrogen conversion: Fundamentals and recent progress in copper-based chalcogenide photocathodes. *Nanophotonics* **2016,** *5* (4), 524-547.

30. Kobayashi, H.; Sato, N.; Orita, M.; Kuang, Y.; Kaneko, H.; Minegishi, T.; Yamada, T.; Domen, K., Development of highly efficient $CuIn_{0.5}Ga_{0.5}Se_2$-based photocathode and application to overall solar driven water splitting. *Energy & Environmental Science* **2018,** *11* (10), 3003-3009.

31. Gaillard, N.; Prasher, D.; Chong, M.; Deangelis, A.; Horsley, K.; Ishii, H. A.; Bradley, J. P.; Varley, J.; Ogitsu, T., Wide-Bandgap Cu(In,Ga)S_2 Photocathodes Integrated on Transparent Conductive F:SnO2 Substrates for Chalcopyrite-Based Water Splitting Tandem Devices. *ACS Applied Energy Materials* **2019,** *2* (8), 5515-5524.

32. Kumagai, H.; Minegishi, T.; Moriya, Y.; Kubota, J.; Domen, K., Photoelectrochemical Hydrogen Evolution from Water Using Copper Gallium Selenide Electrodes Prepared by a Particle Transfer Method. *The Journal of Physical Chemistry C* **2014,** *118* (30), 16386-16392.

33. Moriya, M.; Minegishi, T.; Kumagai, H.; Katayama, M.; Kubota, J.; Domen, K., Stable hydrogen evolution from CdS-modified $CuGaSe_2$ photoelectrode under visible-light irradiation. *Journal of the American Chemical Society* **2013,** *135* (10), 3733-3735.

34. Kubacka, A.; Fernández-García, M.; Colón, G., Advanced Nanoarchitectures for Solar Photocatalytic Applications. *Chemical Reviews* **2012,** *112* (3), 1555-1614.

35. Kudo, A.; Miseki, Y., Heterogeneous photocatalyst materials for water splitting. *Chemical Society Reviews* **2009,** *38* (1), 253-278.

36. Hernández-Alonso, M. D.; Fresno, F.; Suárez, S.; Coronado, J. M., Development of alternative photocatalysts to TiO_2: Challenges and opportunities. *Energy & Environmental Science* **2009,** *2* (12), 1231-1257.

37. Yang, Y.; Niu, S.; Han, D.; Liu, T.; Wang, G.; Li, Y., Progress in Developing Metal Oxide Nanomaterials for Photoelectrochemical Water Splitting. *Advanced Energy Materials* **2017,** *7* (19), 1700555.

38. Hong, S.; Burkhow, S. J.; Doughty, R. M.; Cheng, Y.; Ryan, B. J.; Mantravadi, A.; Roling, L. T.; Panthani, M. G.; Osterloh, F. E.; Smith, E. A.; Zaikina, J. V., Local Structural Disorder in Metavanadates MV_2O_6 (M = Zn and Cu) Synthesized by the Deep Eutectic Solvent Route: Photoactive Oxides with Oxygen Vacancies. *Chemistry of Materials* **2021,** *33* (5), 1667-1682.

39. Hong, S.; Cheng, Y.; Hariyani, S.; Li, J.; Doughty, R. M.; Mantravadi, A.; Adeyemi, A. N.; Smith, E. A.; Brgoch, J.; Osterloh, F. E.; Zaikina, J. V., The Deep Eutectic Solvent Precipitation Synthesis of Metastable $Zn_4V_2O_9$. *Inorganic Chemistry* **2022,** *61* (1), 154-169.

40. Kim, J. H.; Kim, H. E.; Kim, J. H.; Lee, J. S., Ferrites: emerging light absorbers for solar water splitting. *Journal of Materials Chemistry A* **2020,** *8* (19), 9447-9482.

41. Matsumoto, Y.; Omae, M.; Sugiyama, K.; Sato, E., New photocathode materials for hydrogen evolution: calcium iron oxide ($CaFe_2O_4$) and strontium iron oxide ($Sr_7Fe_{10}O_{22}$). *The Journal of Physical Chemistry* **1987,** *91* (3), 577-581.

42. Ida, S.; Yamada, K.; Matsunaga, T.; Hagiwara, H.; Matsumoto, Y.; Ishihara, T., Preparation of p-Type $CaFe_2O_4$ Photocathodes for Producing Hydrogen from Water. *Journal of the American Chemical Society* **2010,** *132* (49), 17343-17345.

43. Kirchberg, K.; Marschall, R., Sol-gel synthesis of mesoporous $CaFe_2O_4$ photocathodes with hierarchical pore morphology. *Sustainable Energy & Fuels* **2019,** *3* (5), 1150-1153.

44. Díez-García, M. I.; Gómez, R., Investigating Water Splitting with $CaFe_2O_4$ Photocathodes by Electrochemical Impedance Spectroscopy. *ACS Applied Materials & Interfaces* **2016,** *8* (33), 21387-21397.

45. Dom, R.; Kim, H. G.; Borse, P. H., Photo Chemical Hydrogen Generation from Orthorhombic $CaFe_2O_4$ Nanoparticles Synthesized by Different Methods. *ChemistrySelect* **2017,** *2* (8), 2556-2564.

46. Bloesser, A.; Timm, J.; Kurz, H.; Milius, W.; Hayama, S.; Breu, J.; Weber, B.; Marschall, R., A Novel Synthesis Yielding Macroporous $CaFe_2O_4$ Sponges for Solar Energy Conversion. *Solar RRL* **2020,** *4* (8), 1900570.

47. Yang, W.; Prabhakar, R. R.; Tan, J.; Tilley, S. D.; Moon, J., Strategies for enhancing the photocurrent, photovoltage, and stability of photoelectrodes for photoelectrochemical water splitting. *Chemical Society Reviews* **2019,** *48* (19), 4979-5015.

48. He, Y.; Hamann, T.; Wang, D., Thin film photoelectrodes for solar water splitting. *Chemical Society Reviews* **2019,** *48* (7), 2182-2215.

49. Gerischer, H., Electrochemical Behavior of Semiconductors under Illumination. *Journal of the Electrochemical Society* **1966,** *113* (11), 1174-1182.

50. Lewis, N. S., A Quantitative Investigation of the Open-Circuit Photovoltage at the Semiconductor/Liquid Interface. *Journal of the Electrochemical Society* **1984,** *131* (11), 2496-2503.

51. Gerischer, H., The impact of semiconductors on the concepts of electrochemistry. *Electrochimica Acta* **1990,** *35* (11), 1677-1699.

52. Walter, M. G.; Warren, E. L.; McKone, J. R.; Boettcher, S. W.; Mi, Q.; Santori, E. A.; Lewis, N. S., Solar Water Splitting Cells. *Chemical Reviews* **2010,** *110* (11), 6446-6473.

53. Lewis, N. S., Chemical Control of Charge Transfer and Recombination at Semiconductor Photoelectrode Surfaces. *Inorganic Chemistry* **2005,** *44* (20), 6900-6911.

54. Bard, A. J.; Bocarsly, A. B.; Fan, F. R. F.; Walton, E. G.; Wrighton, M. S., The concept of Fermi level pinning at semiconductor/liquid junctions. Consequences for energy conversion efficiency and selection of useful solution redox couples in solar devices. *Journal of the American Chemical Society* **1980,** *102* (11), 3671-3677.

55. Hinkle, C. L.; Milojevic, M.; Brennan, B.; Sonnet, A. M.; Aguirre-Tostado, F. S.; Hughes, G. J.; Vogel, E. M.; Wallace, R. M., Detection of Ga suboxides and their impact on III-V passivation and Fermi-level pinning. *Applied Physics Letters* **2009,** *94* (16), 162101.

56. Klahr, B.; Gimenez, S.; Fabregat-Santiago, F.; Hamann, T.; Bisquert, J., Water Oxidation at Hematite Photoelectrodes: The Role of Surface States. *Journal of the American Chemical Society* **2012,** *134* (9), 4294-4302.

57. Jang, Y. J.; Lee, J. S., Photoelectrochemical Water Splitting with p-Type Metal Oxide Semiconductor Photocathodes. *ChemSusChem* **2019,** *12* (9), 1835-1845.

58. Liu, Y.; Le Formal, F.; Boudoire, F.; Yao, L.; Sivula, K.; Guijarro, N., Insights into the interfacial carrier behaviour of copper ferrite ($CuFe_2O_4$) photoanodes for solar water oxidation. *Journal of Materials Chemistry A* **2019,** *7* (4), 1669-1677.

59. Lichterman, M. F.; Hu, S.; Richter, M. H.; Crumlin, E. J.; Axnanda, S.; Favaro, M.; Drisdell, W.; Hussain, Z.; Mayer, T.; Brunschwig, B. S.; Lewis, N. S.; Liu, Z.; Lewerenz, H.-J., Direct observation of the energetics at a semiconductor/liquid junction by operando X-ray photoelectron spectroscopy. *Energy & Environmental Science* **2015,** *8* (8), 2409-2416.

60. Liu, Y.; Bouri, M.; Yao, L.; Xia, M.; Mensi, M.; Grätzel, M.; Sivula, K.; Aschauer, U.; Guijarro, N., Identifying Reactive Sites and Surface Traps in Chalcopyrite Photocathodes. *Angewandte Chemie International Edition* **2021,** *60* (44), 23651-23655.

61. Mayer, M. T., Photovoltage at semiconductor–electrolyte junctions. *Current Opinion in Electrochemistry* **2017,** *2* (1), 104-110.

62. Hu, S.; Xiang, C.; Haussener, S.; Berger, A. D.; Lewis, N. S., An analysis of the optimal band gaps of light absorbers in integrated tandem photoelectrochemical water-splitting systems. *Energy & Environmental Science* **2013,** *6* (10), 2984-2993.

63. Sun, S.; Hisatomi, T.; Wang, Q.; Chen, S.; Ma, G.; Liu, J.; Nandy, S.; Minegishi, T.; Katayama, M.; Domen, K., Efficient Redox-Mediator-Free Z-Scheme Water Splitting Employing Oxysulfide Photocatalysts under Visible Light. *ACS Catalysis* **2018,** *8* (3), 1690-1696.

64. Song, Z.; Hisatomi, T.; Chen, S.; Wang, Q.; Ma, G.; Li, S.; Zhu, X.; Sun, S.; Domen, K., Visible-Light-Driven Photocatalytic Z-Scheme Overall Water Splitting in $La_5Ti_2AgS_5O_7$-based Powder-Suspension System. *ChemSusChem* **2019,** *0* (0).

65. Coridan, R. H.; Nielander, A. C.; Francis, S. A.; McDowell, M. T.; Dix, V.; Chatman, S. M.; Lewis, N. S., Methods for comparing the performance of energy-conversion systems for use in solar fuels and solar electricity generation. *Energy & Environmental Science* **2015,** *8* (10), 2886-2901.

66. Pan, Z.; Yanagi, R.; Wang, Q.; Shen, X.; Zhu, Q.; Xue, Y.; Röhr, J. A.; Hisatomi, T.; Domen, K.; Hu, S., Mutually-dependent kinetics and energetics of photocatalyst/co-catalyst/two-redox liquid junctions. *Energy & Environmental Science* **2020,** *13* (1), 162-173.

67. Lin, F.; Boettcher, S. W., Adaptive semiconductor/electrocatalyst junctions in water-splitting photoanodes. *Nature Materials* **2014,** *13* (1), 81-86.

68. Nellist, M. R.; Laskowski, F. A. L.; Lin, F.; Mills, T. J.; Boettcher, S. W., Semiconductor–Electrocatalyst Interfaces: Theory, Experiment, and Applications in Photoelectrochemical Water Splitting. *Accounts of Chemical Research* **2016,** *49* (4), 733-740.

69. Nellist, M. R.; Laskowski, F. A. L.; Qiu, J.; Hajibabaei, H.; Sivula, K.; Hamann, T. W.; Boettcher, S. W., Potential-sensing electrochemical atomic force microscopy for in operando analysis of water-splitting catalysts and interfaces. *Nature Energy* **2018,** *3* (1), 46-52.

70. Nellist, M. R.; Qiu, J.; Laskowski, F. A. L.; Toma, F. M.; Boettcher, S. W., Potential-Sensing Electrochemical AFM Shows CoPi as a Hole Collector and Oxygen Evolution Catalyst on $BiVO_4$ Water-Splitting Photoanodes. *ACS Energy Letters* **2018,** *3* (9), 2286-2291.

71. Laskowski, F. A. L.; Nellist, M. R.; Qiu, J.; Boettcher, S. W., Metal Oxide/(oxy)hydroxide Overlayers as Hole Collectors and Oxygen-Evolution Catalysts on Water-Splitting Photoanodes. *Journal of the American Chemical Society* **2019,** *141* (4), 1394-1405.

72. Laskowski, F. A. L.; Oener, S. Z.; Nellist, M. R.; Gordon, A. M.; Bain, D. C.; Fehrs, J. L.; Boettcher, S. W., Nanoscale semiconductor/catalyst interfaces in photoelectrochemistry. *Nature Materials* **2020,** *19* (1), 69-76.

73. Muzzillo, C. P.; Klein, W. E.; Li, Z.; DeAngelis, A. D.; Horsley, K.; Zhu, K.; Gaillard, N., Low-Cost, Efficient, and Durable H2 Production by Photoelectrochemical Water Splitting with $CuGa_3Se_5$ Photocathodes. *ACS Applied Materials & Interfaces* **2018,** *10* (23), 19573-19579.

74. Palm, D. W.; Muzzillo, C. P.; Ben-Naim, M.; Khan, I.; Gaillard, N.; Jaramillo, T. F., Tungsten oxide-coated copper gallium selenide sustains long-term solar hydrogen evolution. *Sustainable Energy & Fuels* **2021,** *5* (2), 384-390.

75. Khan, I. S.; Muzzillo, C. P.; Perkins, C. L.; Norman, A. G.; Young, J. L.; Gaillard, N.; Zakutayev, A., $Mg_xZn_{1-x}O$ contact to $CuGa_3Se_5$ absorber for photovoltaic and photoelectrochemical devices. *Journal of Physics: Energy* **2021,** *3* (2), 024001.

76. Mahmoudi, B.; Caddeo, F.; Lindenberg, T.; Schneider, T.; Hölscher, T.; Scheer, R.; Maijenburg, A. W., Photoelectrochemical properties of Cu-Ga-Se photocathodes with compositions ranging from $CuGaSe_2$ to $CuGa_3Se_5$. *Electrochimica Acta* **2021,** *367*, 137183.

77. Dittrich, T.; Fengler, S., *Surface Photovoltage Analysis of Photoactive Materials*. World Scientific Publishing Europe Ltd.: 2020.

78. Kronik, L.; Shapira, Y., Surface photovoltage phenomena: theory, experiment, and applications. *Surface Science Reports* **1999,** *37*, 1-206.

79. Brattain, W. H., Evidence for Surface States on Semiconductors from Change in Contact Potential on Illumination. *Physical Review* **1947,** *72* (4), 345-345.

80. Brattain, W. H.; Bardeen, J., Surface Properties of Germanium. *Bell System Technical Journal* **1953,** *32* (1), 1-41.

81. Gatos, H. C.; Lagowski, J., Surface Photovoltage Spectroscopy—A New Approach to the Study of High-Gap Semiconductor Surfaces. *Journal of Vacuum Science and Technology* **1973,** *10* (1), 130-135.

82. Kronik, L.; Shapira, Y., Surface photovoltage spectroscopy of semiconductor structures: at the crossroads of physics, chemistry and electrical engineering. *Surface and Interface Analysis* **2001,** *31* (10), 954-965.

83. Wang, J.; Zhao, J.; Osterloh, F. E., Photochemical charge transfer observed in nanoscale hydrogen evolving photocatalysts using surface photovoltage spectroscopy. *Energy & Environmental Science* **2015,** *8* (10), 2970-2976.

84. Zhao, J.; Osterloh, F. E., Photochemical Charge Separation in Nanocrystal Photocatalyst Films: Insights from Surface Photovoltage Spectroscopy. *Journal of Physical Chemistry Letters* **2014,** *5* (5), 782-786.

85. Zhao, J.; Nail, B. A.; Holmes, M. A.; Osterloh, F. E., Use of Surface Photovoltage Spectroscopy to Measure Built-in Voltage, Space Charge Layer Width, and Effective Band Gap in CdSe Quantum Dot Films. *J Phys Chem Lett* **2016,** *7* (17), 3335-40.

86. Doughty, R. M.; Hodges, B.; Dominguez, J.; Han, R.; Zhao, Z.; Assavachin, S.; Osterloh, F. E., Fermi Level Pinning Controls Band Bending and Photochemical Charge Separation in Particles of n-$SrTiO_3$, n-$SrTiO_3$:Al, and n-GaAs:Te. *The Journal of Physical Chemistry C* **2020,** *124* (34), 18426-18435.

87. Ma, X.; Cui, X.; Zhao, Z.; Melo, M. A.; Roberts, E. J.; Osterloh, F. E., Use of surface photovoltage spectroscopy to probe energy levels and charge carrier dynamics in transition metal (Ni, Cu, Fe, Mn, Rh) doped $SrTiO_3$ photocatalysts for H_2 evolution from water. *Journal of Materials Chemistry A* **2018,** *6* (14), 5774-5781.

88. Ma, X.; Wu, Z.; Roberts, E. J.; Han, R.; Rao, G.; Zhao, Z.; Lamoth, M.; Cui, X.; Britt, R. D.; Osterloh, F. E., Surface Photovoltage Spectroscopy Observes Sub-Band-Gap Defects in Hydrothermally Synthesized $SrTiO_3$ Nanocrystals. *The Journal of Physical Chemistry C* **2019,** *123* (41), 25081-25090.

89. Zhao, Z.; Willard, E. J.; Li, H.; Wu, Z.; Castro, R. H. R.; Osterloh, F., Aluminum Enhances Photochemical Charge Separation in Strontium Titanate Nanocrystal Photocatalysts for Overall Water Splitting. *Journal of Materials Chemistry A* **2018,** *6* (33), 16170-16176.

90. Wu, Z.; Cheung, G.; Wang, J.; Zhao, Z.; Osterloh, F. E., Wavelength dependent photochemical charge transfer at the Cu_2O–$BiVO_4$ particle interface – evidence for tandem excitation. *Chemical Communications* **2018,** *54* (65), 9023-9026.

91. Han, R.; Kim, T.-Y.; Hamann, T. W.; Osterloh, F. E., Photochemical Charge Separation and Dye Self-Oxidation Control Performance of Fluorescein, Rose Bengal, and Triphenylamine Dye-Sensitized Solar Cells. *The Journal of Physical Chemistry C* **2020,** *124* (48), 26174-26183.

92. Assavachin, S.; Nail, B. A.; V. Goncalves, R.; Mulcahy, J. R.; Lloyd, S. E.; Osterloh, F. E., Ferroelectric surface photovoltage enhancement in chromium-doped $SrTiO_3$ nanocrystal photocatalysts for hydrogen evolution. *Materials Advances* **2020,** *1* (5), 1382-1389.

Chapter 2 Liquid Surface Photovoltage Reveals Effects of Substrates and Passivation Layers on Quasi-Fermi Level Splitting of $CuGa_3Se_5$ Thin Film Photocathodes for Proton and Methyl Viologen Reduction

The work in this Chapter contains unpublished results. Part of the work is used in the manuscript "Contactless Measurement of Quasi Fermi Level Splitting in Solar Fuel Photoelectrodes" that submitted to Nature Energy (Sep 2022). Other parts are prepared in the manuscript "Effect of Charge Selective Contacts on Quasi Fermi Level Splitting of $CuGa_3Se_5$ Thin Film Photocathodes for Hydrogen Evolution and Methylviologen Reduction" that will be submitted for publication soon. The XPS in this work is contributed by Chengcan Xiao in the Osterloh lab.

Introduction

Copper chalcopyrites, $Cu(In_xGa_{1-x})Se_2$ (CIGS) (x = 0~1), have been well established for thin film photovoltaic (PV) applications, due to their tunable band gap, high absorption coefficients and usability in the polycrystalline state.[1-3] In recent decades there also has been emerging research on these materials for photoelectrochemical (PEC) water splitting.[4-11] It has been shown that lower Cu content relative to stoichiometric $CuGaSe_2$ leads to more favorable energy band positions for better PEC performance.[12] Specifically, $CuGa_3Se_5$, has emerged as a champion because of its wider band gap (*ca.* 1.85 eV) and deeper valence band potential.[12-15] Utilization of a buried junction with cadmium sulfide extraction layer is often required to achieve a relatively positive onset for PEC water reduction.[5, 10-11, 15] For devices with direct $CuGa_3Se_5$/electrolyte interface, stable H_2-generation saturation photocurrent were only reached at a negative potential versus the reversible hydrogen electrode (RHE).[13-14] For example, the Maijenburg group reports hour-stable H_2-related saturation photocurrents of 68% of the theoretical limit (-12.1 $mA \cdot cm^{-2}$ at -0.40 V_{RHE}).[14] However, the onset of only +0.20 V_{RHE} is not positive enough to make it an efficient photocathode that can be utilized in a tandem water splitting system. The onset indicates that there is substantial voltage loss of this photocathode with direct $CuGa_3Se_5$/electrolyte contact.

Recently, the Sivula group used spectroelectrochemical and computational methods on a related $CuIn_{0.3}Ga_{0.7}S_2$ photocathode to conclude that voltage losses are linked to charge carrier traps induced by surface Ga and In vacancies.[16] A similar voltage loss mechanism may limit operation of the $CuGa_3Se_5$ photocathode. To test this hypothesis, we employ liquid SPV to measure the internal photovoltage of an illuminated $CuGa_3Se_5$ (CGSe) photocathode in contact with several electrolytes for the first time.

(Note: In this chapter, **CGSe** is used as abbreviation for $CuGa_3Se_5$ specifically.)

Preliminary evidence with $BiVO_4$ and GaP photoelectrodes (unpublished results) suggests that the liquid SPV signal reports on quasi-Fermi level splitting (the internal photovoltage) of a semiconductor/liquid junction, as illustrated in **Figure 2.1**. Thus, by combining SPV with open circuit potential measurements that provide the majority carrier quasi-Fermi level, the minority carrier quasi-Fermi level at the CGSe photocathode/liquid interface under illumination can be obtained.

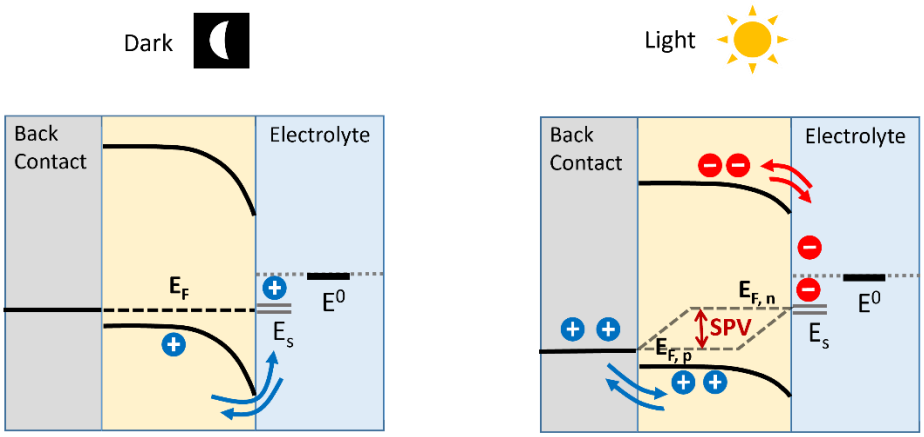

Figure 2.1 Energetics and charge carrier dynamics of a typical p-type semiconductor-liquid junction, in the dark and under illumination. SPV gives quasi-Fermi level splitting (QFLS) energy. Quasi-Fermi levels, $E_{f,n}$ and $E_{f,p}$, are shown together with the standard reduction potentials of the solution E^0 and of the surface states E_S.

The CGSe thin film photocathode used in this study is provided by Prof. Wouter Maijenburg's group from Martin-Luther-University Halle-Wittenberg, Germany. Details of the preparation are

described in their previous publication.[14] The samples consist of 2 μm thick $CuGa_3Se_5$ on molybdenum- or FTO-coated soda-lime glass and are noted as **Mo-CGSe** and **FTO-CGSe**, respectively. Photos, SEM and reported PEC water reduction performance of the Mo-CGSe electrode are shown in **Figure 2.15** in the Appendix. The SEM images show a flake-shape morphology with a high density of grain boundaries. The PEC data in electrolyte of 0.5 M H_2SO_4 under AM 1.5 irradiation shows a saturated photocurrent of -12 $mA \cdot cm^{-2}$ (at -0.40 V_{RHE}) for water reduction with a photo-onset of 0.20 V_{RHE}. This is one of the best PEC water reduction performances reported for $CuGa_3Se_5$ photocathode with direct CGSe/electrolyte contact.[13-14] While promising regarding its photocurrent, the photo-onset is below expectations. Based on its band positions, $CuGa_3Se_5$ should be able to reduce protons at potentials positive of 0.80 V_{RHE} under illumination. The voltage loss may be a result of material defects, or it may be related to a substantial kinetic proton reduction overpotential. For the related Cu_2Se [17-18] and for layered GaSe,[19] proton reduction overpotentials were reported to be 0.8 V and near 0.3 V, respectively. To better understand the photocathodic performance of CGSe, its photoelectrochemical and SPV response was measured in different electrolytes. Viologen dications (4,4′-bipyridinium compounds) were chosen because of the high solubility, formal potentials negative of the hydrogen potential and fast, reversible charge transfer kinetics.[20-21] Specifically, methyl viologen ($MVCl_2$) and benzyl viologen ($BVCl_2$) have redox potentials of $E_{MV2+/MV+}$ = -0.446 V_{NHE} and $E_{BV2+/BV+}$ = -0.359 V_{NHE}.[22] Water reduction was studied in the presence of 0.1 M Na_2SO_4. To all systems, 0.05 M phosphate buffer was used to exclude pH variations. Electrolytes are abbreviated as follows:

NaPi: 0.1 M Na_2SO_4 with 0.05 M pH=7 sodium phosphate buffer

MV: 0.01 $MVCl_2$ with 0.05 M pH=7 sodium phosphate buffer

BV: 0.01 M $BVCl_2$ with 0.05 M pH=7 sodium phosphate buffer

Results and Discussion

To assess the ability of the CGSe electrodes to photo-reduce methyl viologen or protons, linear sweep voltammetry (LSV) measurements were conducted on the systems above under chopped light illumination. **Figure 2.2a** and **2.2b** show the LSV curves for the Mo-CGSe electrode in NaPi and MV electrolytes, respectively. Cathodic photocurrents were observed for water reduction and MV^{2+} reduction, respectively. **Figure 2.2a** shows that the stable photocurrent reaches -3 $mA \cdot cm^{-2}$ at 0 V_{RHE}, approximately one-third of the photocurrent achieved in 0.5 M H_2SO_4 electrolyte reported by Maijenburg[14] (**Figure 2.15c**). This difference in photocurrents is attributed to the concentration difference of protons, as the proton concentration in NaPi at pH 7 is six orders of magnitude lower than that in 0.5 M H_2SO_4 electrolyte. In addition, strong capacitive currents were observed, as evident by the sawtooth shape of the photocurrent response after switching the light on. The capacitive current is due to the trapping and de-trapping of photogenerated charge carriers at CGSe/electrolyte interface.[23] As shown in **Figure 2.2a**, the onset potential of PEC water reduction is at 0.32 V_{RHE}, similar to the value (0.20 V_{RHE}) observed in 0.5 H_2SO_4. Based on this value and the standard water reduction potential, the external photovoltage $\mathbf{V_{ph}}$ **(ext, LSV)** is estimated to be $E_{on} - E^0_{(H+/H2)} = 0.32\ V_{RHE} - 0.0\ V_{RHE} = 0.32$ V for the Mo-CGSe/NaPi contact. [24] Hydrogen evolution was evident from bubble formation at the working electrode under cathodic bias (0.0 V_{RHE}). The LSV curve of the Mo-CGSe electrode in MV electrolyte is shown in **Figure 2.2b**. The curve shape is similar to the water reduction curve in **Figure 2.2a**, but this time no bubbles were formed. Instead, a purple color is observed from the MV^+ radical cation suggesting that MV^{2+} reduction is taking place instead of proton reduction. The onset potential of MV^{2+} reduction is at 0.35 V_{RHE}, so the external photovoltage is estimated to be $E_{on} - E^0_{(MV2+/MV+)} = 0.35\ V_{RHE} - (-0.03)\ V_{RHE} = 0.38$ V for the Mo-CGSe/MV contact.

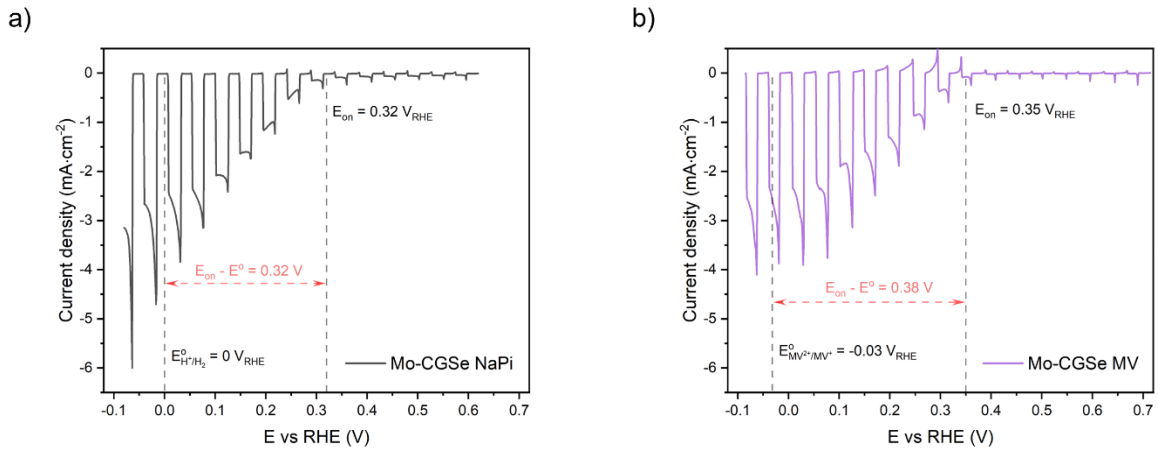

Figure 2.2 Linear sweep voltammetry (LSV) scans of the Mo-CGSe electrode under chopped illumination (400 nm, 81 mW·cm^{-2}). (a) Electrolyte: 0.1 M Na_2SO_4 with 0.05 M sodium phosphate buffer (pH=7). (b) Electrolyte: 0.01 M $MVCl_2$ with 0.05 M sodium phosphate buffer (pH=7). Electrolytes were de-aerated by continuous N_2 bubbling.

Next, to obtain the Fermi level in the dark ($E_{f,\,dark}$) and quasi-Fermi level of holes ($E_{f,\,p}$) under illumination, open circuit potential (OCP) measurements were done on the Mo-CGSe electrodes. The data measured with increasing light intensity is shown in **Figure 2.3**. In both systems, $E_{f,\,dark}$ is at around 0.53 V_{RHE}. The MV^{2+} did not affect $E_{f,\,dark}$, possibly because no reduced MV^{+} radicals are present in the experiment. Likely, the Fermi level is pinned to CGSe surface states in both cases. Under illumination, $E_{f,\,p}$ moves to more positive potentials, as expected for a p-type photocathode. For example, at 81 mW·cm^{-2}, $E_{f,\,p}$ = 0.71 V_{RHE} for Mo-CGSe/NaPi and $E_{f,\,p}$ = 0.77 V_{RHE} for Mo-CGSe/MV. This corresponds to an external photovoltage $\mathbf{V_{ph}}$ **(ext, OCP)** = $E_{f,\,dark}$ - $E_{f,\,p\,light}$ of 0.18 V for Mo-CGSe/NaPi and 0.25 V for Mo-CGSe/MV. These values are smaller than those observed for the PEC method. For the latter, a negative bias is applied which increases the band banding and charge separation efficiency of the photoelectrode. This explains the increased photovoltage compared to the open circuit condition.

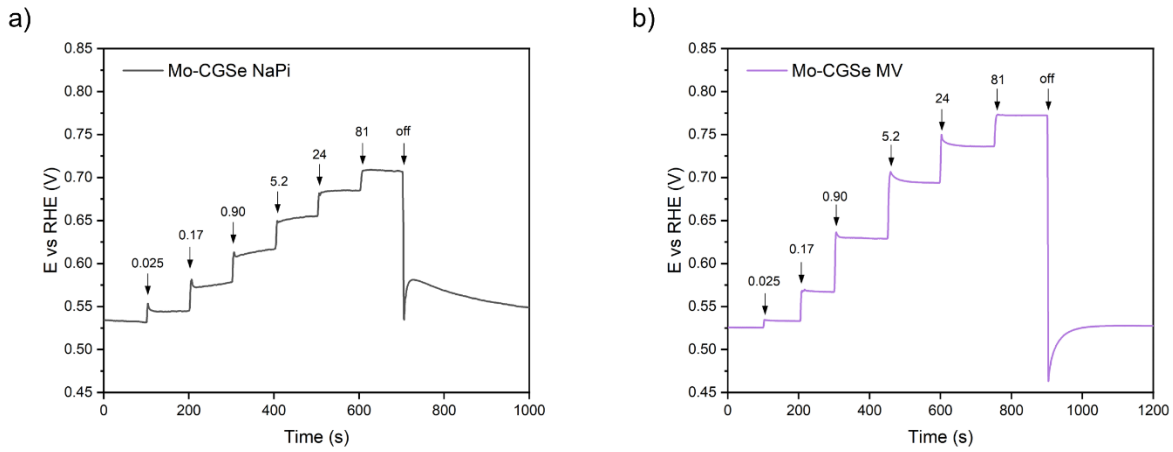

Figure 2.3 Open circuit potential (OCP) of the Mo-CGSe electrode in the dark and under 400 nm monochromatic illumination of variable intensity (irradiances given in $mW \cdot cm^{-2}$). (a) Electrolyte: 0.1 M Na_2SO_4 with 0.05 M sodium phosphate buffer (pH=7). (b) Electrolyte: 0.01 M $MVCl_2$ with 0.05 M sodium phosphate buffer (pH=7). Electrolytes were de-aerated by continuous N_2 bubbling.

Finally, to measure the quasi-Fermi level splitting of CGSe, chopped light surface photovoltage data of the Mo-CGSe electrode in variable light intensity were recorded. **Figure 2.4a** and **b** show the contact potential difference (CPD) versus the time, with chopped light of variable intensity. The difference of the CPD between dark and light conditions is defined as the surface photovoltage (SPV).[25-28] As expected for the p-type $CuGa_3Se_5$ electrode, a positive SPV signal from transfer of majority carriers (holes) into the electric contact at the CGSe backside and of minority carriers (electrons) into surface states were observed. The SPV signal increases when the light intensity increases, the trend is described below. SPV data in both systems are reversible. For both systems, the baseline drifts by 0.1 V to smaller CPD values, indicating trapping of minority charge carriers (electrons) at the CGS/Mo interface. The Mo-CGSe/MV shows slightly larger SPV signal than the Mo-CGSe/NaPi, but the difference is not significant.

For each system, the SPV was also plotted versus the logarithm of light intensity, shown in **Figure 2.4c** and **d** (closed dots). For an ideal photovoltaic junction, the quasi-Fermi level splitting energy (the SPV signal) is expected to increase linearly with the logarithm of light intensity.[29-30] Experimentally, the Mo-

CGSe/NaPi shows slopes of 77 mV/dec and 37 mV/dec at low and high light intensity. The Mo-CGSe/MV gives the slope of 75 mV/dec over the entire intensity interval. Deviations from the ideal 59 mV slope value indicate that there are different recombination processes happening at the Mo/CGSe or CGSe/electrolyte junction under illumination. This is quite common for real photovoltaic junctions.[30] Though the slope varies from the ideal case, it still shows decent linear trend in the whole or separate regions. This allows us to interpolate the SPV, so that SPV values can be compared directly to the external photovoltages at each light intensity. **Figure 2.4c** and **d** (open dots) show the data points that were extracted from the plots. For the Mo-CGSe/NaPi contact, the SPV is estimated to be 0.23 V (81mW·cm^{-2}). It is comparable to the V_{ph} (ext, OCP) of 0.22 V, but slightly smaller than the V_{ph} (ext, LSV) of 0.32 V. For the Mo-CGSe/MV contact, the SPV is estimated to be 0.30 V (81mW·cm^{-2}). It is comparable to the V_{ph} (ext, OCP) of 0.35 V and V_{ph} (ext, LSV) of 0.38 V. This shows that the photovoltage observed by the liquid SPV are in reasonable agreement with the external photovoltage measured by the conventional PEC and OCP method.

It is worthy to point out that the photovoltage estimated from photoelectrochemical (PEC) scans may not reflect the true value, because the photocurrent onset may be from reduction of CGSe surface species instead of proton or MV^{2+} reduction. Moreover, liquid SPV measurement is done at no applied bias, when $E_{f,\,p} = 0.71\ V_{RHE}$. In contrast, the PEC water reduction onset of 0.32 V_{RHE}, corresponds to an applied negative potential and increased band bending. This explains the differences between SPV and external photovoltage from PEC.

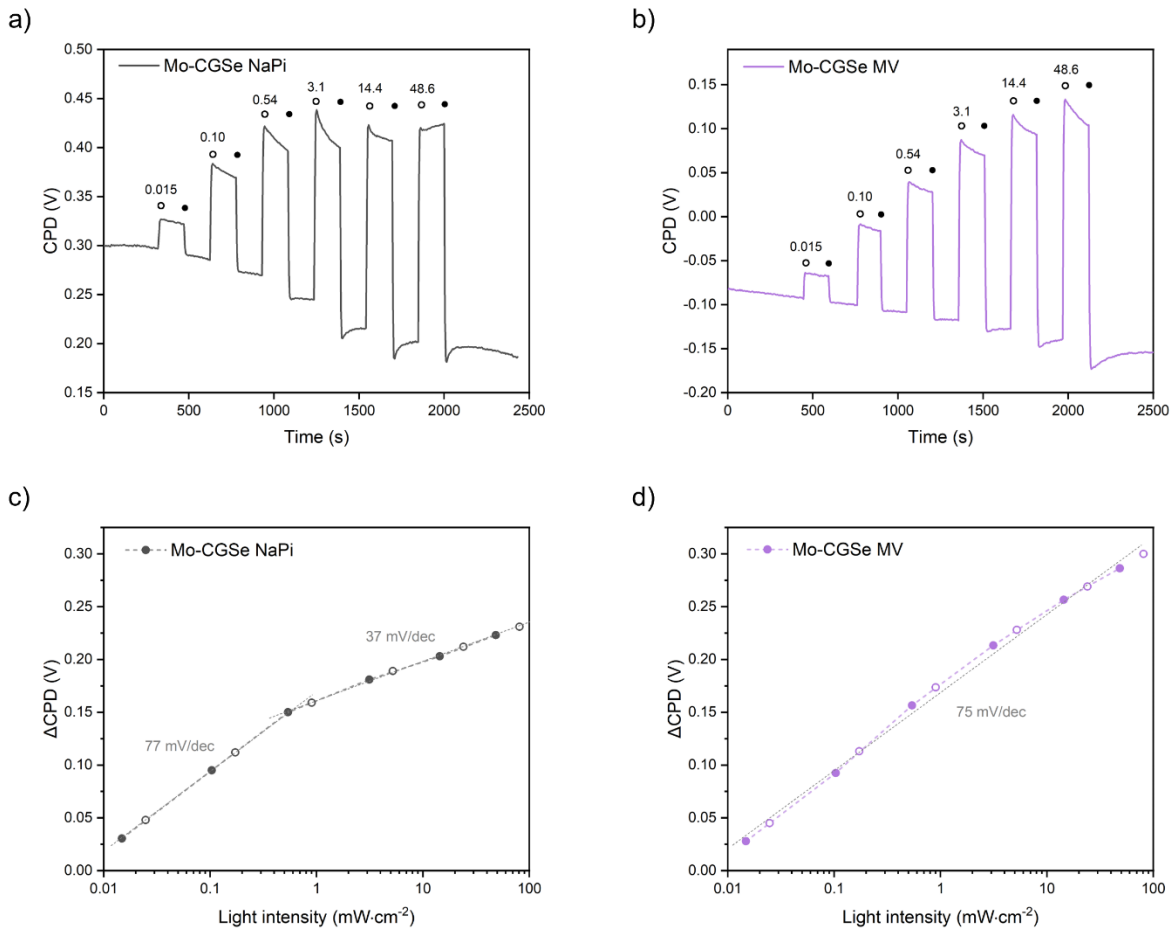

Figure 2.4 Surface photovoltage (SPV) data of the Mo-CGSe electrode under 400 nm monochromatic illumination of variable intensity (irradiances given in $mW \cdot cm^{-2}$). (a) Electrolyte: NaPi. (b) Electrolyte: MV. (c)(d) SPV versus logarithm of the light intensity for each system. SPV = CPD (light) – CPD (dark). Closed dots: Experimental data. Open dots: Interpolated and extrapolated SPV values.

Assuming that the SPV equals the quasi-Fermi level splitting ($E_{f,\,p} - E_{f,\,n}$), and that quasi-Fermi level of the holes ($E_{f,\,p}$) is obtained from the OCP measurement, quasi-Fermi level of the electrons ($E_{f,\,n}$) can be calculated with the equation of $E_{f,\,n} = E_{f,\,p} - SPV$. The quasi-Fermi levels, $E_{f,\,n}$ and $E_{f,\,p}$, were plotted versus the logarithm of light intensity to produce the QFLS plots in **Figure 2.5**. In both electrolytes, $E_{f,\,p}$ becomes slightly more oxidizing with increasing light intensity while $E_{f,\,n}$ stays constant and appears pinned by the surface states, which could be surface Ga vacancies states near the flat band

potential.[16] The quasi-Fermi level splitting suggests that MV^{2+} in the electrolyte is not changing the junction compared to NaPi. Based on the potential of $E_{f,\,n}$, without applied cathodic potential, Mo-CGSe can neither reduce protons nor MV^{2+}, even under the highest illumination intensity.

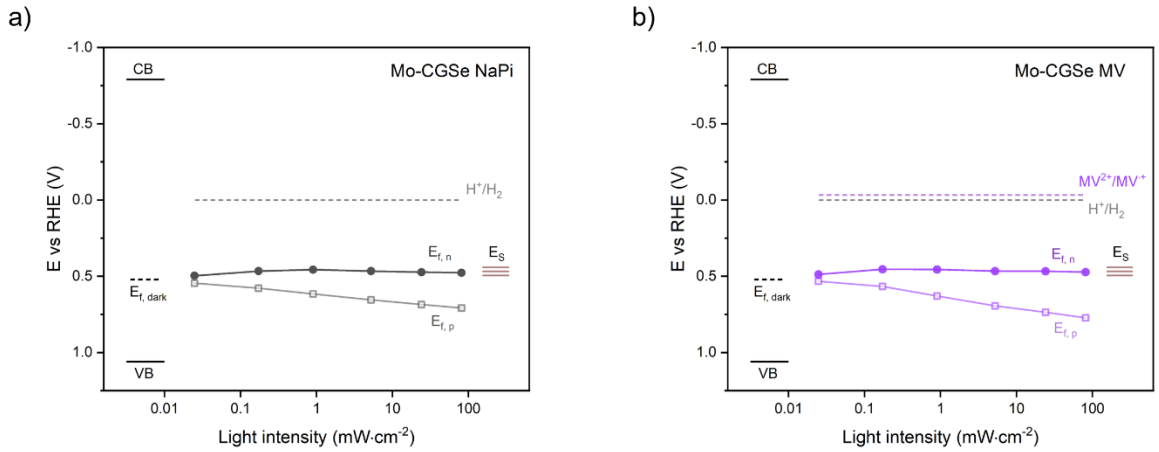

Figure 2.5 Quasi-Fermi level splitting (QFLS) plots of the Mo-CGSe electrodes with the electrolyte of (a) NaPi and (b) MV. Quasi-Fermi levels, $E_{f,\,n}$ and $E_{f,\,p}$, were plotted versus the logarithm of light intensity (400 nm LED).

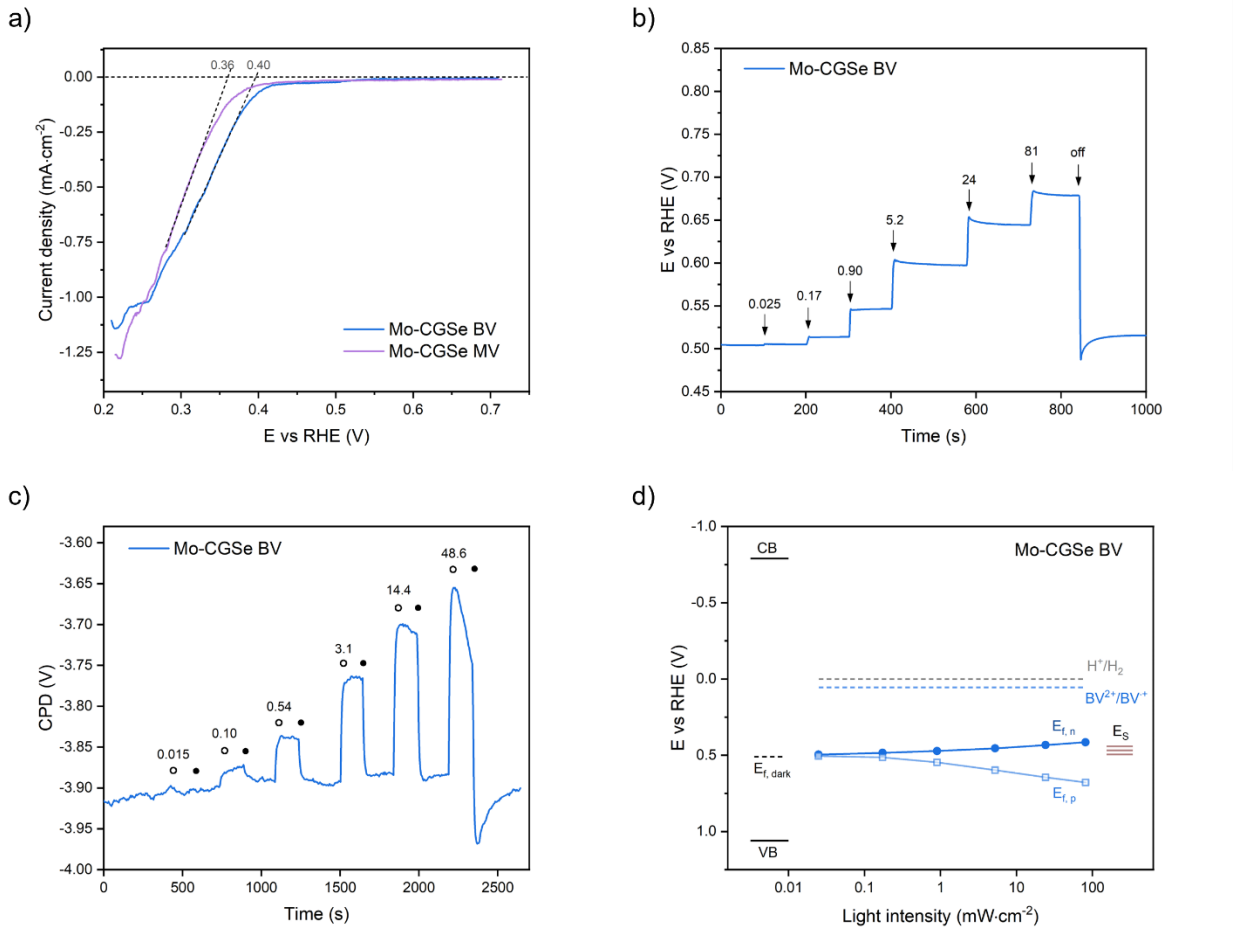

Figure 2.6. Data for the Mo-CGSe electrode with the electrolyte of 0.01 M $BVCl_2$ and 0.05 M sodium phosphate buffer (pH=7). (a) LSV scans under illumination (400 nm, 81 $mW \cdot cm^{-2}$). (b)(c) OCP and SPV data in the dark and under 400 nm monochromatic illumination of variable intensity (irradiances given in $mW \cdot cm^{-2}$). (d) QFLS plot based on the OCP and SPV results.

To further support the above analysis, another set of LSV, OCP and SPV measurements were performed on the Mo-CGSe electrode with the BV electrolyte (**Figure 2.6**). Benzyl viologen (BV^{2+}) has a slightly more positive reduction potential (-0.359 V_{NHE} / 0.055 V_{RHE}) than methyl viologen (MV^{2+}, -0.446 V_{NHE} / -0.032 V_{RHE}). Accordingly, a more positive photo-onset (BV: 0.40 V_{RHE}, MV: 0.36 V_{RHE}) is observed in the LSV curve (**Figure 2.6a**). The sizes of light induced SPV and OCP changes are similar to

that with the MV contact. Finally, **Figure 2.6d** shows the QFLS plot for the Mo-CGSe/BV system. Again, it is found that $E_{f,n}$ is pinned near the surface states under illumination.

Overall, the similar SPV data for the CGSe/NaPi and CGSe/MV, BV systems confirm that the low photovoltage of these junctions is not a result of a large proton reduction overpotential. Instead, it is a result of poor charge separation at the CGSe/liquid interfaces. The latter is not ideally controlled by the redox potential of the electrolyte, but instead by the potential of the surface states in CGSe. This is known as Fermi Level Pinning, which has been documented for many semiconductor electrodes.[16, 24, 31-35] In the case of CGSe, the pinning surface states could be gallium vacancies.[16] Our QFLS results suggest that they pin the Fermi level at around 0.5 eV above the valence band and limit the band bending that controls the electron hole separation. These surface states also trap electrons and can act as recombination sites for the holes, as shown in **Figure 2.7a**. This is causing the voltage loss during PEC water reduction and methyl viologen reduction. **Figure 2.7b** shows the increased band bending at a negative applied potential, that allows electrons to reduce protons. It explains why a cathodic bias is required for reduction of protons and methyl viologen, as seen in the PEC data in **Figure 2.2**.

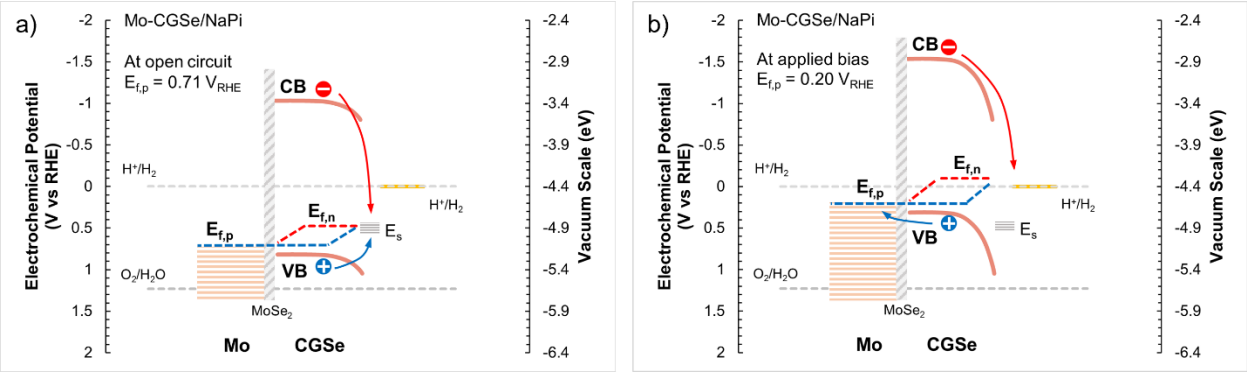

Figure 2.7 Energy diagram shows the band bending and QFLS of the Mo-CGSe/NaPi system under illumination (400 nm, 81 $mW \cdot cm^{-2}$). (a) At open circuit potential, $E_{f,p}$ = 0.71 V_{RHE} (from **Figure 2.3a**). (b) At an applied potential of 0.20 V_{RHE}. The increased band bending allows electrons to reduce protons.

In order to study the effect of the back contact on the internal photovoltage of CGSe electrode, a series of LSV, OCP and SPV measurements were performed on the FTO-CGSe and the Mo-CGSe electrodes. Transparent conductive oxide substrates, such as FTO, are used in the superstrate configuration of CIGS based solar cells, even though the electronic properties of the CIGS/FTO junction are inferior.[36-38] **Figure 2.8** shows energy diagrams for CGSe on Mo and FTO back contacts. A n-/p-junction forms at the FTO/CGSe interface, whereas the Mo/CGSe contact is ohmic due to the formation of a thin $MoSe_2$ layer at the Mo/CGSe interface during the high temperature absorber formation step.[39-41]

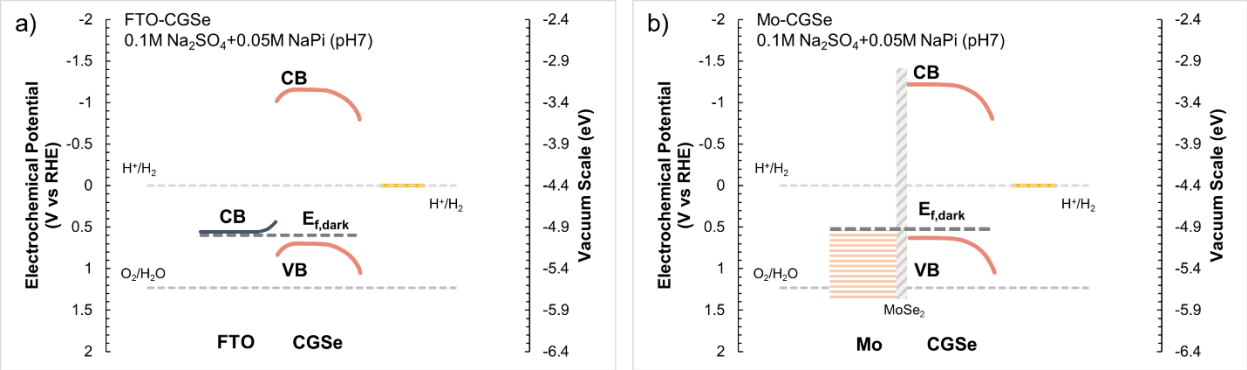

Figure 2.8. Energetics of the FTO-CGSe and the Mo-CGSe electrodes with liquid contact in the dark. A n-/p-junction forms at the FTO/CGSe interface, while the Mo/CGSe contact is ohmic.

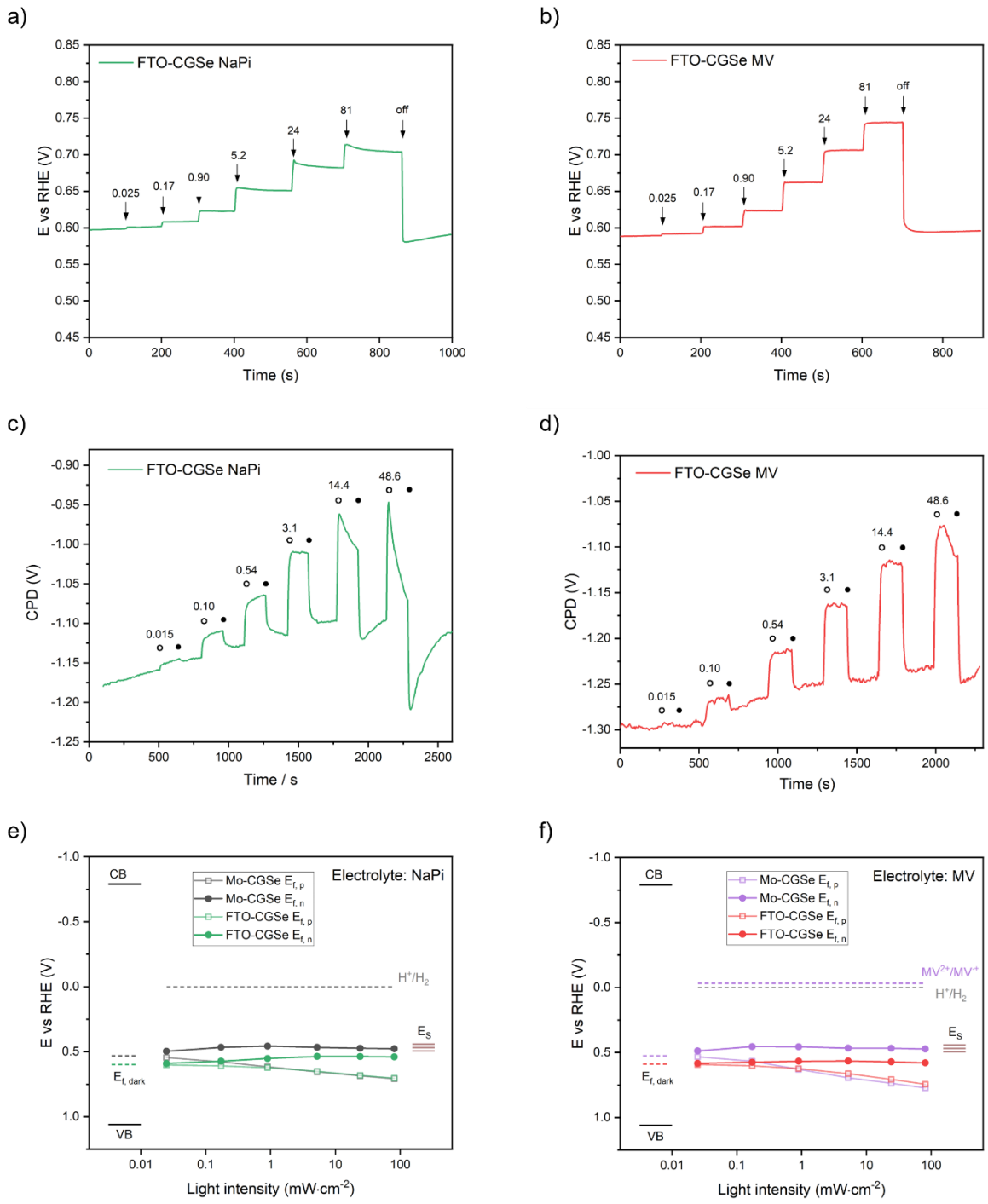

Figure 2.9 Data for the FTO-CGSe electrode. (a-d) OCP and SPV data in the dark and under 400 nm monochromatic illumination of variable intensity (irradiances given in mW·cm^{-2}). (a)(c) Electrolyte: NaPi. (b)(d) Electrolyte: MV. (e)(f) QFLS plots of the FTO-CGSe and the Mo-CGSe electrodes with electrolyte of NaPi and MV, respectively.

The OCP and SPV data for the FTO-CGSe electrode with NaPi and MV contacts are shown in **Figure 2.9a-d**, with the corresponding QFLS plots in **Figure 2.9ef**. LSV curves are shown in **Figure 2.10a** and **b**, for water reduction and MV^{2+} reduction, respectively. With a Mo back contact, the CGSe photocathode shows earlier onset and higher photocurrent density for both proton reduction and MV^{2+} reduction. This indicates higher photovoltage achievement for Mo-CGSe, compared to FTO-CGSe. This result is in consistent with the observed internal photovoltage (**Figure 2.9ef**). At the light intensity of 81 $mW \cdot cm^{-2}$, the internal photovoltage (the QFLS) is estimated to be 0.16 V for FTO-CGSe/NaPi, smaller than the 0.23 V for Mo-CGSe/NaPi. The increased QFLS of Mo-CGSe over FTO-CGSe applies to the entire range of illumination. This shows the superior properties of the Mo-CGSe configuration and confirms that the n-/p-junction at the FTO/CGSe interface acts as recombination center is the cause for the decrease of the photovoltage. This demonstrates that the surface photovoltage measurement is an effective method to evaluate the contribution of back contact to the quasi-Fermi level splitting in a thin film photoelectrode.

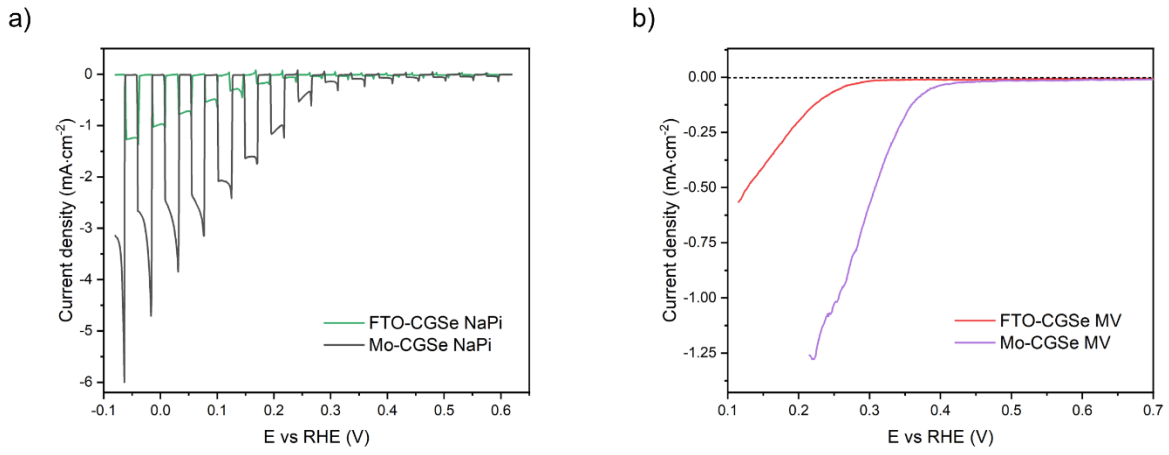

Figure 2.10 LSV scans of the FTO-CGSe and the Mo-CGSe electrodes under (chopped) illumination (400 nm, 81 $mW \cdot cm^{-2}$). (a) Electrolyte: NaPi. (b) Electrolyte: MV.

Potentially, the photovoltage loss at CGSe photocathodes from electron hole recombination at surface states can be overcome with surface treatments.[42-44] For example, surface pretreatment with Cd^{2+} solution before the deposition of buffer layers was reported improve the performance of $Cu(In,Ga)Se_2$, $CuInS_xSe_{2-x}$ or $CuGa_3Se_5$ based solar cells.[42-44] This was mainly attributed to surface Cd doping and the removal of surface oxide.[42, 44]

To investigate the effect of cadmium acetate solution treatment on QFLS of the Mo-CGSe electrode, the electrode was soaked in a 65 ºC 0.1 M cadmium acetate aqueous solution for 30 min, followed by washing. The resulting electrode is described as Mo-CGSe_Cd in the following. Surface Cd doping is confirmed by X-ray photoelectron spectroscopy (XPS) (**Figure 2.16** in the Appendix), similar to what was observed in the literature.[44] LSV, OCP and SPV measurements were performed on the Mo-CGSe_Cd electrode. The LSV curves and the corresponding QFLS plots are shown in **Figure 2.11**. Compared to the non-treated sample, the LSV curve shows no significant photo-onset difference for water reduction after soaking (**Figure 2.11a**). The photocurrent is slightly lower, probably due to slightly reduced active sites after soaking. For the MV^{2+} reduction, a 50 mV anodic shift of the photocurrent onset is observed after the soaking treatment (**Figure 2.11b**). This slightly increased external photovoltage for MV^{2+} reduction from PEC confirms that Cd^{2+} surface treatment changed the CGSe surface. However, the 0.05 V shift is small, as seen in the QFLS plot in **Figure 2.11c**. So, we conclude that aqueous cadmium acetate solution treatment does not significantly increase the internal photovoltage for CGSe photoelectrode with direct CGSe/electrolyte contact.

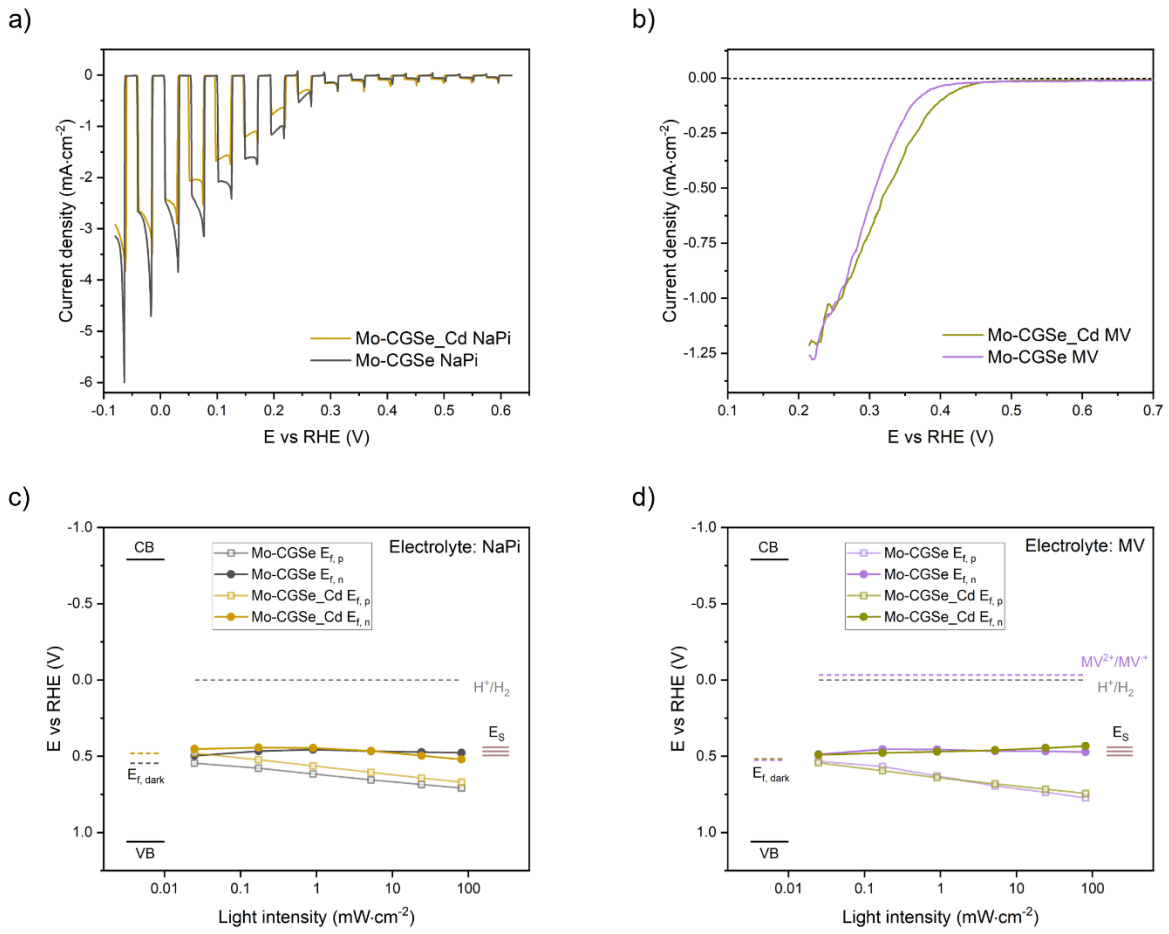

Figure 2.11 (a)(b) LSV scans of the Mo-CGSe_Cd and the Mo-CGSe electrodes under (chopped) illumination (400 nm, 81 mW·cm^{-2}) in the electrolyte of NaPi and MV, respectively. (c)(d) QFLS plots of the Mo-CGSe_Cd and the Mo-CGSe electrodes with electrolyte of NaPi and MV, respectively.

It is known that for Cu-based chalcogenide photocathodes, surface modification using a thin layer of n-type CdS to form a p–n heterojunction can produce anodically shifted onset potentials and larger cathodic photocurrents.[5, 15, 45-46] To test this in the present system, a thin layer of CdS was deposited on the surface of the Mo-CGSe electrode by the chemical bath deposition (CBD) method.[15] The sample after CdS deposition is noted as **Mo-CGSe/CdS** in the following. Photos, SEM and EDX mapping data (**Figure 2.17** in the Appendix) show that the CdS deposition is uniform and produces a thin layer of expected thickness of ~60 nm.[15] OCP and SPV measurements were performed on the Mo-CGSe/CdS

electrode with both NaPi and MV liquid contacts (**Figure 2.12a-d**). The resulting QFLS plot is shown in **Figure 2.12e** and **f**. It can be seen in both cases, that addition of the CdS layer moves the dark Fermi level to more reducing potential. This is a result of the negative Fermi energy of the CdS layer, as shown in **Figure 2.14**. The QFLS of the Mo-CGSe/CdS electrode shows an increase of 30-40%, compared to the bare Mo-CGSe, over the entire intensity range. This confirms improved charge separation at the CGSe – CdS interface. However, while the quasi-Fermi level of electrons shifts to negative energy, it still is not sufficient to reduce protons or MV^{2+} without applied negative bias. This is also confirmed by PEC measurements in **Figure 2.13**.

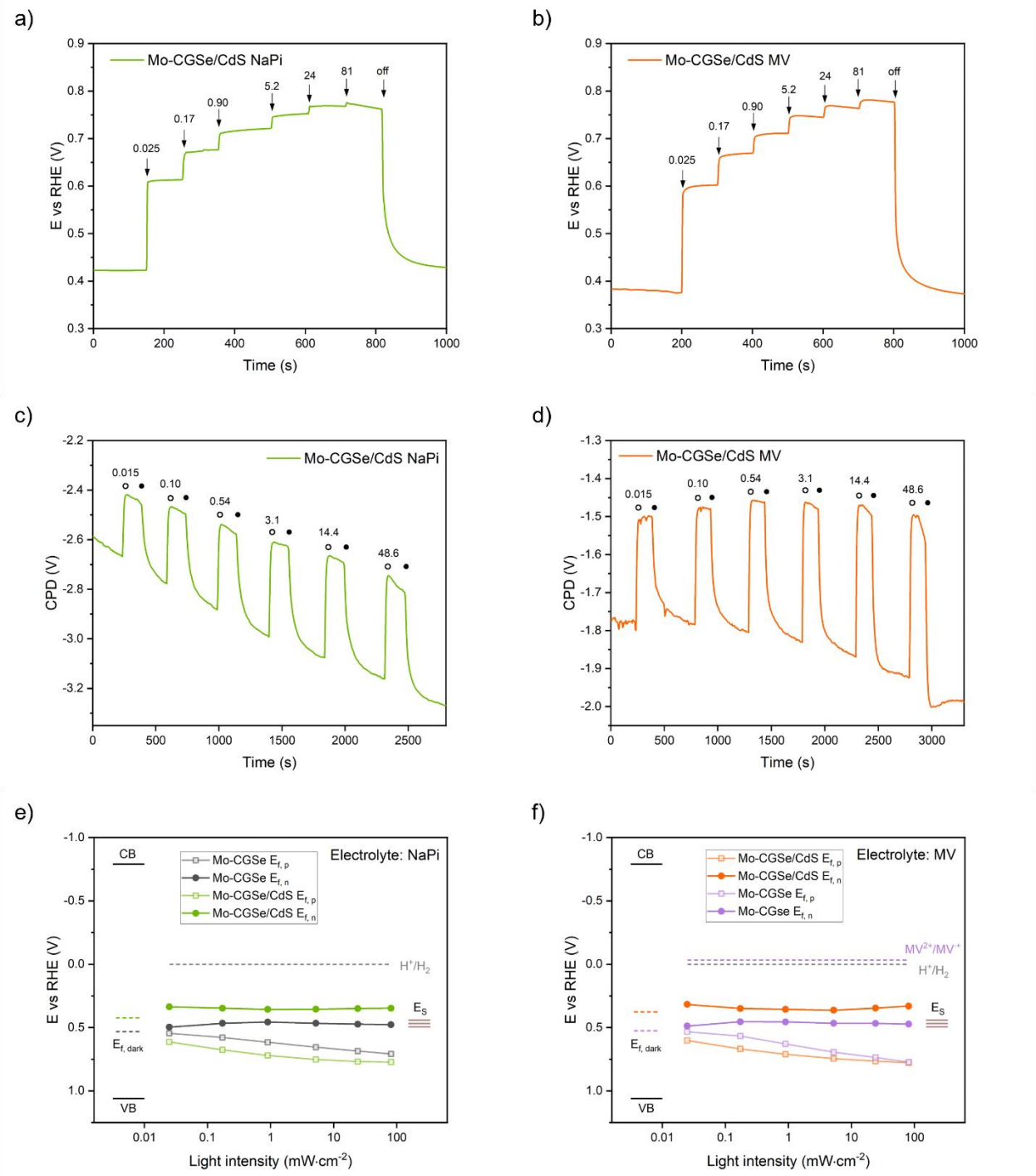

Figure 2.12 Data for the Mo-CGSe/CdS electrode. (a-d) OCP and SPV data in the dark and under 400 nm monochromatic illumination of variable intensity (irradiances given in mW·cm^{-2}). (a)(c) Electrolyte: NaPi. (b)(d) Electrolyte: MV. (e)(f) QFLS plots of the Mo-CGSe/CdS and the Mo-CGSe electrodes with electrolyte of NaPi and MV, respectively.

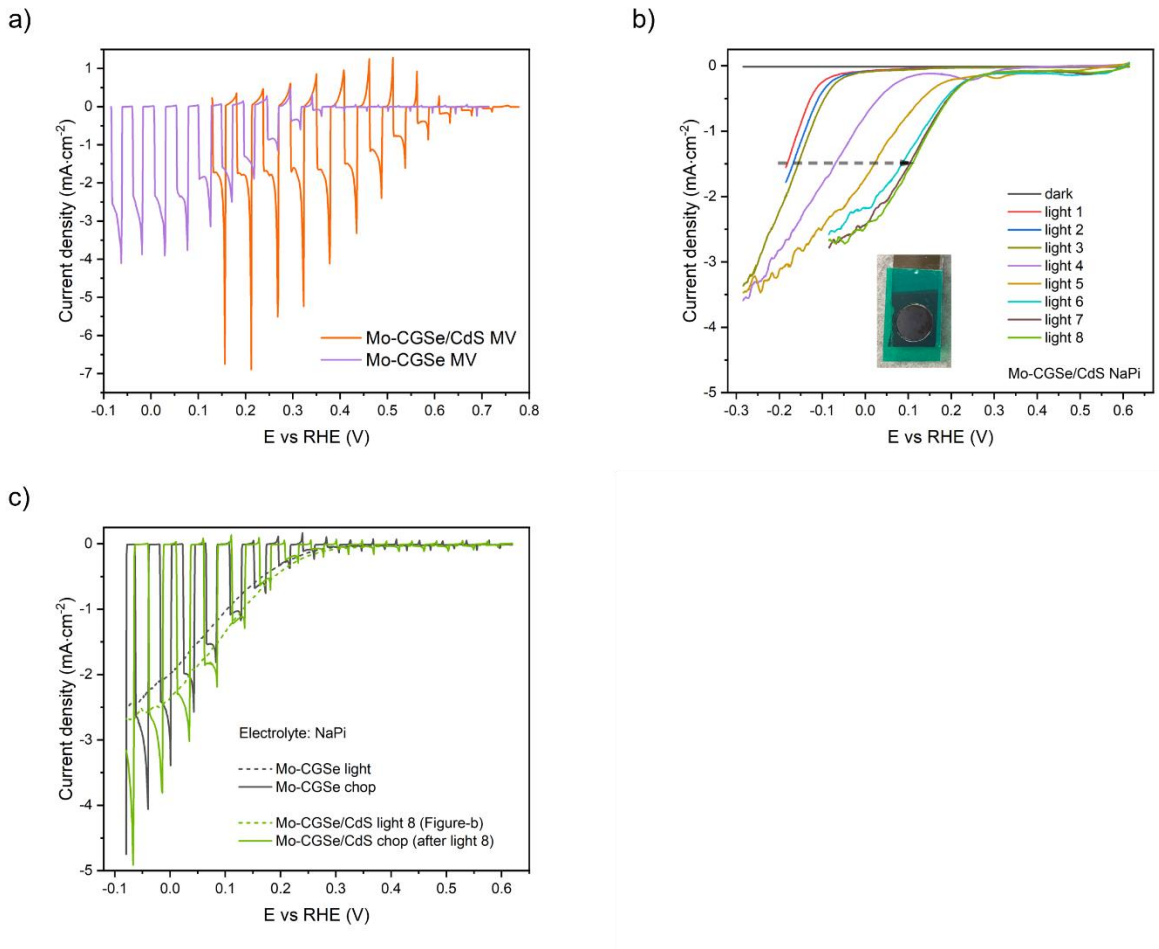

Figure 2.13 (a) LSV scans of the Mo-CGSe/CdS and the Mo-CGSe electrodes in the electrolyte of MV. (b) LSV curve of the Mo-CGSe/CdS electrode in NaPi electrolyte with repeating scans. Inserted photo: the electrode after repeated scans. (c) LSV curve of the Mo-CGSe/CdS electrode after repeated scans, compared with the bare Mo-CGSe, in NaPi electrolyte. Light source is 400 nm LED, with light intensity of 81 $mW \cdot cm^{-2}$. Electrolytes were de-aerated by continuous N_2 bubbling.

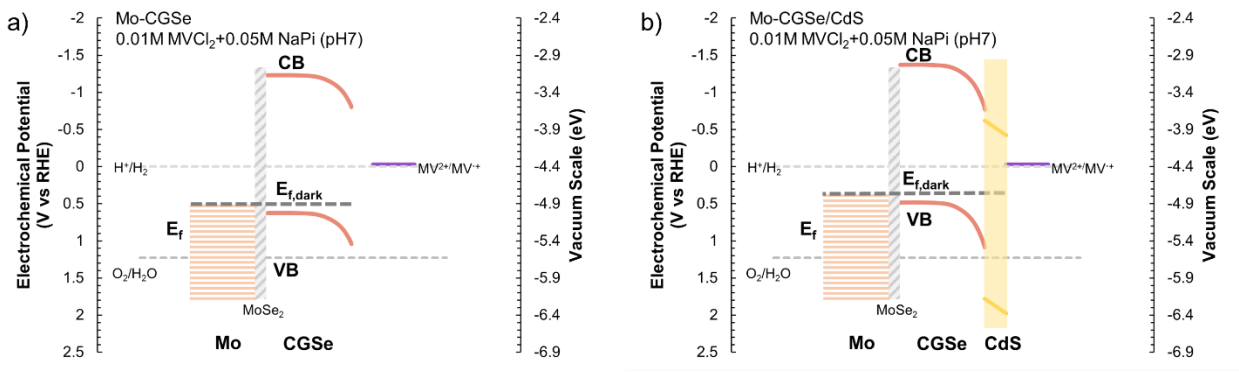

Figure 2.14 Energy diagram of (a) the Mo-CGSe electrode (b) the Mo-CGSe/CdS electrode with MV electrolyte contact, shows the band bending in the dark. A p-/n-junction forms at the CGSe/CdS interface. The band alignment at the CGSe/CdS interface were drawn based on the value reported in ref.[15]

The cathodic photocurrent for proton reduction begins at -0.10 V_{RHE}, shifted by 0.35 V to more negative potential compared to the bare Mo-CGSe electrode. When the scans are repeated, the photo-onset gradually shifts in anodic direction (**Figure 2.13c**) until it finally (light 8 scan) becomes equal to the bare Mo-CGSe electrode. At the same time, we observed that most of the top CdS layer was peeled off from the CGSe surface, as shown in the inserted photo in **Figure 2.13b**. These observations suggests that the performance of the Mo-CGSe/CdS system is limited by the unfavorable kinetics of proton reduction at the CdS surface. CdS is known to have a large overpotential for proton reduction.[47] As a result, proton reduction occurs at the CGSe layer, and the resulting H_2 bubbles peel off the CdS layer.

When the fast redox couple of MV^{2+}/MV^{+} is used, no reduction overpotential at the CdS layer should exist. Accordingly, in the Mo-CGSe/CdS system, the photo-onset for MV^{2+} reduction shift anodically from 0.35 V_{RHE} to 0.65 V_{RHE} (**Figure 2.13a**). MV^{2+} reduction is confirmed by observation of a purple color of the MV^{+} radical cation near the electrode. This confirms the improved performance of the Mo-CGSe/CdS photoelectrode for MV^{2+} reduction. Based on the PEC data, the CdS layer increases the external photovoltage to 0.68 V from 0.38 V for the bare Mo-CGSe photoelectrodes. This increase is larger than the internal photovoltage increase observed in SPV measurement (from 0.30 V to 0.45 V). As discussed in earlier parts, PEC method usually gives a larger photovoltage because there is an applied

potential in LSV measurements comparing to the open circuit condition in the SPV experiment. Considering this, the external photovoltage from PEC and the internal photovoltage (QFLS) from SPV are in good agreement.

Conclusions

For the first time, surface photovoltage (SPV) measurements were used to measure quasi-Fermi level splitting (QFLS) in $CuGa_3Se_5$ thin film photocathodes in contact with different electrolytes, different back contacts, and with surface passivation layers. For the non-passivated electrodes, Fermi level pinning near the surface states, 0.5 eV above the CGSe valence band was established as the cause for the voltage loss during photoelectrochemical water and methyl viologen reduction. The surface states both limited the band-bending at the CGSe/liquid interface, and they served as recombination centers for the electron/hole pairs. Application of a CdS passivation layer increases the internal photovoltage to 0.43 V for NaPi contact and 0.45 V for MV contact under 81 $mW \cdot cm^{-2}$ illumination. This increase is due to the passivation of the CGSe surface states and the formation of a p-/n-junction that promotes electron extraction from CGSe. Molybdenum was confirmed to be a better back contact to CGSe than FTO, based on the increased internal photovoltage (from 0.16 V to 0.23 V, NaPi electrolyte, light intensity of 81 $mW \cdot cm^{-2}$). This confirms the hypothesis that Mo acts as a hole selective contact at the CGSe back side. These findings improve our understanding of the factors that control charge carrier extraction from illuminated CGSe photoelectrodes. Additionally, the work establishes SPV as a powerful method to measure internal photovoltages in semiconductor/liquid junctions, and to identify charge selective contacts and passivation layers.

Experimental Section

Chemicals. Sodium phosphate monobasic monohydrate (≥99.0%, Sigma-Aldrich), sodium phosphate dibasic heptahydrate (98.0% - 102.0%, Sigma-Aldrich), sodium sulfate (≥99.0%, Sigma-Aldrich), methyl viologen dichloride hydrate (98%, Acros Organics) and benzyl viologen dichloride hydrate (>98.0%, TCI) were used for the preparation of the electrolytes. Cadmium acetate dihydrate (analytical reagent, Mallinckrodt), thiourea (99%, Alfa Aesar) and ammonium hydroxide (29.7%, certified ACS plus, Fisher Chemicals) were used for the cadmium sulfide chemical bath deposition. Potassium ferricyanide (99.2%, Sigma) and potassium hexacyanoferrate (II) trihydrate (98.0% - 102.0%, Sigma-Aldrich) were used as received. Water was purified to 18 MΩ·cm resistivity by a Nanopure system.

Scanning electron microscopy (SEM) and energy dispersive X-ray spectroscopy (EDX) were recorded using Scios DualBeam FIB/SEM.

pH of the electrolyte was measured with a pH meter (Fisher Scientific accumet AE150).

X-ray photoelectron spectroscopy (XPS) was conducted via Supra XPS spectrometer with Al Kα source that generate x-ray at 1487 eV. All analysis was done in the ultra-high vacuum (UHV) analytical chamber with the pressure of 10^{-7} mbar. The survey scan was conducted at constant pass energy of 40 eV with a scan step of 0.5 eV, and the high-resolution core-level spectra were recorded at constant pass energy of 40 eV with a scan step of 0.1 eV. The spectra were electrostatically corrected based on the position of C 1s (284.8 eV).

Cadmium treatment: Treatment method is modified from literature.[43-44] The film was soaked in a 65 ^{o}C 0.1 M cadmium acetate aqueous solution for 30 min. The film was rinsed with water afterwards.

CdS layer deposition: CdS layers were formed on the surface of CGSe films by the chemical bath deposition (CBD) method.[15] Prior to CdS deposition, the surface of the CGSe films was pretreated with an aqueous solution containing 2 M NH_4OH and 7.5 mM $Cd(CH_3COO)_2$ at 80°C for 10 min. CBD of

CdS was performed by immersing the Cd^{2+}-pretreated films in a bath solution containing 0.375 M $SC(NH_2)_2$, 7.5 mM $Cd(CH_3COO)_2$, and 2 M NH_4OH at 65°C for 5 min. After CdS deposition, the samples were annealed in air at 300°C for 60 min.

Surface photovoltage spectroscopy (SPS): Contact potential differences (CPD) were measured using a circular (2.5 mm diameter), semitransparent vibrating gold mesh disk (Kelvin Probe S, Besocke Delta Phi) controlled by a Kelvin Control 7 Oscillator/amplifier (Besocke Delta Phi) that mounted inside of a home-built vacuum chamber. Samples were placed approximately 1 mm underneath the Kelvin probe. 400 nm LED (LZC-00UA00, LedEngin) was used as the light source, irradiation power was controlled by a power supply (Naweisz NP6005). Light intensity was measured from a photometer (International Light IL1400BL) equipped with a SEL005 detector. SPS data was recorded every 5 seconds and by measuring the contact potential difference (CPD) value at each step. For liquid SPS measurements, 15 μL of the respective liquid electrolyte was dropped on the surface of the sample and then covered with a microscope cover glass (12 mm diameter, Fisherbrand). During the measurements, the chamber was continuously purged with a water saturated N_2 (flow rate of 0.02-0.10 SLPM) to suppress the evaporation of the electrolyte.

Photoelectrochemical Linear Sweep Voltammetry (LSV) Measurements: Electrochemical measurements were conducted using a Gamry Reference 600 Potentiostat connected to a typical three-electrode system, with a Pt counter electrode and a calomel reference electrode (3.5 M KCl). All the PEC measurements were performed with stirring and continuously N_2 purging. LSV scans were performed with a 10 mV/s scan rate in cathodic direction. The potentials in each measurement were converted to normal hydrogen electrode (NHE) by calibration with 10 mM $K_3Fe(CN)_6$/ $K_4Fe(CN)_6$. Potentials were adjusted to RHE with the following formula: $V_{RHE} = V_{NHE} + 0.0592 \times pH$. The same 400 nm LED described in the SPS measurements was used as the light source.

Open Circuit Potential (OCP) Measurements: A two-electrode setup was used in the OCP measurements by using the calomel electrode (3.5 M KCl) as the counter/reference electrode and the

CGSe electrode as working electrode. All OCP measurements were performed with stirring and continuously N_2 purging. The potentials in each measurement were converted into the values versus RHE, as described above. The same 400 nm LED light source was used.

Appendix

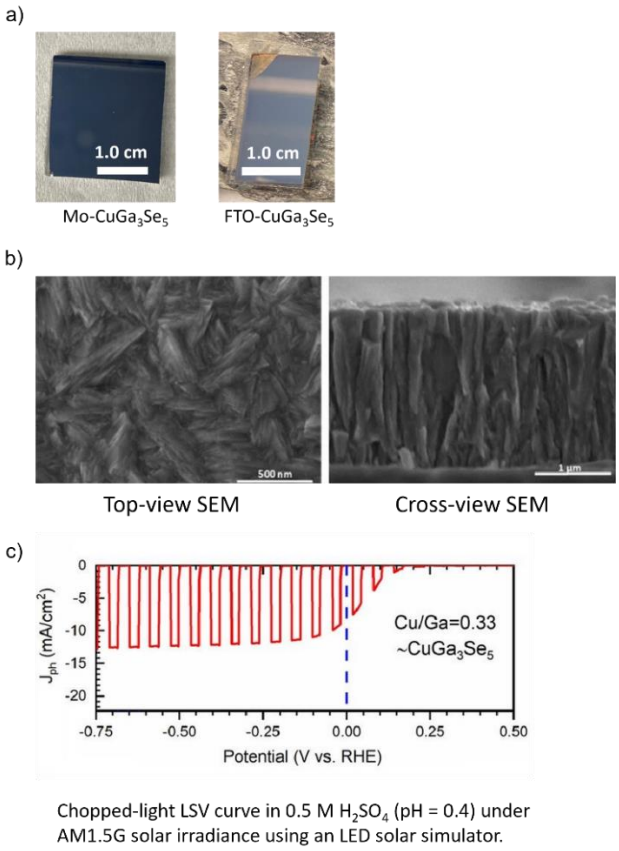

Figure 2.15 (a) Photos of the Mo-CGSe and FTO-CGSe electrodes. (b) SEM images of the Mo-CGSe electrode. (c) PEC data of the Mo-CGSe electrode. Adapted from reference[14] with permission from Elsevier, Copyright 2020.

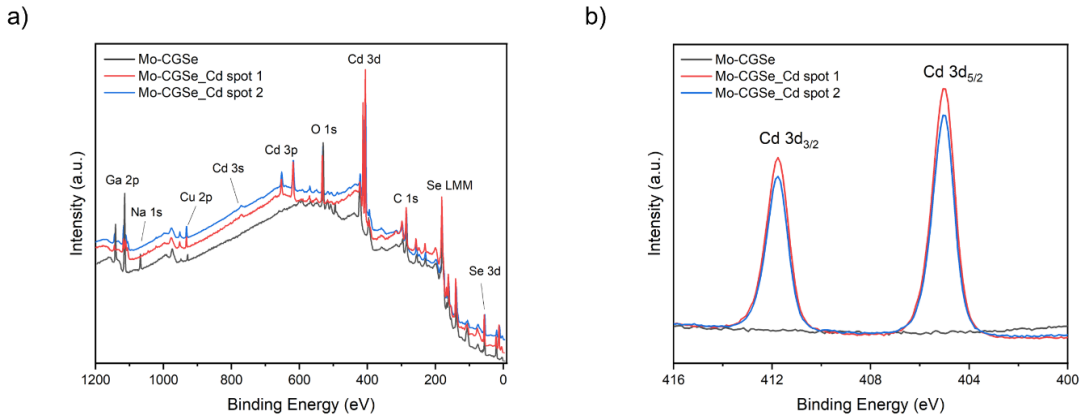

Figure 2.16 XPS data of Mo-CGSe and Mo-CGSe_Cd. (a) Survey spectrum. (b) Cd 3d region. This XPS data was obtained by Chengcan Xiao in the Osterloh lab.

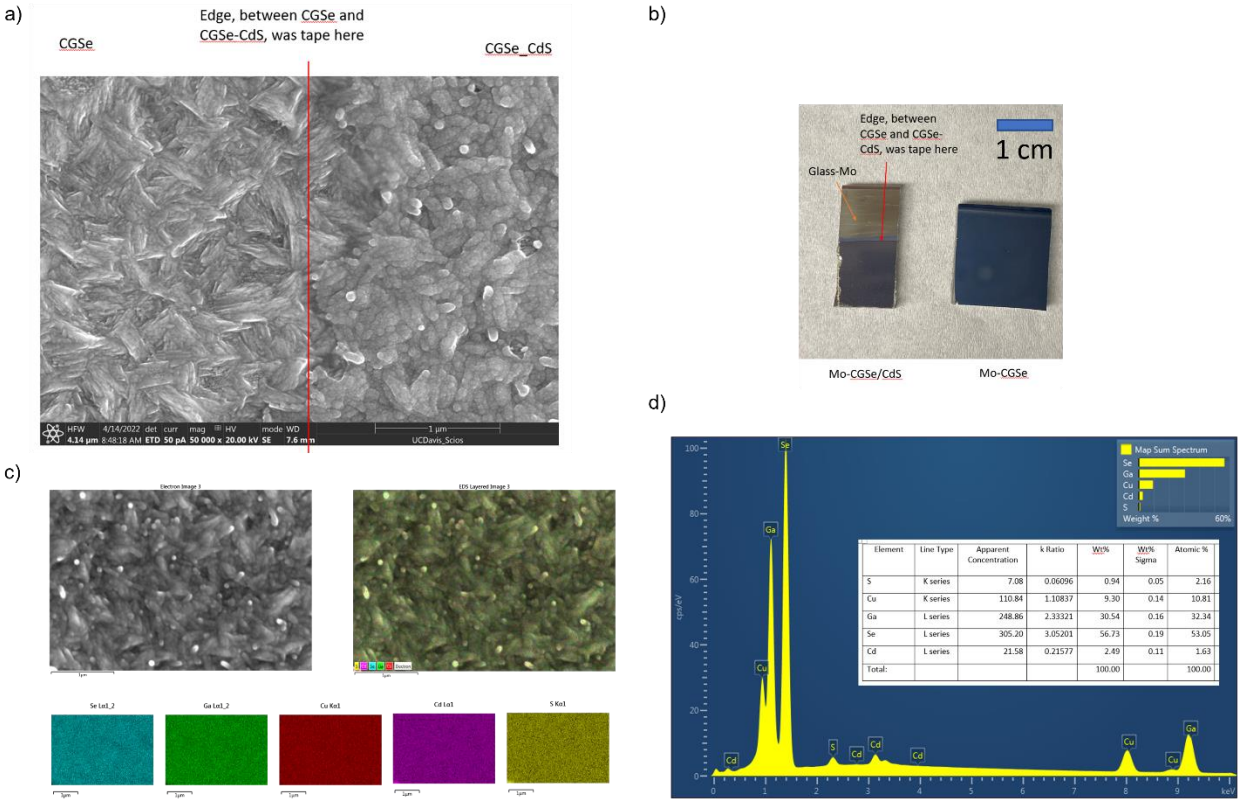

Figure 2.17 (a) Top-view SEM image of the Mo-CGSe/CdS electrode, showing the region where the left part is CGSe surface, and the right part is CGSe/CdS surface. It corresponds to the border marked in the photo. (b) Photos of the Mo-CGSe/CdS and the Mo-CGSe electrodes. (c)(d) EDS mapping, elemental spectrum, and quantification results of the Mo-CGSe/CdS surface.

References

1. Niki, S.; Contreras, M.; Repins, I.; Powalla, M.; Kushiya, K.; Ishizuka, S.; Matsubara, K., CIGS absorbers and processes. *Progress in Photovoltaics: Research and Applications* **2010,** *18* (6), 453-466.

2. Nakamura, M.; Yamaguchi, K.; Kimoto, Y.; Yasaki, Y.; Kato, T.; Sugimoto, H., Cd-Free $Cu(In,Ga)(Se,S)_2$ Thin-Film Solar Cell With Record Efficiency of 23.35%. *IEEE Journal of Photovoltaics* **2019,** *9* (6), 1863-1867.

3. Bär, M.; Bohne, W.; Röhrich, J.; Strub, E.; Lindner, S.; Lux-Steiner, M. C.; Fischer, C. H.; Niesen, T. P.; Karg, F., Determination of the band gap depth profile of the penternary $Cu(In_{(1-X)}Ga_X)(S_YSe_{(1-Y)})_2$ chalcopyrite from its composition gradient. *Journal of Applied Physics* **2004,** *96* (7), 3857-3860.

4. Marsen, B.; Cole, B.; Miller, E. L., Photoelectrolysis of water using thin copper gallium diselenide electrodes. *Solar Energy Materials and Solar Cells* **2008,** *92* (9), 1054-1058.

5. Moriya, M.; Minegishi, T.; Kumagai, H.; Katayama, M.; Kubota, J.; Domen, K., Stable hydrogen evolution from CdS-modified $CuGaSe_2$ photoelectrode under visible-light irradiation. *Journal of the American Chemical Society* **2013,** *135* (10), 3733-3735.

6. Gaillard, N.; Prasher, D.; Kaneshiro, J.; Mallory, S.; Chong, M., Development of Chalcogenide Thin Film Materials for Photoelectrochemical Hydrogen Production. *Materials Research Society Symposium Proceedings* **2013,** *1558* (1), mrss13-1558-z02-07.

7. Jacobsson, T. J.; Fjällström, V.; Sahlberg, M.; Edoff, M.; Edvinsson, T., A monolithic device for solar water splitting based on series interconnected thin film absorbers reaching over 10% solar-to-hydrogen efficiency. *Energy & Environmental Science* **2013,** *6* (12), 3676-3683.

8. Chen, Y.; Feng, X.; Liu, M.; Su, J.; Shen, S., Towards efficient solar-to-hydrogen conversion: Fundamentals and recent progress in copper-based chalcogenide photocathodes. *Nanophotonics* **2016,** *5* (4), 524-547.

9. Gaillard, N.; Prasher, D.; Chong, M.; Deangelis, A.; Horsley, K.; Ishii, H. A.; Bradley, J. P.; Varley, J.; Ogitsu, T., Wide-Bandgap Cu(In,Ga)S_2 Photocathodes Integrated on Transparent Conductive F:SnO_2 Substrates for Chalcopyrite-Based Water Splitting Tandem Devices. *ACS Applied Energy Materials* **2019,** *2* (8), 5515-5524.

10. Kobayashi, H.; Sato, N.; Orita, M.; Kuang, Y.; Kaneko, H.; Minegishi, T.; Yamada, T.; Domen, K., Development of highly efficient $CuIn_{0.5}Ga_{0.5}Se_2$-based photocathode and application to overall solar driven water splitting. *Energy & Environmental Science* **2018,** *11* (10), 3003-3009.

11. Kumagai, H.; Minegishi, T.; Sato, N.; Yamada, T.; Kubota, J.; Domen, K., Efficient solar hydrogen production from neutral electrolytes using surface-modified Cu(In,Ga)Se_2 photocathodes. *Journal of Materials Chemistry A* **2015,** *3* (16), 8300-8307.

12. Kim, J.; Minegishi, T.; Kobota, J.; Domen, K., Investigation of Cu-Deficient Copper Gallium Selenide Thin Film as a Photocathode for Photoelectrochemical Water Splitting. *Japanese Journal of Applied Physics* **2011,** *51* (1), 015802.

13. Muzzillo, C. P.; Klein, W. E.; Li, Z.; DeAngelis, A. D.; Horsley, K.; Zhu, K.; Gaillard, N., Low-Cost, Efficient, and Durable H_2 Production by Photoelectrochemical Water Splitting with $CuGa_3Se_5$ Photocathodes. *ACS Applied Materials & Interfaces* **2018,** *10* (23), 19573-19579.

14. Mahmoudi, B.; Caddeo, F.; Lindenberg, T.; Schneider, T.; Hölscher, T.; Scheer, R.; Maijenburg, A. W., Photoelectrochemical properties of Cu-Ga-Se photocathodes with compositions ranging from $CuGaSe_2$ to $CuGa_3Se_5$. *Electrochimica Acta* **2021,** *367*, 137183.

15. Zhang, L.; Minegishi, T.; Nakabayashi, M.; Suzuki, Y.; Seki, K.; Shibata, N.; Kubota, J.; Domen, K., Durable hydrogen evolution from water driven by sunlight using (Ag,Cu)$GaSe_2$ photocathodes modified with CdS and $CuGa_3Se_5$. *Chemical Science* **2015,** *6* (2), 894-901.

16. Liu, Y.; Bouri, M.; Yao, L.; Xia, M.; Mensi, M.; Grätzel, M.; Sivula, K.; Aschauer, U.; Guijarro, N., Identifying Reactive Sites and Surface Traps in Chalcopyrite Photocathodes. *Angewandte Chemie International Edition* **2021,** *60* (44), 23651-23655.

17. Anantharaj, S.; Amarnath, T. S.; Subhashini, E.; Chatterjee, S.; Swaathini, K. C.; Karthick, K.; Kundu, S., Shrinking the Hydrogen Overpotential of Cu by 1 V and Imparting Ultralow Charge Transfer Resistance for Enhanced H_2 Evolution. *ACS Catalysis* **2018,** *8* (7), 5686-5697.

18. Zhang, W.; Fu, D.; Bai, Y.; Yuan, C., In-situ anion exchange synthesis of copper selenide electrode as electrocatalyst for hydrogen evolution reaction. *International Journal of Hydrogen Energy* **2017,** *42* (16), 10925-10930.

19. Tan, S. M.; Chua, C. K.; Sedmidubský, D.; Sofer, Z.; Pumera, M., Electrochemistry of layered GaSe and GeS: applications to ORR, OER and HER. *Physical Chemistry Chemical Physics* **2016,** *18* (3), 1699-1711.

20. Chun, S.-E.; Evanko, B.; Wang, X.; Vonlanthen, D.; Ji, X.; Stucky, G. D.; Boettcher, S. W., Design of aqueous redox-enhanced electrochemical capacitors with high specific energies and slow self-discharge. *Nature Communications* **2015,** *6* (1), 7818.

21. Bird, C. L.; Kuhn, A. T., Electrochemistry of the viologens. *Chemical Society Reviews* **1981,** *10* (1), 49-82.

22. Lide, D. R., *CRC handbook of chemistry and physics*. CRC Press: 2004; Vol. 85.

23. Wang, J.; Osterloh, F. E., Limiting factors for photochemical charge separation in $BiVO_4/Co_3O_4$, a highly active photocatalyst for water oxidation in sunlight. *Journal of Materials Chemistry A* **2014,** *2* (24), 9405-9411.

24. Bard, A. J.; Bocarsly, A. B.; Fan, F. R. F.; Walton, E. G.; Wrighton, M. S., The concept of Fermi level pinning at semiconductor/liquid junctions. Consequences for energy conversion efficiency and selection of useful solution redox couples in solar devices. *Journal of the American Chemical Society* **1980,** *102* (11), 3671-3677.

25. Dittrich, T.; Fengler, S., *Surface Photovoltage Analysis of Photoactive Materials*. World Scientific Publishing Europe Ltd.: 2020.

26. Kronik, L.; Shapira, Y., Surface photovoltage phenomena: theory, experiment, and applications. *Surface Science Reports* **1999,** *37*, 1-206.

27. Rühle, S.; Cahen, D., Contact-free photovoltage measurements of photoabsorbers using a Kelvin probe. *Journal of Applied Physics* **2004,** *96* (3), 1556-1562.

28. Zhao, J.; Osterloh, F. E., Photochemical Charge Separation in Nanocrystal Photocatalyst Films: Insights from Surface Photovoltage Spectroscopy. *Journal of Physical Chemistry Letters* **2014,** *5* (5), 782-786.

29. Melo, M. A.; Wu, Z.; Nail, B. A.; De Denko, A. T.; Nogueira, A. F.; Osterloh, F. E., Surface Photovoltage Measurements on a Particle Tandem Photocatalyst for Overall Water Splitting. *Nano Letters* **2018,** *18* (2), 805-810.

30. Gerischer, H., Electrochemical Behavior of Semiconductors under Illumination. *Journal of the Electrochemical Society* **1966,** *113* (11), 1174-1182.

31. Hinkle, C. L.; Milojevic, M.; Brennan, B.; Sonnet, A. M.; Aguirre-Tostado, F. S.; Hughes, G. J.; Vogel, E. M.; Wallace, R. M., Detection of Ga suboxides and their impact on III-V passivation and Fermi-level pinning. *Applied Physics Letters* **2009,** *94* (16), 162101.

32. Klahr, B.; Gimenez, S.; Fabregat-Santiago, F.; Hamann, T.; Bisquert, J., Water Oxidation at Hematite Photoelectrodes: The Role of Surface States. *Journal of the American Chemical Society* **2012,** *134* (9), 4294-4302.

33. Jang, Y. J.; Lee, J. S., Photoelectrochemical Water Splitting with p-Type Metal Oxide Semiconductor Photocathodes. *ChemSusChem* **2019,** *12* (9), 1835-1845.

34. Liu, Y.; Le Formal, F.; Boudoire, F.; Yao, L.; Sivula, K.; Guijarro, N., Insights into the interfacial carrier behaviour of copper ferrite ($CuFe_2O_4$) photoanodes for solar water oxidation. *Journal of Materials Chemistry A* **2019,** *7* (4), 1669-1677.

35. Lichterman, M. F.; Hu, S.; Richter, M. H.; Crumlin, E. J.; Axnanda, S.; Favaro, M.; Drisdell, W.; Hussain, Z.; Mayer, T.; Brunschwig, B. S.; Lewis, N. S.; Liu, Z.; Lewerenz, H.-J., Direct observation of the energetics at a semiconductor/liquid junction by operando X-ray photoelectron spectroscopy. *Energy & Environmental Science* **2015,** *8* (8), 2409-2416.

36. Haug, F. J.; Rudmann, D.; Romeo, A.; Zogg, H.; Tiwari, A. N.; Eth In *Electrical properties of the heterojunction in Cu(In,Ga)Se_2 superstrate solar cells*, 3rd World Conference on Photovoltaic Energy Conversion, Osaka, JAPAN, May 11-18; Osaka, JAPAN, 2003; pp 2853-2858.

37. Park, S. J.; Lee, E.; Jeon, H. S.; Ahn, S. J.; Oh, M.-K.; Min, B. K., A comparative study of solution based CIGS thin film growth on different glass substrates. *Applied Surface Science* **2011,** *258* (1), 120-125.

38. Mazzer, M.; Rampino, S.; Spaggiari, G.; Annoni, F.; Bersani, D.; Bissoli, F.; Bronzoni, M.; Calicchio, M.; Gombia, E.; Kingma, A.; Pattini, F.; Gilioli, E., Bifacial CIGS solar cells grown by Low Temperature Pulsed Electron Deposition. *Solar Energy Materials and Solar Cells* **2017,** *166*, 247-253.

39. Kohara, N.; Nishiwaki, S.; Hashimoto, Y.; Negami, T.; Wada, T., Electrical properties of the Cu(In,Ga)Se_2/$MoSe_2$/Mo structure. *Solar Energy Materials and Solar Cells* **2001,** *67* (1), 209-215.

40. Abou-Ras, D.; Kostorz, G.; Bremaud, D.; Kalin, M.; Kurdesau, F. V.; Tiwari, A. N.; Dobeli, M., Formation and characterisation of $MoSe_2$ for Cu(In,Ga)Se_2 based solar cells. *Thin Solid Films* **2005,** *480*, 433-438.

41. Yoon, J. H.; Kim, J. H.; Kim, W. M.; Park, J. K.; Baik, Y. J.; Seong, T. Y.; Jeong, J. H., Electrical properties of CIGS/Mo junctions as a function of $MoSe_2$ orientation and Na doping. *Progress in Photovoltaics* **2014,** *22* (1), 90-96.

42. Contreras, M. A.; Romero, M. J.; To, B.; Hasoon, F.; Noufi, R.; Ward, S.; Ramanathan, K., Optimization of CBD CdS process in high-efficiency Cu(In,Ga)Se_2-based solar cells. *Thin Solid Films* **2002,** *403-404*, 204-211.

43. Lei, B.; Hou, W. W.; Li, S. H.; Yang, W. B.; Chung, C. H.; Yang, Y., Cadmium ion soaking treatment for solution processed $CuInS_xSe_{2-x}$ solar cells and its effect on defect properties. *Solar Energy Materials and Solar Cells* **2011,** *95* (8), 2384-2389.

44. Khan, I. S.; Muzzillo, C. P.; Perkins, C. L.; Norman, A. G.; Young, J. L.; Gaillard, N.; Zakutayev, A., $Mg_xZn_{1-x}O$ contact to $CuGa_3Se_5$ absorber for photovoltaic and photoelectrochemical devices. *Journal of Physics: Energy* **2021,** *3* (2), 024001.

45. Hayashi, T.; Niishiro, R.; Ishihara, H.; Yamaguchi, M.; Jia, Q. X.; Kuang, Y. B.; Higashi, T.; Iwase, A.; Minegishi, T.; Yamada, T.; Domen, K.; Kudo, A., Powder-based $(CuGa_{1-y}In_y)_{(1-x)}Zn_{2x}S_2$ solid solution photocathodes with a largely positive onset potential for solar water splitting. *Sustainable Energy & Fuels* **2018,** *2* (9), 2016-2024.

46. Kaneko, H.; Minegishi, T.; Domen, K., Recent Progress in the Surface Modification of Photoelectrodes toward Efficient and Stable Overall Water Splitting. *Chemistry-a European Journal* **2018,** *24* (22), 5697-5706.

47. Sahu, N.; Upadhyay, S. N.; Sinha, A. S. K., Kinetics of reduction of water to hydrogen by visible light on alumina supported Pt-CdS photocatalysts. *International Journal of Hydrogen Energy* **2009,** *34* (1), 130-137.

Chapter 3 Factors Limiting p-type Copper Gallium Selenide as a Particulate Photocatalyst for Hydrogen Evolution

Introduction

Sunlight-driven water splitting with photocatalysts is a potential scalable, low-cost approach to hydrogen fuel production.[1-7] Tandem photocatalysts combining separate hydrogen evolution photocatalyst (HEP) and oxygen evolution photocatalyst (OEP) achieve maximum light utilization.[8-11] One of the most efficient photocatalysts is a tandem system with $SrTiO_3$:La, Rh and $BiVO_4$:Mo powders embedded in a gold layer. It achieves 1.1% solar-to-hydrogen (STH) conversion efficiency.[12] As discussed in Chapter 1, the development of narrow bandgap HEP that can harvest a larger portion of the solar spectrum is needed to further increase the efficiency of such tandems.

Chalcopyrites of the formula $Cu(In,Ga)(Se,S)_2$ (CIGS) are suitable for this purpose, due to their narrow bandgaps (1.0 – 2.2 eV), their tunable band structures and high absorption coefficients.[13-17] Among these, copper gallium selenides (CGSe) is most suitable for PEC water reduction,[18-23] because of its favorable conduction band edge. This is illustrated for $CuGa_3Se_5$ **Figure 3.1**.

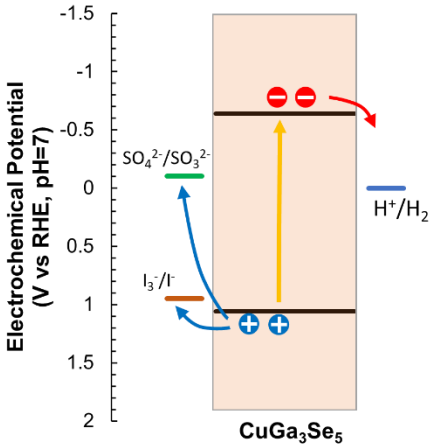

Figure 3.1 Energy band positions of $CuGa_3Se_5$ with proton reduction potential and sacrificial donor (iodide/ sulfite) standard reduction potentials. Positions of the valence band (VB) and conduction band (CB) were drawn based on a reported VB position in ref,[23] and considering a bulk bandgap of 1.7 eV measured later in the Chapter.

Electrodes prepared from particulate CGSe were achieve efficient PEC water reduction (cathodic photocurrent 9.3 $mA \cdot cm^{-2}$ at 0 V_{RHE}) after proper surface modifications.[21] To date, reports of the application of CGSe in particulate photocatalytic water splitting are limited. However, in 2019 the Domen group reported the use of solid solutions of ZnSe and CGSe (ZnSe:CGSe) combined with $BiVO_4$ embedded in a gold layer, as photocatalyst sheet for overall water splitting, with STH energy conversion efficiency of 0.01%.[24] A similar ZnSe:CGSe system was constructed from reduced graphene oxide as electron mediator.[25] In 2020, single-crystalline ZnSe:CGSe with optimized cocatalyst composite showed apparent quantum yield (AQY) of 13.7% at 420 nm during H_2 evolution reaction with sulfide and sulfite ions as sacrificial electron donors.[26] In contrast, CGSe shows much lower activity (7 $\mu mol \cdot h^{-1}$ for $CuGa_5Se_8$ with same electron donors, corresponding to 0.05% AQY at 420 nm)[25] for photocatalytic water reduction. This activity is far below the theoretical limit of 0.86 $mmol \cdot h^{-1} \cdot cm^{-2}$ for this compound, based on its 1.7 eV band gap and 100% quantum efficiency.

Therefore, the purpose of this work is to study CGSe as a particulate photocatalyst for water reduction and to investigate the reasons for the low activity. We hypothesize that defect states and inefficient charge separation were responsible for the low photocatalytic activity. To test this, surface photovoltage spectroscopy is applied to measure the charge separation ability and charge separation reversibility in CGSe particles in contact electron and hole selective materials. The effectiveness of charge selective contacts and layers is also studied with the CGSe particle films.

Results and Discussion

Copper gallium selenide ($CuGa_xSe_y$, abbreviated as CGSe) powders with different Ga/Cu ratios (x = 1 or 3) were synthesized via a solid-state reaction of Cu_2Se and Ga_2Se_3 according to the literature.[21] The powder X-ray diffraction (PXRD) pattens are shown in **Figure 3.2**. All diffraction peaks of CGSe with Ga/Cu of ratio 1 can be assigned to the chalcopyrite phase $CuGaSe_2$. The most prominent peak at 27.6° is due to the (112) diffraction. The peaks of CGSe with Ga/Cu of ratio 3 were assigned to the ordered-defect chalcopyrite phase $CuGa_3Se_5$.[27]

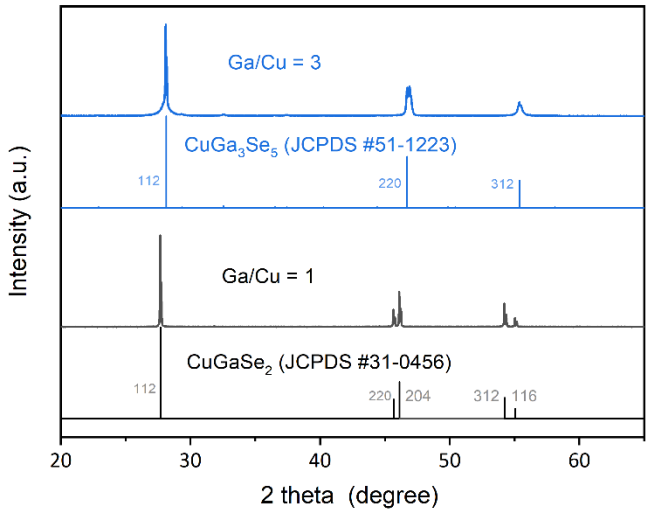

Figure 3.2 Powder X-ray diffraction patterns of synthesized CGSe with Ga/Cu ratio of 1 and 3. All doublets (2:1) of the peaks are due to X-ray source Cu Kα1 and Kα2 (2:1 ratio).[28] The broadening of the peak at 46 degrees in $CuGa_3Se_5$, has been previously observed in XRD patterns.[21-22, 24] It is likely associated with the presence of more copper deficient compositions.

Figure 3.3 shows the SEM images of $CuGaSe_2$ and $CuGa_3Se_5$ particles. For $CuGaSe_2$, most of the particles are several tens of micrometers in size. For $CuGa_3Se_5$, the particles range from submicrometers to micrometers. Those polycrystalline particles do not have well-defined facets. This is because they were obtained by breaking up a polycrystalline chunk from the solid-state synthesis.

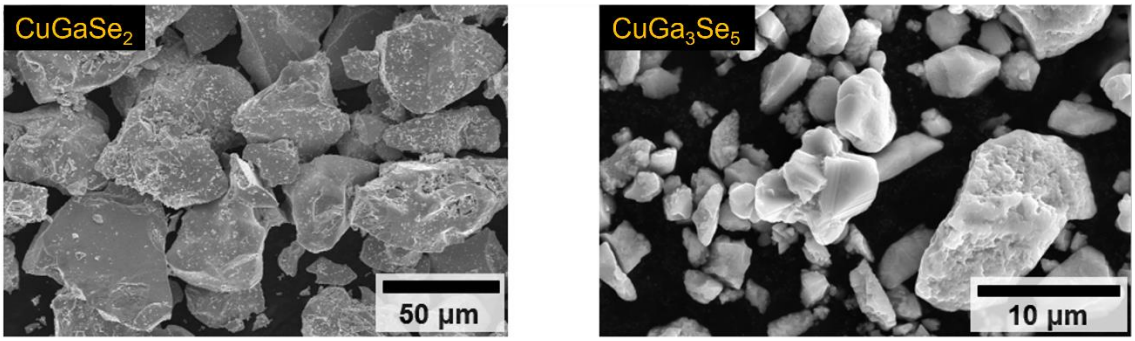

Figure 3.3 SEM images of $CuGaSe_2$ and $CuGa_3Se_5$ powders obtained by grinding the polycrystalline melt from the solid-state synthesis.

The CGSe powder powders look black grey in color. The optical absorption properties of the CGSe samples were examined by UV-vis diffuse reflectance spectroscopy, as shown in **Figure 3.4**. From the absorption edges, the band gaps were estimated to be 1.55 eV (800 nm) for $CuGaSe_2$ and 1.70 eV (728 nm) for $CuGa_3Se_5$, which are consistent with the reported values.[20] Additionally, $CuGaSe_2$ shows a tail in the absorption spectrum. This can be explained by the Cu(0) defects and increased interband transitions due to a slightly Cu-rich composition.[29]

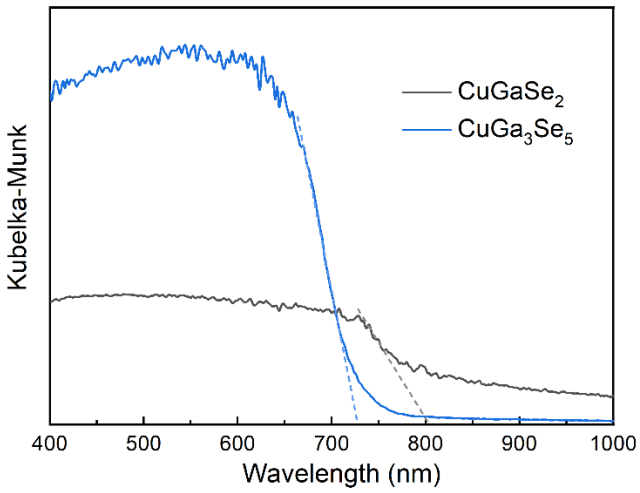

Figure 3.4 Kubelka-Munk-transformed UV−vis diffuse reflectance spectra of $CuGaSe_2$ and $CuGa_3Se_5$ powders.

CGSe particle films were then prepared on fluorine-doped tin oxide (FTO) substrates by drop-casting, followed by annealing under argon at 500 ºC for 2h to enhance the electric contact. An SEM image of the $CuGa_3Se_5$ film is shown in **Figure 3.19** in the Appendix. The film is not a compact layered film, as the CGSe particles are not uniformly covering the FTO. This is common for particle films made from inhomogeneous particles with large particle domains.

To study the photophysics of the FTO/CGSe system, surface photovoltage (SPV) spectra were recorded on the above films. The SPV spectra are shown in **Figure 3.5**, together with the corresponding UV−vis spectra. The positive photovoltage signals (black and blue solid line) for both samples can be assigned to transfer of photogenerated holes into the substate and photogenerated electrons into CGSe surface states (**Figure 3.6**). These states are likely related to reduced Ga(3+) and Cu(+) ions, although convincing experimental evidence is not yet available.[30-31] Based on results (surface pinning states) in Chapter 2, E_s is ~0.5 eV above the valence band. The positive SPV signal confirms that holes are the majority carriers and that the synthesized $CuGaSe_2$ and $CuGa_3Se_5$ are p-type. The effective bandgap can be estimated based on the extrapolation of the tangent of the major photovoltage signal. For $CuGa_3Se_5$, the effective bandgap is 1.6 eV, which is slightly smaller than the optical bandgap of 1.7 eV. This is attributed to the sub-bandgap states in $CuGa_3Se_5$ that are further discussed later in the chapter. For $CuGaSe_2$ the effective bandgap is 2.2 eV, much larger than the optical bandgap (1.55 eV). This indicates that the charge separation in $CuGaSe_2$ is relatively inefficient near the bandgap. This might be due to electron-hole recombination at a copper induced defect band located 0.1-0.4 eV below the conduction band, as shown in **Figure 3.6b**. The defect band was previously identified with photoluminescence and transient spectroscopy studies [32-35] It is likely due to copper interstitial defects (Cu_i).[31, 36] These states likely also affect the photocatalytic activity, as discussed below. Above 3.6 eV, the photovoltage is diminished because of the lower intensity of the Xe lamp at this photon energy (emission spectrum in **Figure 3.20** in the appendix). For $CuGa_3Se_5$, the small SPV signal at 1.25 eV - 1.6 eV is also attributed to the sub-

bandgap states of unknown origin (see discussion below).

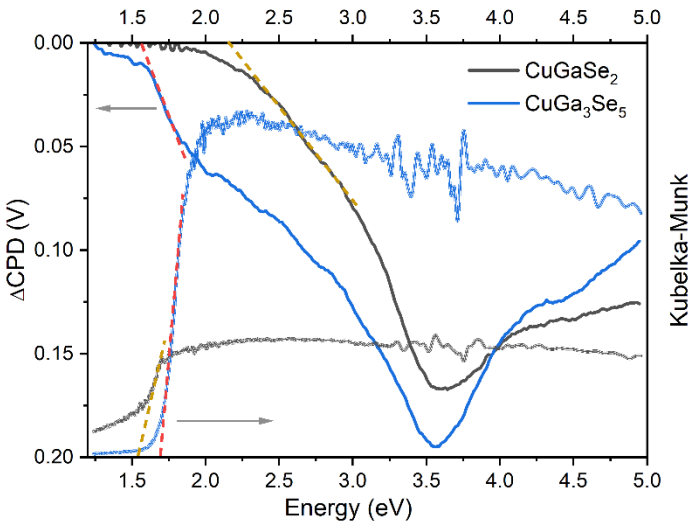

Figure 3.5 SPV spectra of $CuGaSe_2$ and $CuGa_3Se_5$ particle films on FTO, together with UV-vis spectra (back and blue short dash lines). Note: the y-axis for the ΔCPD values is inverted to allow better comparison with the UV-vis spectra.

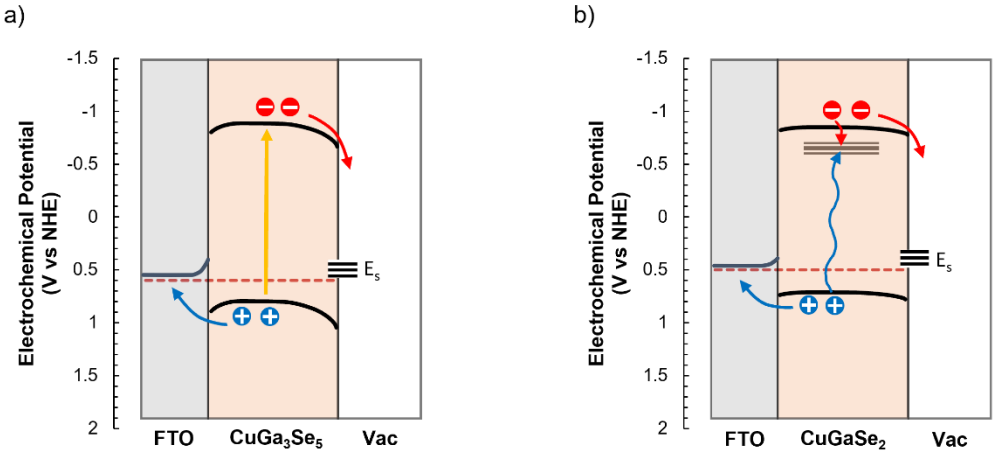

Figure 3.6 Energy diagram shows charge separation during SPV measurements for (a) $CuGa_3Se_5$ and (b) $CuGaSe_2$. Under illumination, photogenerated holes inject into the substrate and electrons move to the surface states of energy E_s. For $CuGaSe_2$, interband states located 0.1-0.4 eV below the conduction

band have been documented in the literature.[32-35] Electron-hole recombination at these defects will reduce the SPV signal.

To examine the photoelectrochemical (PEC) water reduction ability of the synthesized CGSe, linear sweep voltammetry (LSV) measurements were performed on the particle film electrodes immersed in 0.1 M Na_2SO_4 electrolyte and subjected to visible light illumination (**Figure 3.7a**). Both $CuGaSe_2$ and $CuGa_3Se_5$ electrodes generate weak cathodic photocurrents (5~20 $\mu A \cdot cm^{-2}$) under illumination. The origin of the photocurrent is likely proton reduction, although no H_2 bubbles were observed due to the weak current. $CuGa_3Se_5$ shows a superior PEC performance than $CuGaSe_2$, which is attributed to improved charge separation also seen in the SPV signal. For the drop-casted particle films, high resistance and inefficient charge transfer at FTO/CGSe contacts and at the CGSe/liquid interface are responsible for the overall small size of the photocurrent. The comparable dark current observed during the chopped light LSV scan is attributed to the exposed FTO surface of the particle films. This is more pronounced for $CuGaSe_2$ which has larger particle sizes and less coverage on the FTO.

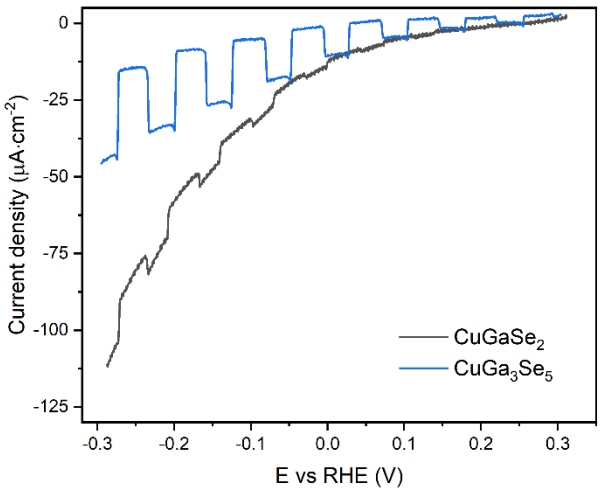

Figure 3.7 Linear sweep voltammetry (LSV) curves for $CuGaSe_2$ and $CuGa_3Se_5$ particle film electrodes on FTO. 0.1 M Na_2SO_4(aq) and a 300 W Xe lamp equipped with 400 nm long pass filters were used as the electrolyte and light source, respectively. Visible light intensity is 150 $mW \cdot cm^{-2}$.

To study the ability of the CGSe powders to function as proton reduction photocatalyst, Pt nanoparticle cocatalysts were loaded by impregnation, followed by annealing at 450 ºC in argon for 3h. For the related Cu_2Se [37-38] and for layered GaSe,[39] proton reduction overpotentials were reported to be 0.8 V and near 0.3 V, respectively. Therefore, Pt cocatalysts were loaded here to reduce the overpotential. **Figure 3.8** shows the SEM and energy dispersive X-ray spectroscopy (EDX) mapping of Pt-loaded $CuGa_3Se_5$. It confirms that that the Pt was successful loaded on the CGSe particles. The mapping result shows that Pt prefers to be loaded on the CGSe particles with smaller size.

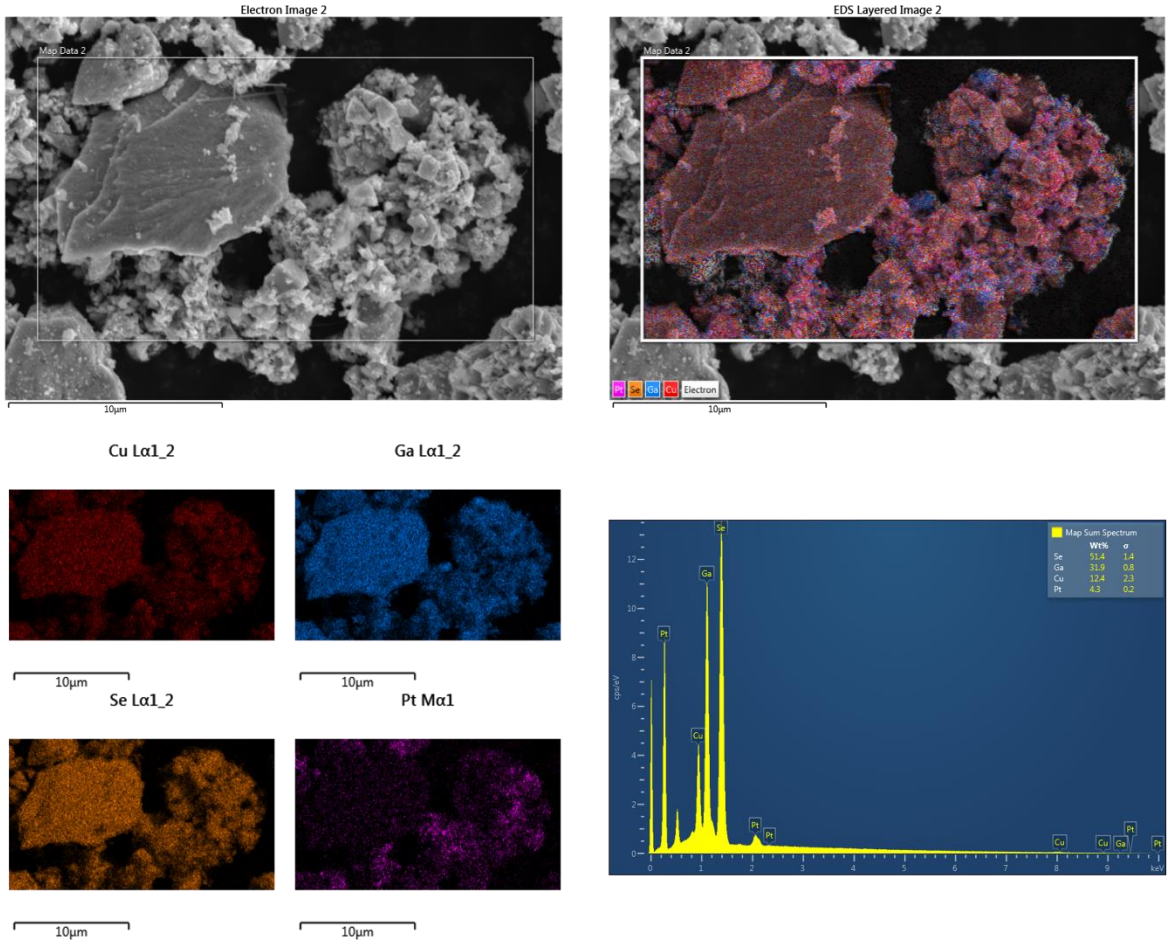

Figure 3.8 SEM and EDX mapping of Pt-loaded $CuGa_3Se_5$ (impregnation method). EDX shows that Pt loading amount is 4.3 wt%.

Next, H_2 evolution test under visible light irradiation was performed on the particle suspensions, with 0.1 M KI as sacrificial electron donor (E^0 (I_3^-/I^-) = 0.536 V_{NHE}). H_2 evolution results are shown in **Figure 3.9a**. The $CuGaSe_2$-Pt shows no H_2 evolution activity. This is possibly attributed to inefficient charge carrier separation in $CuGaSe_2$ as discussed above. The $CuGa_3Se_5$-Pt produces hydrogen at a relative steady rate of 0.4 μmol/h over the 7 h experiment.

It was reported that the photocatalytic H_2 evolution rate of p-type GaP has a dependence on the potential barrier at the solid-liquid junction, which is partially controlled by the potential of the sacrificial electron donor.[40] So as another sacrificial donor 0.1 M Na_2SO_3 (E (SO_4^{2-}/SO_3^{2-}) = -0.516 V_{NHE}, at pH 7) was tested. H_2 was evolved, but at the same H_2 evolution rate as before (**Figure 3.9b**). Overall, the photocatalytic H_2 evolution activity of $CuGa_3Se_5$-Pt remains significantly below its theoretical limit (0.86 $mmol \cdot h^{-1} \cdot cm^{-2}$, assuming a bandgap of 1.7 eV and quantum efficiency of 100%). This suggests the activity is limited not by the proton reduction overpotential, but by electron-hole recombination at surface defects and poor charge separation.

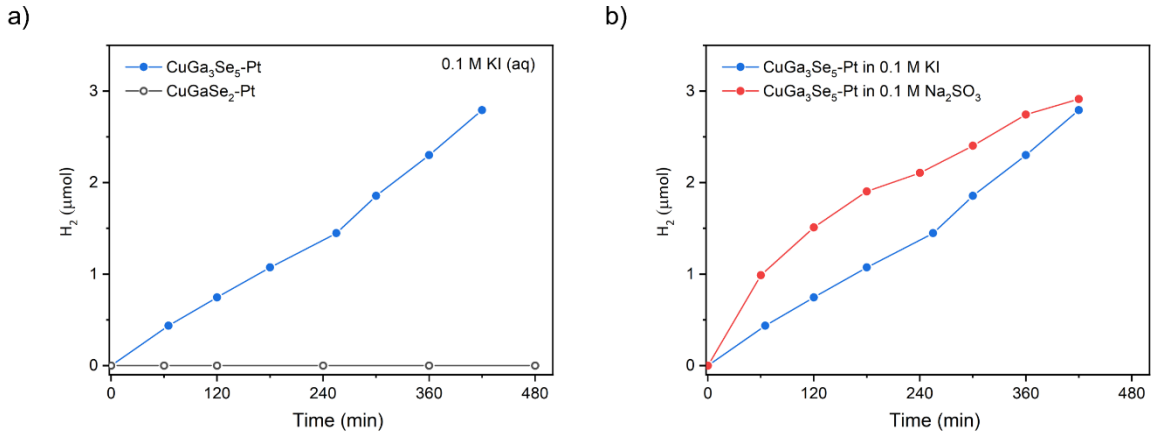

Figure 3.9 Hydrogen evolution from (a) 25 mg $CuGa_3Se_5$-Pt or $CuGa_3Se_5$-Pt particles in 50 mL 0.1 M KI solution, or (b) 25 mg $CuGa_3Se_5$-Pt particles in 50 mL 0.1 M Na_2SO_3 solution under Xe lamp irradiation with 400 nm long pass filter.

Sulfur treatment has been known to passivate III-V semiconductors, by removal of surface defects from native oxides and dangling sulfur bonds.[41-43] To test the effect of sulfur treatment on CGSe, a high temperature solid-state sulfur treatment was applied to $CuGa_3Se_5$. $CuGa_3Se_5$ powders were mixed and ground with sulfur of 1:1 molar ratio and heated at 900 ºC for 10 h in a sealed quartz tube. A PXRD pattern of the resulting powder is shown in **Figure 3.10**. Comparing to $CuGa_3Se_5$, the diffraction peaks of the resulting compound shifted to higher angle by 2 theta = 0.4 degrees, indicating a smaller unit cell size. SEM and EDS mapping result (**Figure 3.11**) shows uniform sulfur distribution and gives atomic ratio of Cu: Ga: Se: S to 9.3: 10.8: 33.5: 46.4, which is close to 1: 1: 3: 4. The above results indicate that 20 atomic percent of Se in $CuGa_3Se_5$ was replaced by S, giving the new quaternary compound $CuGa_3Se_4S$.

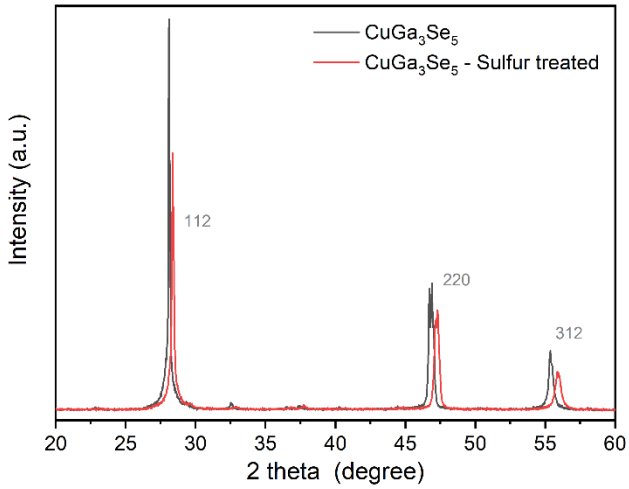

Figure 3.10 XRD pattern of high temperature (900 ºC, 10 h) sulfur treated $CuGa_3Se_5$. The diffraction peaks of the resulting compound shifted to higher angle by 2 theta = 0.4 degrees.

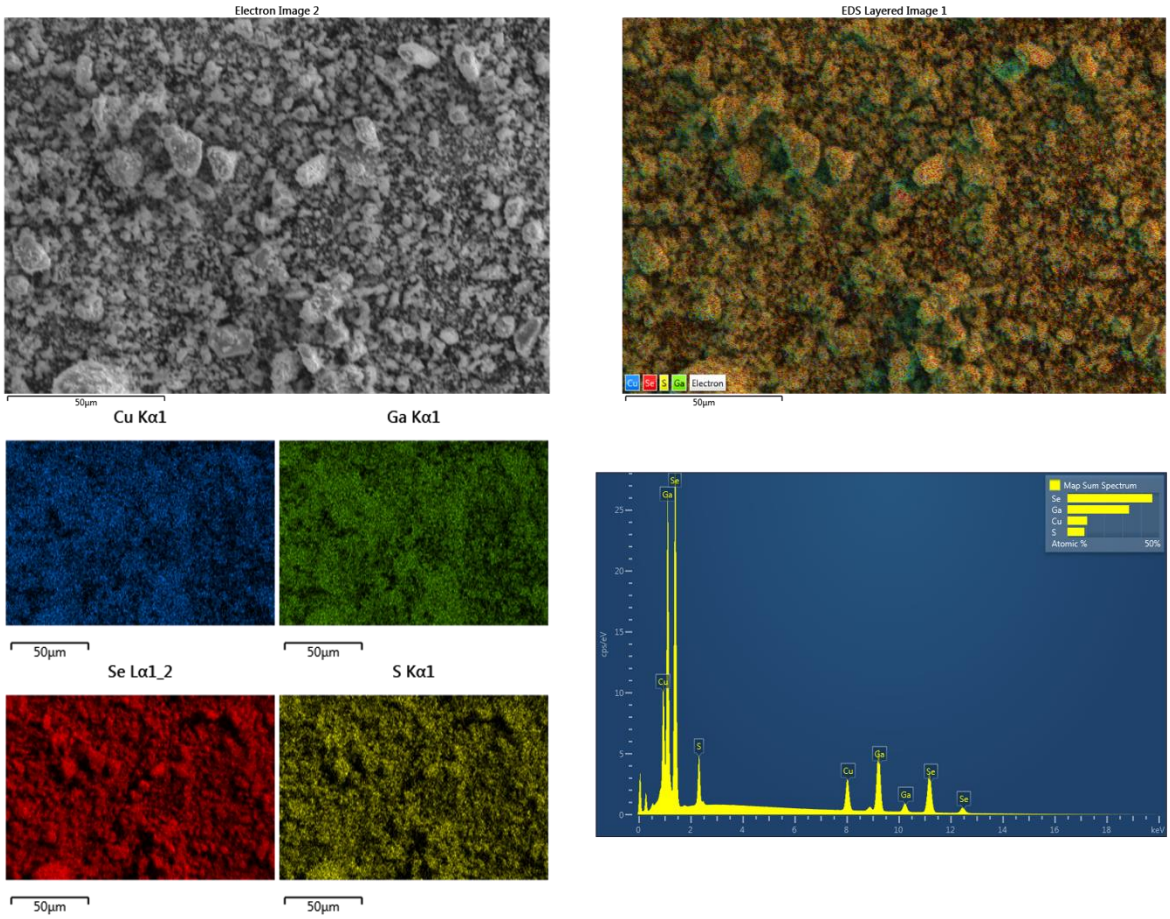

Figure 3.11 SEM and EDX mapping of high temperature sulfur treated $CuGa_3Se_5$. EDX gives the atomic ratio of Cu: Ga: Se: S to be 9.3: 10.8: 33.5: 46.4, which is close to 1: 1: 3: 4.

With S substitution, the $CuGa_3Se_4S$ is expected to have a more reducing conduction band than $CuGa_3Se_5$. To test the effect on the photocatalytic H_2 evolution properties, an illumination experiment was performed on the $CuGa_3Se_4S$ after loading the Pt cocatalyst. The result in **Figure 3.12** shows that there is no significant improvement. This indicates that the low activity of $CuGa_3Se_5$ is not limited by the conduction band edge. This also agrees with the energy scheme in **Figure 3.1**.

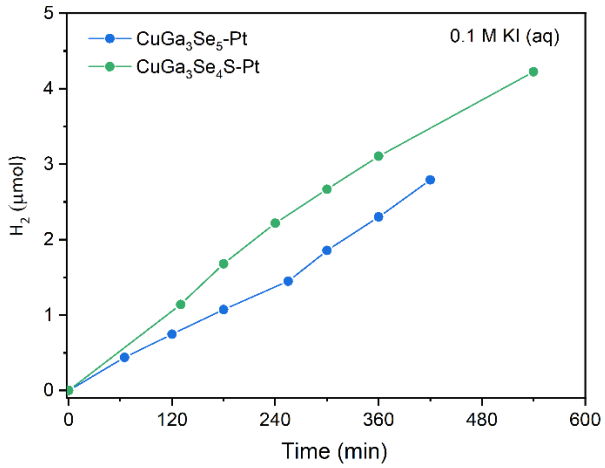

Figure 3.12 Hydrogen evolution from 25 mg $CuGa_3Se_4S$-Pt or $CuGa_3Se_5$-Pt particles in 50 mL 0.1 M KI solution under Xe lamp irradiation with 400 nm long pass filter.

As discussed above, the achieved photocatalytic activity of $CuGa_3Se_5$ is far below the theoretical limit. We attribute this to the high recombination rate and inefficient charge separation under illumination in the CGSe particles. To further investigate the photochemical charge separation in the CGSe particles, additional SPS and transient surface photovoltage (SPV) experiments were conducted for $CuGa_3Se_5$. As discussed earlier, $CuGa_3Se_5$ (blue line in **Figure 3.5)** shows a small photovoltage signal between 1.25 eV and 1.6 eV, which was attributed to the light absorption and charge separation induced by sub-bandgap states and surface states. To further study the charge separation that is caused by these states, we performed full SPV scan with increased photon energy range and increased light intensity at low energy range. This was done by changing the settings of monochromator and holographic grating from grating 2 to grating 1 (details are shown in the Experimental section). The output spectrum from the light source of Xe lamp is shown in **Figure 3.20** in the Appendix.

The revised SPV spectrum of the $CuGa_3Se_5$ particle film on FTO (**FTO-$CuGa_3Se_5$**) is shown in **Figure 3.13a**, alongside its UV-vis absorption spectrum. As shown in the marked region of I and II, there is a substantial SPV signal before the optical bandgap. This is attributed to the light absorption and charge

separation caused by the sub-bandgap states and interface/surface states, as shown in the energy diagram (**Figure 3.14b**). In analogy to Cu(In, Ga)Se_2,[30-31, 34, 44-45] these defects may be assigned to copper vacancy (V_{Cu}) acceptor states 0.1 eV above the valence band and Ga_{Cu} antisite donor states 0.4 eV below the conduction band. Transitions between these states could produce the SPV onset at 1.2 eV in region II. The SPV onset at 0.8 eV in region I indicates additional defect states located at 0.8-0.9 eV above the valence band. These might be defect states at the FTO/$CuGa_3Se_5$ interface.

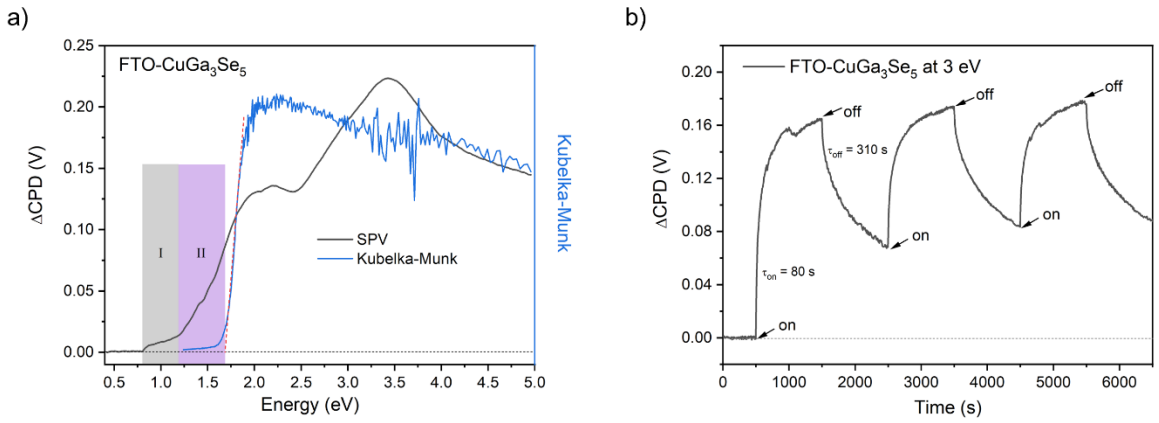

Figure 3.13 (a) SPV spectra of FTO-$CuGa_3Se_5$ and UV-vis spectra. (b) Transient SPV data of FTO-$CuGa_3Se_5$ under 3.0 eV illumination (~1.6 mW·cm^{-2}).

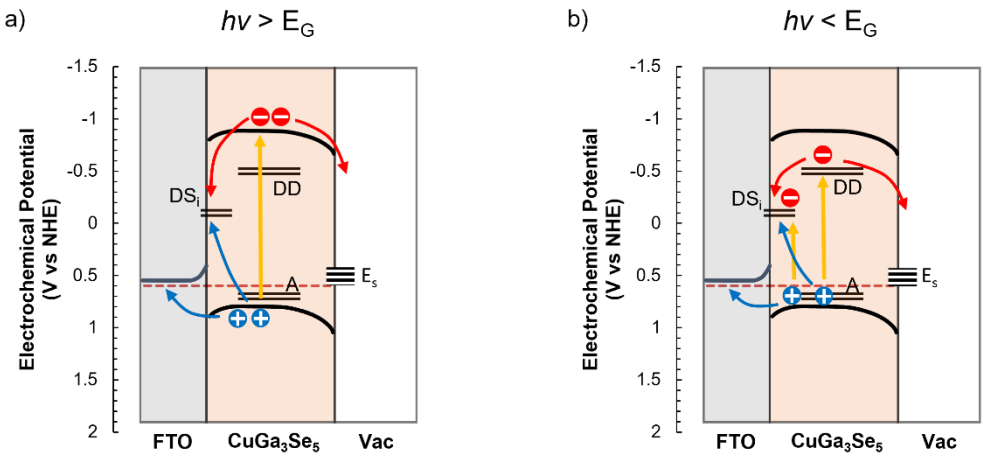

Figure 3.14 Energy diagrams of FTO-$CuGa_3Se_5$ showing charge separation under (a) super-bandgap ($h\nu > E_G$) and (b) sub-bandgap ($h\nu < E_G$) illumination. DD: deep donor states 0.4 eV below the conduction

band (CB). A: shallow acceptor states 0.1 eV above the valence band (VB). DS_i: defect states at the interface. DS_i contribute to the sub-bandgap SPV signal, also act as recombination sites and trap states that limit the charge separation and transfer in FTO-$CuGa_3Se_5$ particle films.

To evaluate the ability of these states to trap charge carriers, transient SPV data was recorded under monochromatic illumination at 3.0 eV, as shown in **Figure 3.13b**. The scan shows a positive SPV signal similar in size and sign to what was seen in the full spectrum. This suggests a similar charge transport mechanism under monochromatic illumination. The signal rise and decay can be described with time constants τ_{on} and τ_{off} which correspond to the times needed for the signal to reach 63.2% (1-1/e) of the final value, after light on and off, respectively.[11] Charge separation in FTO-$CuGa_3Se_5$ occurs on an 80 second time scale, but photovoltage decay is markedly slower with τ_{off} =310 s. This difference is attributed to the different charge transport mechanism, *drift* under light and *diffusion* when the light is off.[40] In the first light-on and light-off circle, there is still 41% of the photovoltage remaining after 1,000 seconds. This indicates that some of the photogenerated electrons were trapped in deep trap states. Similar observations of this low photovoltage reversibility and slow charge transport have been reported in the SPV study of GaP particles films.[40]

We hypothesize that the low photovoltage and slow charge transport of $CuGa_3Se_5$ particles on FTO is a result of charge trapping at the FTO/$CuGa_3Se_5$ interface (**Figure 3.14**). To confirm this, $CuGa_3Se_5$ particle films were prepared on molybdenum or nickel substrate, by drop-casting, and annealing at 600 ^oC in argon for 2h. The SPV spectrum and transient SPV data for the $CuGa_3Se_5$ particle film on molybdenum (**Mo-$CuGa_3Se_5$**) are shown in **Figure 3.15**. The positive photovoltage signal seen in **Figure 3.15a** confirms the hole injection into the molybdenum substrate. Compared to FTO-$CuGa_3Se_5$, the Mo contact gives increased photovoltage in the entire absorption range (1.5 eV – 3.0 eV) and the sub-bandgap photovoltage at 0.8 eV is reduced. Also, the transient SPV data in **Figure 3.15b** reveals much smaller time constants (τ_{on} = 30 s, τ_{off} = 30 s) compared with FTO (τ_{on} = 80 s, τ_{off} = 310 s). This shows that charge transfer for the $CuGa_3Se_5$ particle films on molybdenum substrate is faster than on FTO. In the

first light-on and light-off circle, there is only 13% of the photovoltage remaining after 1,000 seconds (41% for FTO-$CuGa_3Se_5$). This also indicates that there are fewer charge trap states at the Mo/$CuGa_3Se_5$ interface.

These findings are consistent with the results in Chapter 2 for the physical vapor deposited (PVD) $CuGa_3Se_5$ thin films, which prove that a Mo contact promotes hole transfer.[46-47] Based on the diminished SPV signal in 0.8-1.2 eV region the Mo-CGSe interface also has fewer defects. This confirms that the defects 0.8-0.9 eV above valence band originate from the FTO/CGSe interface (**Figure 3.14a** and **Figure 3.15c**).

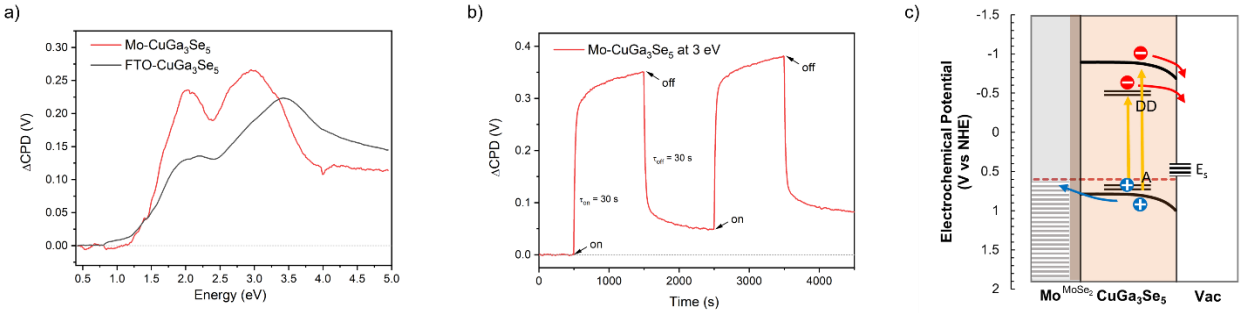

Figure 3.15 (a) SPV spectra of Mo-$CuGa_3Se_5$ and FTO-$CuGa_3Se_5$. (b) Time-dependent SPV data of Mo-$CuGa_3Se_5$ under 3.0 eV illumination (~1.6 mW·cm^{-2}). (c) Energy diagram of Mo-$CuGa_3Se_5$, showing charge separation under illumination. A $MoSe_2$ layer is expected at the Mo-CGSe interface.[46-47]

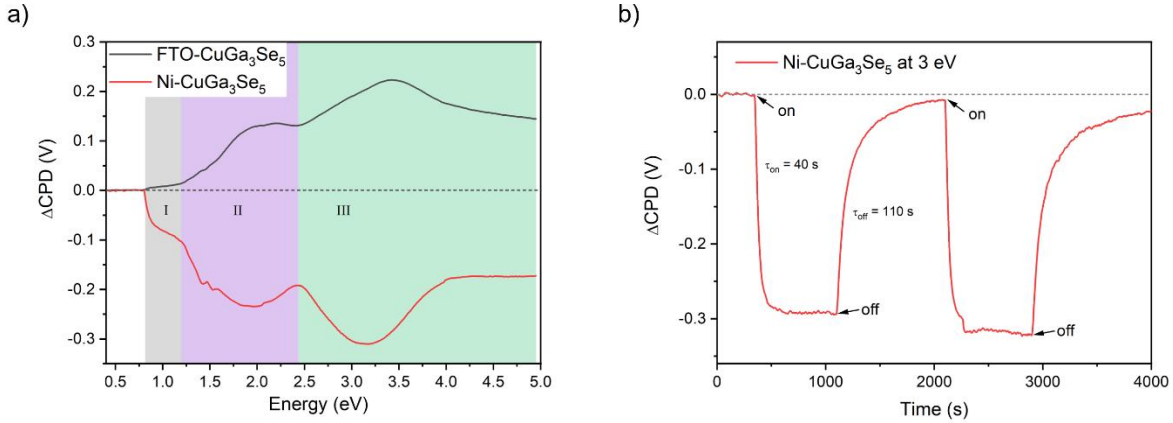

Figure 3.16 (a) SPV spectra of Ni-$CuGa_3Se_5$ and FTO-$CuGa_3Se_5$. (b) Transient SPV data of Ni-$CuGa_3Se_5$ under 3.0 eV illumination (~1.6 mW·cm^{-2}). Regions I, II, III designate 0.8-1.2 eV, 1.2-2.4 eV, and 2.4-4.9 eV, respectively.

SPV spectra and transient SPV data for the $CuGa_3Se_5$ particle film on a nickel substrate (**Ni-$CuGa_3Se_5$**) are shown in **Figure 3.16**. Surprisingly, a negative photovoltage signal was observed, which indicates electron injection into the nickel substrate (**Figure 3.17b**). The spectrum of Ni-$CuGa_3Se_5$ also shows an enhanced SPV signal (-0.30 V at 3.0 eV), compared to FTO-$CuGa_3Se_5$ (0.19 V at 3.0 eV). Additionally, the time dependent SPV data under band gap illumination in **Figure 3.16b** shows small time constants (τ_{on} = 40 s, τ_{off} = 110 s) and good reversibility. This indicates that nickel acts as a reversible electron selective contact for $CuGa_3Se_5$. The electron selectivity is possibly due to the formation of a thin nickel selenide (e.g., p-type NiSe [48]) layer at the Ni/$CuGa_3Se_5$ interface during the thermal annealing at 600 ºC. Related to that, nickel sulfide hydroxide composite (NiS/$Ni(OH)_2$) formed on ZnSe:CGSe photocatalyst has been reported to be a good hydrogen evolution cocatalyst that facilitates the electron transfer.[26] Therefore we believe that the nickel selenide interlayer is likely responsible for the observed selective electron transfer in the Ni-$CuGa_3Se_5$ film.

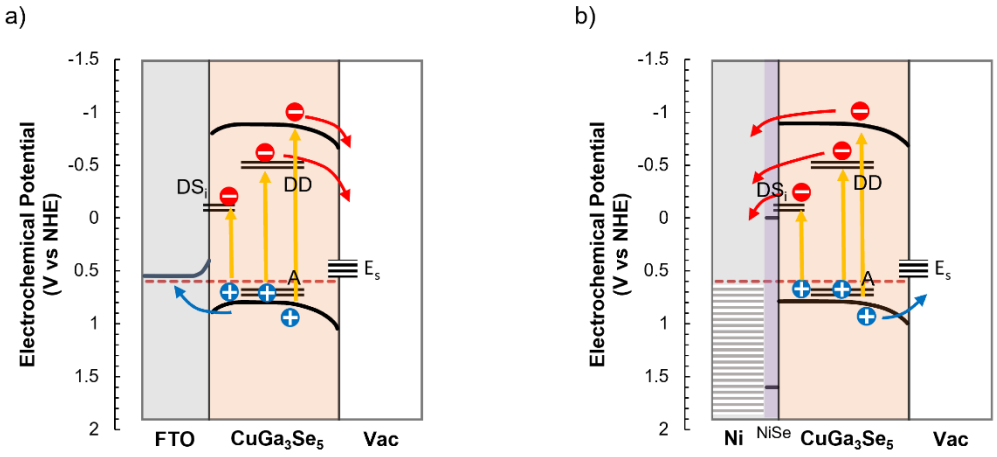

Figure 3.17 Energy diagrams of (a) FTO-$CuGa_3Se_5$ and (b) Ni-$CuGa_3Se_5$ showing charge separation under illumination (including both super-bandgap and sub-bandgap illumination). Nickel substrate acts as

an electron selective contact for $CuGa_3Se_5$, possibly due to the formation of a thin NiSe interlayer during thermal annealing.

Lastly, we investigate TiO_2 as electron selective contact for CGSe. TiO_2 is widely used as electron transporting layer in solar cells.[49-50] To apply this in the CGSe particle films, a TiO_2 particle layer was first prepared by drop-casting 3 mg/mL P25 TiO_2 aqueous suspensions on FTO, followed by 2h annealing at 500 ^oC in air, resulting FTO-TiO_2. And then $CuGa_3Se_5$ particles were drop-cast on the top of TiO_2 layer, followed by annealing at 500 ^oC in argon for 2 h. The formed film is denoted as FTO-TiO_2-$CuGa_3Se_5$. SPV spectra of FTO-TiO_2 and FTO-TiO_2-$CuGa_3Se_5$ are shown in **Figure 3.18** together with charge transfer diagrams. The negative photovoltage observed for FTO-TiO_2 is assigned to the photogenerated electrons injection into the FTO substrate. This confirms the n-type property of TiO_2. The SPV signal shows at 2.1 eV onset is assigned to the charge separation caused by Ti(III) states,[51] while the sharp increase near 3 eV is due to the bandgap absorption. For FTO-TiO_2-$CuGa_3Se_5$, the negative photovoltage at 1.2-3.5 eV confirms the electron injection into the substrate. While the photovoltage features shown in regions II and IV are due to the light absorption and charge separation caused by TiO_2 layer, those features shown in regions I and III are assigned to the $CuGa_3Se_5$ layer. Comparing to FTO-$CuGa_3Se_5$, the inverted photovoltage confirms that TiO_2 acts as electron selective layer, as shown in **Figure 3.18b**. This is explained by the formation a p-n junction at the $CuGa_3Se_5$/TiO_2 interface and by the low valence band of TiO_2 blocking the photoholes from CGSe. The increased photovoltage at 1.2 eV further confirms presence of defect states in $CuGa_3Se_5$.

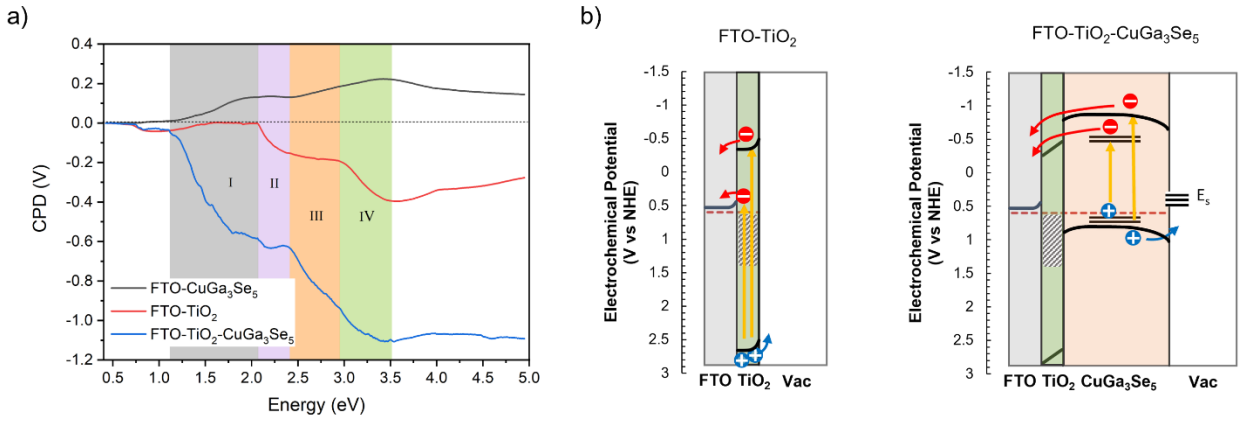

Figure 3.18 (a) SPV spectra of FTO-$CuGa_3Se_5$, FTO-TiO_2 and FTO-TiO_2-$CuGa_3Se_5$. (b) Energy diagrams of FTO-TiO_2 and FTO-TiO_2-$CuGa_3Se_5$, showing charge separation under illumination. Band positions of TiO_2 are estimated from literature value.[51-53] The shaded region in the TiO_2 band diagram indicates a Ti^{3+}-defect band.[51]

Conclusions

$CuGaSe_2$ and $CuGa_3Se_5$ powders were synthesized via solid-state reaction method. XRD, SEM, and UV-vis spectra confirmed their crystal structure, morphology, and optical properties. The optical band gap was found to be 1.55 eV for $CuGaSe_2$ and 1.70 eV for $CuGa_3Se_5$. Photoelectrochemical measurements on drop casted $CuGaSe_2$ and $CuGa_3Se_5$ particle films on FTO showed weak cathodic photocurrents (10 $\mu A \cdot cm^{-2}$ and 20 $\mu A \cdot cm^{-2}$ at -0.2 V_{RHE}) in 0.1 M Na_2SO_4 electrolyte for water reduction. These currents were limited by poor charge separation, electron-hole recombination, and a proton reduction overpotential. After Pt cocatalyst loading, a $CuGa_3Se_5$ particle suspension was mildly active (0.4 $\mu mol \cdot h^{-1}$ over the 7 h experiment) for H_2 evolution from aqueous solution with KI or Na_2SO_3 as the sacrificial donor. The low activity can be attributed to poor charge separation and electron-hole recombination. Surface photovoltage spectroscopy (SPS) on $CuGa_3Se_5$ particle films on FTO revealed strong sub-bandgap signals at 0.8 eV and 1.2 eV, that were attributed to interface/surface defects, likely

V_{Cu} and Ga_{Cu}, based on the literature. These defects can act as charge recombination sites and may be responsible for the low H_2 evolution activity. The SPS result showed that molybdenum is a good hole-selective contact for CGSe, and that nickel or TiO_2 function as electron-selective contacts for CGSe. Adding these contacts to CGSe particles may lead to improved photocatalysts. However, testing this hypothesis requires methods for uniform particle coating with these materials. Such methods should be developed in future work.

Experimental Section

Chemicals. Copper (I) selenide (99.95%, Sigma-Aldrich) and gallium (III) selenide (99.99%, Fisher Scientific) were used for the synthesis of CGSe. Cadmium acetate dihydrate (analytical reagent, Mallinckrodt), thiourea (99%, Alfa Aesar) and ammonium hydroxide (29.7%, certified ACS plus, Fisher Chemicals) were used for the cadmium sulfide chemical bath deposition. Sodium sulfate (≥99.0%, Sigma-Aldrich), sodium sulfite (98.0%, Sigma-Aldrich), potassium iodide (99.9%, Fisher Scientific), dihydrogen hexachloroplatinate (IV) (99.9%, Alfa Aesar), sulfur (99+%, Strem Chemicals) and titanium (IV) oxide (Aeroxide P25, 99.8 %, Acros Organics) were used as received.

Solid-state synthesis of CGSe Powders: CGSe powders were prepared by the published solid-state reaction method.[21] The precursor materials, Cu_2Se (99.95%) and Ga_2Se_3 (99.99%), were ground in a mortar for 20 minutes and then mixed in the inert atmosphere in a nitrogen gas-filled glove box. In the mixing process, the ratio of the precursors was changed to achieve molar ratios of Ga/Cu of 1 and 3. For example, Ga/Cu=1: Cu_2Se 0.1772 g, Ga_2Se_3 0.3235 g; Ga/Cu=3: Cu_2Se 0.0782 g, Ga_2Se_3 0.4243 g were used. These powder mixtures were sealed in quartz tubes, then heated up to 900 ^oC in 10 h, followed by calcination at 900 ^oC for 10 h. Sample were then cooled to room temperature in 10 h. This resulted in a polycrystalline chunk of CGSe. Quartz tubes were opened in air and the CGSe powders were then

obtained by the grinding of the chunk for 10 min. Yields vary from 85% to 95 % for different batches. The loss of yield mostly comes from transferring samples.

Characterizations of CGSe Powders: Powder X-ray diffraction measurements were performed using a Bruker D8 Advance Eco with a Cu Kα X-ray radiation and a monochromatic wavelength of 1.5418 Å. The UV−visible diffuse reflectance spectrum was recorded using a Thermo Scientific Evolution 220 spectrometer, equipped with an integrating sphere. The instrument was calibrated using a $BaSO_4$ disk as a reference. Scanning electron microscopy (SEM) and energy dispersive X-ray spectroscopy (EDX) data were recorded using Scios DualBeam FIB/SEM.

CGSe particle films used in SPV and PEC measurements were prepared by first drop-casting 0.6 mL aqueous suspension (ca. 3 mg/mL) on the corresponding substrate with an area of 0.385 cm^2, followed by drying in air and further annealing at 500 ^oC or 600 ^oC in argon for 2 h.

Surface photovoltage spectroscopy (SPS): Data was obtained under vacuum (~10^{-5} mbar) with a Delta Phi Besocke Kelvin Control and Kelvin probe system. Samples were mounted inside of a custom-made vacuum chamber approximately 1.0 mm underneath the vibrating gold Kelvin probe and illuminated with light from a 150 W Xe lamp passing through an Oriel Cornerstone 130 monochromator. Spectra in **Figure 3.5** were measured using holographic grating 2 (1200 l/mm, 250 nm Blaze, 180-650 nm) from 1.2-5.0 eV. All others were measured using holographic grating 1 (1800 l/mm, 500 nm Blaze, 300-1070 nm) from 0.4-5.0 eV. Emission spectra for these two gratings are shown in **Figure 3.20** in the Appendix.

Photoelectrochemical Linear Sweep Voltammetry (LSV) Measurements: Electrochemical measurements were conducted using a Gamry Reference 600 Potentiostat connected to a typical three-electrode system, with a Pt counter electrode and a calomel reference electrode (3.5 M KCl). All PEC measurements were performed in an open round bottom flask after purging N_2 for 20 minutes. There is no purging during the scans. LSV scans were performed with a 10 mV/s scan rate in cathodic direction. The potentials in each measurement were converted to normal hydrogen electrode (NHE) by calibration with

10 mM $K_3Fe(CN)_6$/ $K_4Fe(CN)_6$ (E^0=0.358 V_{NHE}). Potentials were adjusted to RHE with the following formula: $V_{RHE} = V_{NHE} + 0.0592 \times pH$. A 300 W Xe lamp with a 0.22 M $NaNO_2$ (aq) 400 nm long pass filter was used as the light source.

Photocatalytic hydrogen evolution tests: These were performed by dispersing 25 mg of the catalysts in 50 mL aqueous solution with sacrificial agent (0.1 M KI: 0.830 g of KI; 0.1 M Na_2SO_3: 0.630 g of Na_2SO_3) in a 135 mL quartz flask. The flask was evacuated down to 50 torr and purged with argon several times to remove the air. The stirred suspension was irradiated with a 300 W xenon arc lamp with a 0.22 M $NaNO_2$(aq) 400 nm long pass filter (visible light intensity of 400 $mW \cdot cm^2$ at the flask as measured by a SEL005 detector connected to an International Light IL1400BL photometer). A cooling fan was attached to the flask to keep the temperature at 25-30 ^oC. The air-tight irradiation system was connected to a Varian 3800 gas chromatograph (with a 60/80 Å molecular sieve column and thermal conductivity detector) to quantify the gases evolved.

Surface Modification with CdS: CdS layers were formed on the surface of the CGSe films by chemical bath deposition.[9] An aqueous solution containing cadmium acetate, thiourea, and ammonium hydroxide with concentrations of 25 mM, 375 mM, and 14 wt %, respectively, was used as a chemical bath (0.170 g cadmium acetate dihydrate, 0.860 g thiourea, 15 mL 28 wt% ammonium hydroxide and 15 mL water). This bath solution was heated to 70 ^oC with stirring. The CGSe films were immersed in the chemical bath for 60 s. After this treatment, the resulting films were rinsed with water followed by post-annealing in air at 200 ^oC for 1 h.

Pt deposition on CGSe via impregnation method: 100 mg CGSe and 5 mL water containing 5.3 mg H_2PtCl_6 (2.5 mg Pt, 2.5 wt% Pt) were placed in an open glass vial and heated to 90 ^oC in a water bath with occasionally stirring until all water in the vial evaporated. The resulting powder was heated at 450 ^oC under argon for 3 h to produce CGSe-Pt in 95% yield.

Appendix

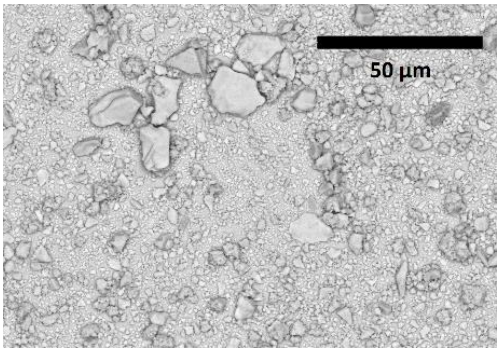

Figure 3.19 SEM image of drop-cast $CuGa_3Se_5$ film on FTO. It shows un-uniform covering with large particles and exposed FTO surface.

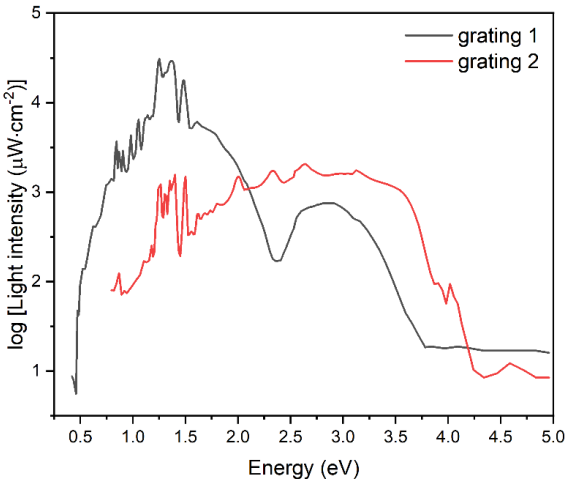

Figure 3.20 Spectra of the 150 W Xe lamp passing through the monochromator with different holographic grating settings, as measured with a thermopile at the SPV measurement distance. Grating 1 gives higher light intensity at low photo energy range (0.7 eV – 2.0 eV).

References

1. Osterloh, F. E., Inorganic Materials as Catalysts for Photochemical Splitting of Water. *Chemistry of Materials* **2008,** *20* (1), 35-54.

2. Kudo, A.; Miseki, Y., Heterogeneous photocatalyst materials for water splitting. *Chemical Society Reviews* **2009,** *38* (1), 253-278.

3. Fabian, D. M.; Hu, S.; Singh, N.; Houle, F. A.; Hisatomi, T.; Domen, K.; Osterloh, F. E.; Ardo, S., Particle suspension reactors and materials for solar-driven water splitting. *Energy Environ Sci* **2015,** *8* (10), 2825-2850.

4. Osterloh, F. E., Photocatalysis versus Photosynthesis: A Sensitivity Analysis of Devices for Solar Energy Conversion and Chemical Transformations. *ACS Energy Letters* **2017,** *2* (2), 445-453.

5. Chen, S.; Takata, T.; Domen, K., Particulate photocatalysts for overall water splitting. *Nature Reviews Materials* **2017,** *2* (10), 17050.

6. Takata, T.; Domen, K., Particulate Photocatalysts for Water Splitting: Recent Advances and Future Prospects. *ACS Energy Letters* **2019,** *4* (2), 542-549.

7. Yanagi, R.; Zhao, T.; Solanki, D.; Pan, Z.; Hu, S., Charge Separation in Photocatalysts: Mechanisms, Physical Parameters, and Design Principles. *ACS Energy Letters* **2022,** *7* (1), 432-452.

8. Kudo, A., Z-scheme photocatalyst systems for water splitting under visible light irradiation. *MRS Bulletin* **2011,** *36* (1), 32-38.

9. Maeda, K., Z-Scheme Water Splitting Using Two Different Semiconductor Photocatalysts. *ACS Catalysis* **2013,** *3* (7), 1486-1503.

10. Zhou, P.; Yu, J.; Jaroniec, M., All-Solid-State Z-Scheme Photocatalytic Systems. *Advanced Materials* **2014,** *26* (29), 4920-4935.

11. Melo, M. A.; Wu, Z.; Nail, B. A.; De Denko, A. T.; Nogueira, A. F.; Osterloh, F. E., Surface Photovoltage Measurements on a Particle Tandem Photocatalyst for Overall Water Splitting. *Nano Letters* **2018,** *18* (2), 805-810.

12. Wang, Q.; Hisatomi, T.; Jia, Q.; Tokudome, H.; Zhong, M.; Wang, C.; Pan, Z.; Takata, T.; Nakabayashi, M.; Shibata, N.; Li, Y.; Sharp, I. D.; Kudo, A.; Yamada, T.; Domen, K., Scalable water splitting on particulate photocatalyst sheets with a solar-to-hydrogen energy conversion efficiency exceeding 1. *Nat Mater* **2016,** *15* (6), 611-5.

13. Niki, S.; Contreras, M.; Repins, I.; Powalla, M.; Kushiya, K.; Ishizuka, S.; Matsubara, K., CIGS absorbers and processes. *Progress in Photovoltaics: Research and Applications* **2010,** *18* (6), 453-466.

14. Guillemoles, J.-F.; Kronik, L.; Cahen, D.; Rau, U.; Jasenek, A.; Schock, H.-W., Stability Issues of Cu(In,Ga)Se_2-Based Solar Cells. *The Journal of Physical Chemistry B* **2000,** *104* (20), 4849-4862.

15. Chen, Y.; Feng, X.; Liu, M.; Su, J.; Shen, S., Towards efficient solar-to-hydrogen conversion: Fundamentals and recent progress in copper-based chalcogenide photocathodes. *Nanophotonics* **2016,** *5* (4), 524-547.

16. Kobayashi, H.; Sato, N.; Orita, M.; Kuang, Y.; Kaneko, H.; Minegishi, T.; Yamada, T.; Domen, K., Development of highly efficient $CuIn_{0.5}Ga_{0.5}Se_2$-based photocathode and application to overall solar driven water splitting. *Energy & Environmental Science* **2018,** *11* (10), 3003-3009.

17. Gaillard, N.; Prasher, D.; Chong, M.; Deangelis, A.; Horsley, K.; Ishii, H. A.; Bradley, J. P.; Varley, J.; Ogitsu, T., Wide-Bandgap Cu(In,Ga)S_2 Photocathodes Integrated on Transparent Conductive F:SnO_2 Substrates for Chalcopyrite-Based Water Splitting Tandem Devices. *ACS Applied Energy Materials* **2019,** *2* (8), 5515-5524.

18. Marsen, B.; Cole, B.; Miller, E. L., Photoelectrolysis of water using thin copper gallium diselenide electrodes. *Solar Energy Materials and Solar Cells* **2008,** *92* (9), 1054-1058.

19. Kim, J.; Minegishi, T.; Kobota, J.; Domen, K., Investigation of Cu-Deficient Copper Gallium Selenide Thin Film as a Photocathode for Photoelectrochemical Water Splitting. *Japanese Journal of Applied Physics* **2011,** *51* (1), 015802.

20. Moriya, M.; Minegishi, T.; Kumagai, H.; Katayama, M.; Kubota, J.; Domen, K., Stable hydrogen evolution from CdS-modified $CuGaSe_2$ photoelectrode under visible-light irradiation. *Journal of the American Chemical Society* **2013,** *135* (10), 3733-3735.

21. Kumagai, H.; Minegishi, T.; Moriya, Y.; Kubota, J.; Domen, K., Photoelectrochemical Hydrogen Evolution from Water Using Copper Gallium Selenide Electrodes Prepared by a Particle Transfer Method. *The Journal of Physical Chemistry C* **2014,** *118* (30), 16386-16392.

22. Muzzillo, C. P.; Klein, W. E.; Li, Z.; DeAngelis, A. D.; Horsley, K.; Zhu, K.; Gaillard, N., Low-Cost, Efficient, and Durable H2 Production by Photoelectrochemical Water Splitting with $CuGa_3Se_5$ Photocathodes. *ACS Applied Materials & Interfaces* **2018,** *10* (23), 19573-19579.

23. Mahmoudi, B.; Caddeo, F.; Lindenberg, T.; Schneider, T.; Hölscher, T.; Scheer, R.; Maijenburg, A. W., Photoelectrochemical properties of Cu-Ga-Se photocathodes with compositions ranging from $CuGaSe_2$ to $CuGa_3Se_5$. *Electrochimica Acta* **2021,** *367*, 137183.

24. Chen, S.; Ma, G.; Wang, Q.; Sun, S.; Hisatomi, T.; Higashi, T.; Wang, Z.; Nakabayashi, M.; Shibata, N.; Pan, Z.; Hayashi, T.; Minegishi, T.; Takata, T.; Domen, K., Metal selenide photocatalysts for visible-light-driven Z-scheme pure water splitting. *Journal of Materials Chemistry A* **2019,** *7* (13), 7415-7422.

25. Chen, S.; Hisatomi, T.; Ma, G.; Wang, Z.; Pan, Z.; Takata, T.; Domen, K., Metal selenides for photocatalytic Z-scheme pure water splitting mediated by reduced graphene oxide. *Chinese Journal of Catalysis* **2019,** *40* (11), 1668-1672.

26. Chen, S.; Vequizo, J. J. M.; Hisatomi, T.; Nakabayashi, M.; Lin, L.; Wang, Z.; Yamakata, A.; Shibata, N.; Takata, T.; Yamada, T.; Domen, K., Efficient photocatalytic hydrogen evolution on single-crystalline metal selenide particles with suitable cocatalysts. *Chemical Science* **2020,** *11* (25), 6436-6441.

27. Wasim, S. M.; Rincón, C.; Delgado, J. M.; Marín, G., Effect of donor–acceptor defect pairs on the crystal structure of In and Ga rich ternary compounds of Cu–In(Ga)–Se(Te) systems. *Journal of Physics and Chemistry of Solids* **2005,** *66* (11), 1990-1993.

28. Stojilovic, N., Using Cu Kα1/Kα2 Splitting and a Powder XRD System To Discuss X-ray Generation. *Journal of Chemical Education* **2018,** *95* (4), 598-600.

29. Tuttle, J.; Albin, D.; Goral, J.; Kennedy, C.; Noufi, R., Effects of composition and substrate temperature on the electro-optical properties of thin-film $CuInSe_2$ and $CuGaSe_2$. *Solar Cells* **1988,** *24* (1), 67-79.

30. Igalson, M.; Czudek, A., Electrical spectroscopy methods for the characterization of defects in thin-film compound solar cells. *Journal of Applied Physics* **2022,** *131* (24), 240901.

31. Spindler, C.; Babbe, F.; Wolter, M. H.; Ehré, F.; Santhosh, K.; Hilgert, P.; Werner, F.; Siebentritt, S., Electronic defects in Cu(In, Ga)Se_2: Towards a comprehensive model. *Physical Review Materials* **2019,** *3* (9), 090302.

32. Meeder, A.; Fuertes Marrón, D.; Chu, V.; Conde, J. P.; Jäger-Waldau, A.; Rumberg, A.; Lux-Steiner, M. C., Photoluminescence and sub band gap absorption of $CuGaSe_2$ thin films. *Thin Solid Films* **2002,** *403-404*, 495-499.

33. Krysztopa, A.; Igalson, M.; Larsen, J. K.; Aida, Y.; Gütay, L.; Siebentritt, S., Photoinduced current transient spectroscopy of defect levels in $CuInSe_2$ and $CuGaSe_2$ epitaxial and polycrystalline layers. *Journal of Physics D: Applied Physics* **2012,** *45* (33), 335101.

34. Spindler, C.; Regesch, D.; Siebentritt, S., Revisiting radiative deep-level transitions in $CuGaSe_2$ by photoluminescence. *Applied Physics Letters* **2016,** *109* (3), 032105.

35. Gaillard, N. *Wide Band Gap Chalcopyrite Photoelectrodes for Direct Water Splitting*; Univ. of Hawaii, Honolulu, HI (United States): 2019.

36. Pohl, J.; Albe, K., Intrinsic point defects in $CuInSe_2$ and $CuGaSe_2$ as seen via screened-exchange hybrid density functional theory. *Physical Review B* **2013,** *87* (24), 245203.

37. Anantharaj, S.; Amarnath, T. S.; Subhashini, E.; Chatterjee, S.; Swaathini, K. C.; Karthick, K.; Kundu, S., Shrinking the Hydrogen Overpotential of Cu by 1 V and Imparting Ultralow Charge Transfer Resistance for Enhanced H_2 Evolution. *ACS Catalysis* **2018,** *8* (7), 5686-5697.

38. Zhang, W.; Fu, D.; Bai, Y.; Yuan, C., In-situ anion exchange synthesis of copper selenide electrode as electrocatalyst for hydrogen evolution reaction. *International Journal of Hydrogen Energy* **2017,** *42* (16), 10925-10930.

39. Tan, S. M.; Chua, C. K.; Sedmidubský, D.; Sofer, Z.; Pumera, M., Electrochemistry of layered GaSe and GeS: applications to ORR, OER and HER. *Physical Chemistry Chemical Physics* **2016,** *18* (3), 1699-1711.

40. Zhao, Z.; Willard, E. J.; Dominguez, J. R.; Wu, Z.; Osterloh, F. E., Depletion layer controls photocatalytic hydrogen evolution with p-type gallium phosphide particles. *Journal of Materials Chemistry A* **2019,** *7* (30), 18020-18029.

41. Driad, R.; Lu, Z. H.; Charbonneau, S.; McKinnon, W. R.; Laframboise, S.; Poole, P. J.; McAlister, S. P., Passivation of InGaAs surfaces and InGaAs/InP heterojunction bipolar transistors by sulfur treatment. *Applied Physics Letters* **1998,** *73* (5), 665-667.

42. Iyer, R.; Chang, R. R.; Lile, D. L., Sulfur as a surface passivation for InP. *Applied Physics Letters* **1988,** *53* (2), 134-136.

43. Suyatin, D. B.; Thelander, C.; Bjork, M. T.; Maximov, I.; Samuelson, L., Sulfur passivation for ohmic contact formation to InAs nanowires. *Nanotechnology* **2007,** *18* (10).

44. Bauknecht, A.; Siebentritt, S.; Albert, J.; Lux-Steiner, M. C., Radiative recombination via intrinsic defects in $Cu_xGa_ySe_2$. *Journal of Applied Physics* **2001,** *89* (8), 4391-4400.

45. Krysztopa, A.; Igalson, M.; Larsen, J. K.; Aida, Y.; Gutay, L.; Siebientritt, S., Photoinduced current transient spectroscopy of defect levels in $CuInSe_2$ and $CuGaSe_2$ epitaxial and polycrystalline layers. *Journal of Physics D-Applied Physics* **2012,** *45* (33).

46. Kohara, N.; Nishiwaki, S.; Hashimoto, Y.; Negami, T.; Wada, T., Electrical properties of the Cu(In,Ga)Se_2/$MoSe_2$/Mo structure. *Solar Energy Materials and Solar Cells* **2001,** *67* (1), 209-215.

47. Abou-Ras, D.; Kostorz, G.; Bremaud, D.; Kalin, M.; Kurdesau, F. V.; Tiwari, A. N.; Dobeli, M., Formation and characterisation of $MoSe_2$ for Cu(In,Ga)Se_2 based solar cells. *Thin Solid Films* **2005,** *480*, 433-438.

48. Hankare, P. P.; Jadhav, B. V.; Garadkar, K. M.; Chate, P. A.; Mulla, I. S.; Delekar, S. D., Synthesis and characterization of nickel selenide thin films deposited by chemical method. *Journal of Alloys and Compounds* **2010,** *490* (1), 228-231.

49. Choi, J.; Song, S.; Horantner, M. T.; Snaith, H. J.; Park, T., Well-Defined Nanostructured, Single Crystalline TiO_2 Electron Transport Layer for Efficient Planar Perovskite Solar Cells. *Acs Nano* **2016,** *10* (6), 6029-6036.

50. Tavakoli, M. M.; Yadav, P.; Tavakoli, R.; Kong, J., Surface Engineering of TiO2 ETL for Highly Efficient and Hysteresis-Less Planar Perovskite Solar Cell (21.4%) with Enhanced Open-Circuit Voltage and Stability. *Advanced Energy Materials* **2018,** *8* (23).

51. Gomathi Devi, L.; Mohan Reddy, K., Photocatalytic performance of silver TiO_2: Role of electronic energy levels. *Applied Surface Science* **2011,** *257* (15), 6821-6828.

52. Giannakopoulou, T.; Papailias, I.; Todorova, N.; Boukos, N.; Liu, Y.; Yu, J.; Trapalis, C., Tailoring the energy band gap and edges' potentials of g-C_3N_4/TiO_2 composite photocatalysts for NOx removal. *Chemical Engineering Journal* **2017,** *310*, 571-580.

53. Wang, K.; Wei, Z.; Colbeau-Justin, C.; Nitta, A.; Kowalska, E., P25 and its components - Electronic properties and photocatalytic activities. *Surfaces and Interfaces* **2022,** *31*, 102057.

Chapter 4 Surface Photovoltage Spectroscopy and Photoelectrochemical Studies on Metavanadates (CuV_2O_6, ZnV_2O_6 and $Zn_4V_2O_9$) and Calcium Ferrite ($CaFe_2O_4$)

The surface photovoltage spectroscopy (SPS) and photoelectrochemical (PEC) studies on the metavanadates (CuV_2O_6, ZnV_2O_6 and $Zn_4V_2O_9$) are parts of the published work[1-2] in collaboration with Prof. Julia Zaikina's group from Iowa State University. Selected parts of the publications are reproduced from reference 1 and 2 with permission by American Chemical Society.

Introduction

Transition metal oxides are receiving increasing interest for the application of PEC water splitting, because of their low cost, chemical stability, and favorable band edge positions.[3-8] While having been extensively studied, simple metal oxides (TiO_2, WO_3, and α-Fe_2O_3) are still not efficiently used, limited by their wide band gaps, poor charge separation and mobility, and slow water oxidation kinetics.[9-11] Incorporation of secondary metal cations into the lattice of simple metal oxides may bring a solution to those limitations. For example, the ternary metal oxide $BiVO_4$, with the bandgap of 2.55 eV, was demonstrated with promising PEC water oxidation performance (2.73 mA/cm^2 at 0.6 V_{RHE}).[12]

Similarly, other metal vanadates, like manganese vanadate (β-$Mn_2V_2O_7$)[13] and copper vanadates (CuV_2O_6, β-$Cu_2V_2O_7$, γ-$Cu_3V_2O_8$, $Cu_{11}V_6O_{26}$, and $Cu_5V_2O_{10}$)[14-20] are considered suitable for PEC applications as well. Copper vanadates possess bandgap energies around 2.0 eV and are chemically stable under mild alkaline conditions.[14] However, the demonstrated PEC performance are not efficient. For example, the copper-poor CuV_2O_6 shows the most drastic increase of photocurrent density (0.30-0.75 mA·cm^{-2}) beyond 1.23 V vs RHE for water oxidation.[16, 18, 20] In contrast, the zinc based analogue ZnV_2O_6 is underexplored, although it was predicted with a favorable bandgap of 2.31 eV and suitable band edge position for water oxidation in a computational study.[21]

Recently, a collaboration between the Zaikina and Osterloh (Dr. Rachel Doughty) groups revealed that oxygen deficiencies, can be introduced in zinc and copper pyrovanadates $M_2V_2O_7$ (M = Zn

and Cu) via a deep eutectic solvent (DES) synthesis route.[22] These vacancies play a vital role for optical absorption and transport properties of metal oxides.[23-26] The Zaikina group then went on to demonstrate that the DES synthetic method can be extended to metavanadates MV_2O_6 (M = Zn and Cu) and zinc-rich $Zn_4V_2O_9$ containing oxygen vacancies. The effective bandgap, majority charge carrier type and charge separation ability of MV_2O_6 (M = Zn and Cu) were characterized by Rachel Doughty with surface photovoltage spectroscopy (SPS).[1] This chapter describes the results of an SPS study on the zinc-rich $Zn_4V_2O_9$, and on their photoelectrochemical methanol or/and water oxidation experiments. Additionally, the surface photovoltage properties of $CaFe_2O_4$ are presented. This oxide is an example of the ferrite family MFe_2O_4 ($M = Ca^{2+}$, Co^{2+}, Cu^{2+}, Mg^{2+} etc.), which exhibit bandgaps of around 2 eV and are made of only elements that are inexpensive and readily available.[27-28] That makes them promising candidates as water oxidation photoanodes. Among them, $CaFe_2O_4$ stands out because the reported conduction band potential is located more cathodic than the hydrogen reduction potential, making $CaFe_2O_4$ a candidate for photocatalytic hydrogen evolution.[29-31] Recently, the Marschall group reported a phase-pure and highly crystalline $CaFe_2O_4$ with a sponge-like microporous structure that was synthesized via facile solution-based microwave reaction and subsequent short thermal treatment.[32] The surface photovoltage spectra reveal the effective bandgap of the material, its majority charge carrier type, and the presence of two separate space charge region (SCR) in the particle films.

Results and Discussion

Powders of the metavanadates (CuV_2O_6, ZnV_2O_6 and $Zn_4V_2O_9$) were received from Prof. Julia Zaikina's group from Iowa State University. Synthesis and structure analysis were done by the Zaikina group. Details are described in the publications.[1-2] Powder X-ray diffraction (PXRD), scanning electron microscopy (SEM), UV-vis, and X-ray photoelectron spectroscopy (XPS) data of the metavanadates are shown in **Figure 4.5** in the Appendix. PXRD patterns confirm the materials to be phase-pure monoclinic CuV_2O_6, ZnV_2O_6 and $Zn_4V_2O_9$. A broad range of individual particles sizes (4−22 μm) with a few

agglomerates for both ZnV_2O_6 and CuV_2O_6 are identified with SEM. The particles have irregular shapes with sharp and round edges. The SEM image of $Zn_4V_2O_9$ shows agglomerates sized up to ~27 μm with porous morphology. The optical bandgaps of the materials are found at 1.8 eV (CuV_2O_6), 2.2 eV (ZnV_2O_6) and 2.9 eV ($Zn_4V_2O_9$). XPS data shows the existence of reduced vanadium species (V^{4+}) in the ZnV_2O_6 and increased concentrations in the zinc-rich $Zn_4V_2O_9$.

Particle films of the metavanadates were prepared on fluorine-doped tin oxide (FTO) coated glass substrates by drop-casting from aqueous suspensions (ca. 3 mg/mL), followed by air annealing at 500 ºC for 2h. The film electrodes (**Figure 4.6** in the Appendix) were used in the following SPS and PEC studies.

First, we use SPS to study the photophysics of $Zn_4V_2O_9$ (**Figure** 4.1). The negative photovoltage is attributed to the injection of photogenerated electrons in $Zn_4V_2O_9$ into the FTO substrate, as shown in the inset. It confirms that the material is n-type. The tangent line for the major photovoltage feature gives a 2.95 eV effective bandgap, which is similar to the optical band gap of the material (**Figure 4.5d** in the Appendix). This is relative larger than the bandgap of the zinc-poor ZnV_2O_6 (2.3 eV). However, there is also substantial sub-bandgap photovoltage signal at 2.25–2.95 eV observed, suggesting the presence of defect states. These states likely correspond to lattice V^{4+} ions that are also responsible for the visible absorption tail in the optical spectra, and that were detected in XPS data for the material (**Figure 4.5e** in the Appendix). The sub-bandgap signal is much more pronounced than for ZnV_2O_6 (**Figure 4.7a** in the Appendix) or $Zn_2V_2O_7$,[22] which indicates that $Zn_4V_2O_9$ has a higher V^{4+} concentration. This is consistent with the XPS data.

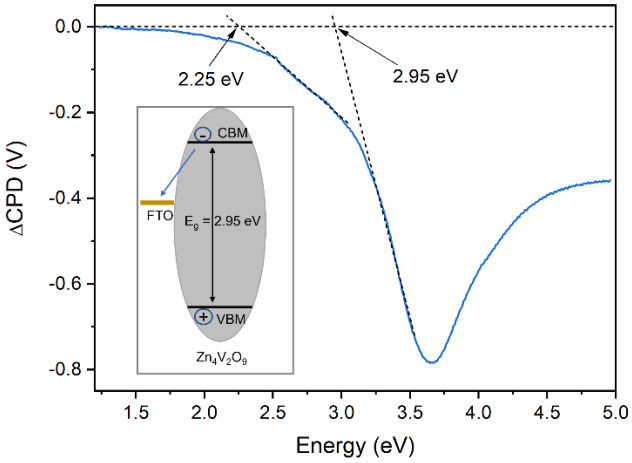

Figure 4.1 SPS of a $Zn_4V_2O_9$ particle film on FTO. Inset: charge transfer causing the photovoltage signal. Adapted with permission from reference 2. Copyright 2022, American Chemical Society.

Next, photoelectrochemical methanol or/and water oxidation experiments were conducted on the metavanadates (CuV_2O_6, ZnV_2O_6 and $Zn_4V_2O_9$) particle film electrodes to investigate these materials for potential solar energy conversion applications. Linear sweep voltammetry (LSV) curves of ZnV_2O_6 and CuV_2O_6 are recorded under chopped light illumination, in degassed aqueous 0.1 M Na_2SO_4 with 20% (v:v) added methanol (**Figure 4.2**). Anodic photocurrents of over 0.40 mA·cm^{-2} for CuV_2O_6 and over 0.150 mA·cm^{-2} for ZnV_2O_6 can be attributed to the oxidation of methanol. For both materials, the initial photocurrent begins at 0.6 V vs NHE, which approximates the electron quasi-Fermi level under illumination. This value compares reasonably well with calculated conduction band edges at the point of zero charge (0.71 V vs NHE for CuV_2O_6 and 0.49 V vs NHE for ZnV_2O_6) using the Butler–Ginley method (details in the Experimental Section).[33-34] The much faster rising photocurrent for CuV_2O_6 suggests that its photoelectrochemical properties are superior to those of ZnV_2O_6. This is mostly attributed to the better light harvesting properties resulting from the smaller band gap of the material. Additionally, we speculate that the lower photocurrent response of ZnV_2O_6 is limited by the higher V^{4+} content, as revealed by the XPS data (**Figure 4.5e** in the Appendix). Reduced metal ions, from oxygen vacancies, for example, are known to produce mid-band gap states that cause electron hole

recombination and lead to energy loss.[35-36] On the basis of the photocurrent size and onset potentials, the vanadates appear to perform at a similar level as recently reported Bi, Zn, Mg, and Cu ferrites ($BiFeO_3$ and MFe_2O_4; M = Zn, Mg, Cu)[28, 37-40] and also Mo-doped $FeVO_4$.[41]

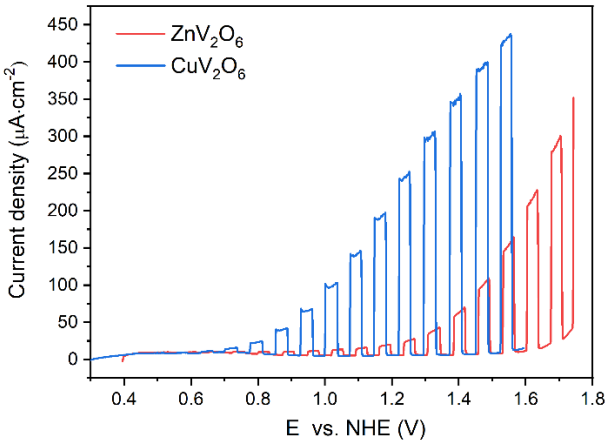

Figure 4.2 Photoelectrochemical scans of ZnV_2O_6 and CuV_2O_6 on FTO with intermitted illumination from the Xe lamp with a 400 nm long pass filter (visible light intensity 150 mW·cm^{-2}). The electrolyte is degassed aqueous 0.1 M Na_2SO_4 (pH 7) containing 20% (v/v) methanol. Adapted with permission from reference 1. Copyright 2021, American Chemical Society.

To determine if the zinc-rich vanadate $Zn_4V_2O_9$ is able to facilitate photoelectrochemical reactions, LSV curves under chopped simulated sunlight were obtained on $Zn_4V_2O_9$ particle film electrodes in degassed aqueous 0.1 M Na_2SO_4 with 20% (v:v) added methanol or in aqueous 0.1 M K_2SO_4 (**Figure 4.3**). Weak photocurrents were observed when the applied potentials exceeded +0.15 V vs NHE in aqueous methanol and +0.6 V vs NHE in aqueous 0.1 M K_2SO_4. In the latter electrolyte, the current is attributed to water oxidation, although no O_2 could be detected at this low activity. Based on the photo-onset potential in aqueous methanol, the Fermi level in $Zn_4V_2O_9$ is at +0.15 V vs NHE (0.56 V RHE). Overall, $Zn_4V_2O_9$ is 10 times less photoactive than the ZnV_2O_6 phase for which methanol oxidation photocurrents of 20 μA·cm^{-2} at 1.6 V vs RHE were measured under 150 mW·cm^{-2} visible light illumination (**Figure 4.2**). The lower activity of $Zn_4V_2O_9$ is attributed to the high concentration of

V^{4+} sub-band gap states, which promotes recombination with the photogenerated holes. A similar role of reduced Ti^{3+} sites had been observed previously for $SrTiO_3$,[36] and for Fe^{2+} states in hematite.[42]

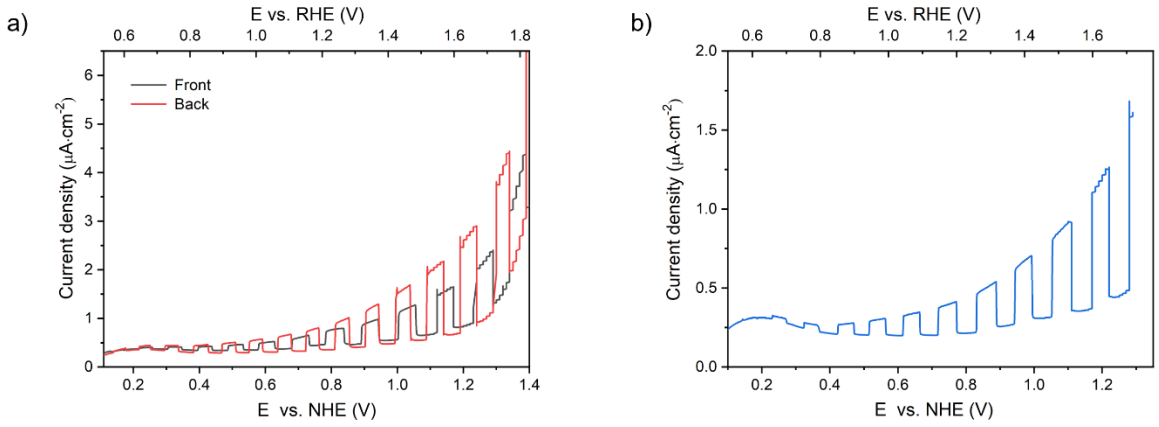

Figure 4.3 Photoelectrochemical scans of $Zn_4V_2O_9$ on FTO with intermitted illumination from a Xe lamp (100 mW·cm^{-2}). The electrolytes are (a) degassed aqueous 0.1 M Na_2SO_4 (pH 7) containing 20% (v/v) methanol or (b) 0.1 M K_2SO_4 aqueous solution (pH 7). Adapted with permission from reference 2. Copyright 2022, American Chemical Society.

Next, the photophysical properties of the calcium ferrite ($CaFe_2O_4$) were investigated. Powders of the $CaFe_2O_4$ were received from Prof. Roland Marschall's group from University of Bayreuth, Germany. Details of the synthesis method and characterization are described in their previous publication,[32] while the PXRD, SEM and UV-vis data of the $CaFe_2O_4$ are shown in **Figure 4.9** in the Appendix. PXRD patterns show the $CaFe_2O_4$ to be phase-pure orthorhombic (Pnma) crystals, with an average crystallite size of 49nm (determined via Scherrer equation). SEM shows that it exhibits a sponge-like, porous macrostructure with walls that are several hundred nanometers in diameter. An indirect optical bandgap of 1.92 eV was determined by Tauc plot construction (**Figure 4.9c**).

Particle films of $CaFe_2O_4$ were prepared on FTO substrates by drop-casting, followed by air annealing at 500 ºC for 2h. The film thickness ranges from 2 μm to 11 μm. Photos of the films and SEM images of the representative films are shown in **Figure 4.8** in the Appendix.

To study the charge separation properties of the $CaFe_2O_4$, SPS measurements of the samples were performed as a function of the film thickness (**Figure 4.4a**). A positive surface photovoltage (SPV) signal is observed for thick films and negative SPV signal is observed for thin films. This reversal of the SPV signal to film thickness is similar to what Rachel Doughty et al. observed recently in the particle films of n-$SrTiO_3$, n-$SrTiO_3$:Al, and n-GaAs:Te.[43] It was attributed to a change from the majority carrier to the minority carrier transport towards the substrate/particle interface. For the $CaFe_2O_4$ particle films, change in the carrier transport indicates the presence of two separate space charge region (SCR) at the substrate/particle interface and at the particle-surface. SCR is known to present at the interface between a semiconductor and an adjacent phase, where the majority carriers is depleted as a result of the electrochemical potential difference.[44-45] This leads to the band bending of the semiconductor at the interface, where the internal electric field can affect the charge carrier transport under illumination.[43]

A model of the charge transport is shown in **Figure 4.4b** for thick and thin films. In the thin film, charge transport is controlled by the space charge layer at the FTO/$CaFe_2O_4$ interface. Electrons are attracted by the interface and holes are repelled by it, producing the negative SPV signal that is observed. In the thick film, light only reaches the film surface, and the charge transport is controlled by the space charge layer at the $CaFe_2O_4$ particle surface. Photogenerated electrons move towards the surface, thus giving the positive SPV signal. The light penetration depth (δ_p), the depth at which the intensity of the light decays to 1/e of its surface value, is calculated based on an absorption coefficient (α) of 1×10^4 cm^{-1} for $CaFe_2O_4$ (under 2.5 eV illumination)[46] : $\delta_p = \alpha^{-1} = 1$ μm. However, for particle films that are not very dense, the light can penetrate deeper. So, for the $CaFe_2O_4$ particle films (**Figure 4.8** in the Appendix) in this study, we estimate that light can penetrate $5\delta_p = 5$ μm deep into the films.

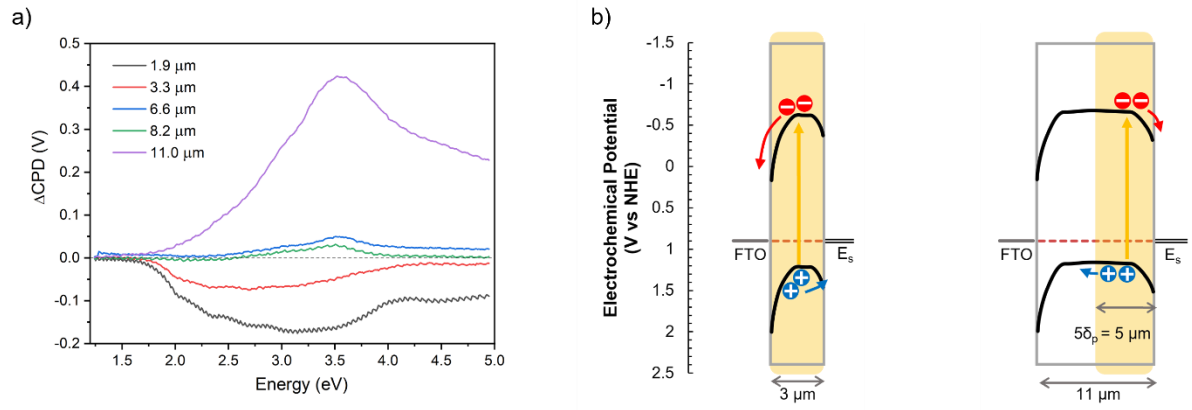

Figure 4.4 (a) SPS of $CaFe_2O_4$ particle films on FTO, with different film thickness. (b) Energy diagram shows the charge separation of the $CaFe_2O_4$ particle films on FTO under illumination. δ_p: light penetration depth. In the thin film, photogenerated charge separation is controlled by the space charge layer at the FTO/$CaFe_2O_4$ interface. In the thick film, light only reaches the film surface, and photogenerated charge separation is controlled by the space charge layer at the $CaFe_2O_4$ particle surface.

On the basis, the major photovoltage signal for the 11.0 µm thick film (purple line in **Figure 4.4a**) can be assigned to transfer of excited electrons into surface states (**Figure 4.4b**). This confirms that electrons are the minority carriers and that is $CaFe_2O_4$ p-type, consistent with the reported Mott-Schottky results on this sample.[32] Based on extrapolation of the tangent of the major photovoltage signal, the effective bandgap can be estimated as 1.75 eV, which is smaller than the optical bandgap of 1.92 eV (**Figure 4.9** in the Appendix). This could be attributed to the existence of sub-bandgap states, possibly Fe^{2+} states, like Fe^{2+} in the hematite.[42] Above 3.6 eV, the photovoltage is diminished because of the low penetration depth of high energy photons and the lower intensity of the Xe lamp at this photon energy.

For samples with thickness of 3.3 µm and 1.9 µm, the photovoltage is inverted from positive to negative. The inversion suggests that carrier movement under illumination is controlled by the SCR at the FTO interface as shown in **Figure 4.4b**. To be noted, the observation of SCR in the particle films usually requires annealing process to enhance the electrical contact the semiconductor/substrate interface.[43]

For 6.6 -8.2 μm thick films, charge separation is controlled by both the interface SCR and the surface SCR, and the photovoltage is reduced. The SCR width at the substrate/particle interface is best estimated from the film thickness which produces the greatest inverted photovoltage.[43] Here it is estimated to be around or less than 1.9 μm for the FTO/$CaFe_2O_4$ interface.

Furthermore, based on this SCR model, the surface states energy can be estimated from the maximum SPV signal of the thick films. The model assumes that surface states of energy E_s control the Fermi energy of the free particles and the band bending in the dark (**Figure 4.4b**). Sufficiently strong illumination flattens the bands at the surface. Thus, the maximum SPV for thick films can be used to estimate the built-in potential (V_{bi}), i.e., the difference of E_s and Fermi level in the bulk (E_F): SPV_{max} (thick film) = $V_{bi} = E_F - E_s$. Using an SPV value of 0.42 V (purple line at 3.5 eV in **Figure 4.4a**), and a Fermi level of 1.43 V_{RHE} for p-$CaFe_2O_4$,[32] the energy of the surface states E_S is estimated as $E_s = E_F - V_{bi}$ = 1.43 V_{RHE} – 0.42 V = 1.01 V_{RHE}. This places the estimated defect states 0.5-0.6 eV above the valence band, as shown in **Figure 4.4.b**. This energy is close to the standard reduction potential of the O_2/H_2O couple (E^0=1.23 V), and thus the defect states are likely associated with adsorbed oxygen.[47-48]

Conclusions

In summary, we used surface photovoltage spectroscopy (SPS) to study the charge separation of $Zn_4V_2O_9$ under illumination. It confirms this vanadate as an n-type semiconductor with effective bandgaps of 2.95 eV. This is similar to CuV_2O_6, ZnV_2O_6 with bandgaps of 1.9 eV, 2.3 eV, as measured previously in this lab.[1] SPS of $Zn_4V_2O_9$ reveals a sub-bandgap photovoltage signal at 2.25–2.95 eV, suggesting the presence of defects, likely V^{4+} lattice ions that were also seen in optical spectra and XPS data. This pronounced sub-band gap signal in $Zn_4V_2O_9$ indicates a higher V^{4+} concentration in $Zn_4V_2O_9$ than in ZnV_2O_6 or $Zn_2V_2O_7$. Photoelectrochemical measurements on CuV_2O_6 and ZnV_2O_6 particle film electrodes show anodic photocurrents (0.40 mA·cm^{-2} for CuV_2O_6, 0.15 mA·cm^{-2} for

ZnV_2O_6, at 1.5 V_{NHE}) for methanol oxidation under visible light illumination. On this basis, $Zn_4V_2O_9$ is approximately 10 times less photoactive (2 $\mu A \cdot cm^{-2}$ at 1.3 V_{NHE}, 100 $mW \cdot cm^{-2}$ visible light) than the ZnV_2O_6 phase (20 $\mu A \cdot cm^{-2}$ at 1.3 V_{NHE}, 150 $mW \cdot cm^{-2}$ visible light) for methanol oxidation under visible light illumination. The lower activity of $Zn_4V_2O_9$ is attributed to the high concentration of V^{4+} sub-band gap states, which promote electron-hole recombination. Also, SPS data on $CaFe_2O_4$ shows the effective bandgap of 1.75 eV, smaller that the optical bandgap of 1.92 eV. We speculate that Fe^{2+} defects are responsible for the observed sub bandgap signal in SPS. Two separate space charge region (SCR) in the particle films of $CaFe_2O_4$ were observed for the first time. For thin films, charge transport is controlled by the SCR at the FTO/$CaFe_2O_4$ interface, estimated to be less than 1.9 mm thick. For thick films, it is controlled by the SCR at the $CaFe_2O_4$ particle surface instead. These results on the metavanadates and $CaFe_2O_4$ impact our understanding of photochemical charge separation in the metal oxide semiconductors and give new insights into optimizing their solar energy conversion applications.

Experimental Section

Chemicals. Sodium sulfate (≥99.0%, Sigma-Aldrich), methanol (≥99.8%, Sigma-Aldrich), potassium ferricyanide (99.2%, Sigma) and potassium hexacyanoferrate (II) trihydrate (98.0% - 102.0%, Sigma-Aldrich) were used as received. Water was purified to 18 MΩ·cm resistivity by a Nanopure system.

Photoelectrochemical (PEC) Measurements: Electrochemical measurements were conducted using a Gamry Reference 600 Potentiostat connected to a typical three-electrode system, with a Pt counter electrode and a calomel reference electrode (3.5 M KCl). All PEC measurements were performed in an open round bottom flask after purging N_2 for 10 minutes. There is no purging during the scans. The potentials in each measurement were converted to normal hydrogen electrode (NHE) by calibration with 10 mM $K_3Fe(CN)_6$/ $K_4Fe(CN)_6$ (E^0 = 0.358 V_{NHE}). Potentials were adjusted to RHE with the following

formula: $V_{RHE} = V_{NHE} + 0.0592 \times pH$. A 300 W Xe lamp with or without a 0.22 M $NaNO_2$ (aq) 400 nm long pass filter was used as the light source. The light intensities at the samples were 100 $mW \cdot cm^{-2}$ for $Zn_4V_2O_9$ (**Figure 4.3**) and 150 $mW \cdot cm^{-2}$ for ZnV_2O_6 and CuV_2O_6 (**Figure 4.2**).

Film electrodes of CuV_2O_6, ZnV_2O_6 and $Zn_4V_2O_9$ were fabricated by drop-casting 0.06 mL of aqueous suspensions (ca. 3 mg/mL) of each material onto fluorine-doped tin oxide (FTO) glasses (0.385 cm^{-2}), followed by drying in air, and annealing at 500 °C in air for 2 h.

Surface Photovoltage Spectroscopy (SPS): Contact potential differences (CPD) were measured under vacuum (~10^{-5} mbar) with a Delta Phi Besocke Kelvin Control and Kelvin probe system. Samples were mounted inside of a custom-made vacuum chamber approximately 1.0 mm underneath the vibrating gold Kelvin probe and illuminated with light from a 150 W Xe lamp passing through an Oriel Cornerstone 130 monochromator. Spectra were acquired by stepping the photon energy by 0.0124 eV every 5 s and by measuring the CPD value at each step. All CPD values are reported relative to the CPD value in the dark, as ΔCPD in SPV spectra.

Films of $Zn_4V_2O_9$ and $CaFe_2O_4$ for the SPS measurements (**Figure 4.2** and **Figure 4.5a**) were fabricated by drop-casting 0.06 mL of aqueous suspensions (ca. 3 mg/mL for $Zn_4V_2O_9$, ca. 1, 3 or 6 mg/mL for $CaFe_2O_4$) of each material onto FTO glasses (0.385 cm^{-2}), followed by drying in air, and annealing at 500 °C in air for 2 h. Film thicknesses were measured with a Veeco Dektak 150 profilometer.

Calculation of Conduction Band Minima Using the Butler Ginley Method:[33] Using data from Schoonen et al.,[34] a geometric mean electron affinity of 6.05 eV is estimated for both ZnV_2O_6 and CuV_2O_6. Using the band gaps of 2.23 eV for ZnV_2O_6 and 1.81 eV for CuV_2O_6, this yields conduction band (CB) minima of −4.93 eV (0.49 V vs NHE) for ZnV_2O_6 and −5.15 eV (0.71 V vs NHE) for CuV_2O_6.

Appendix

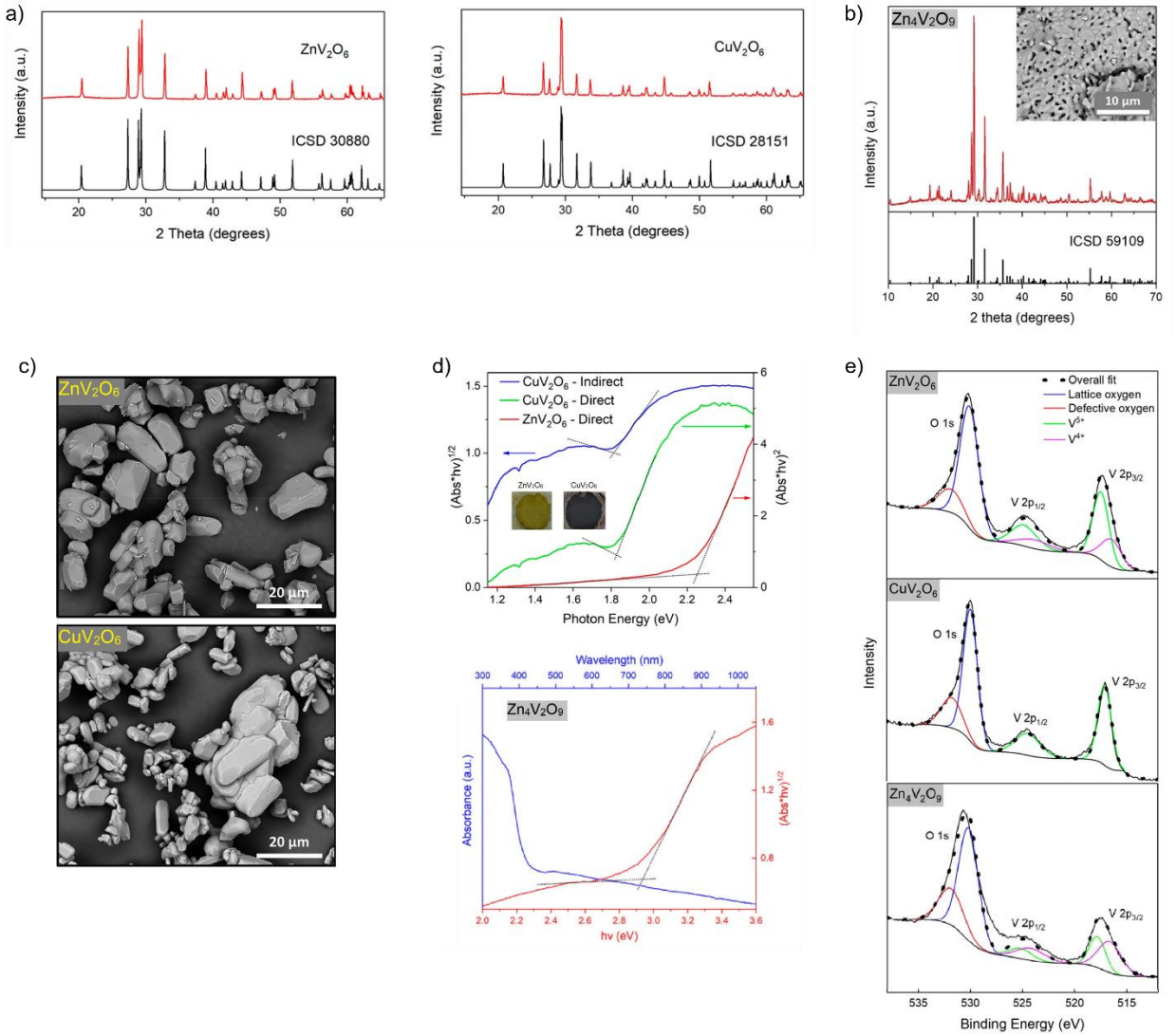

Figure. 4.5 (a) PXRD patterns of ZnV_2O_6 and CuV_2O_6. (b) PXRD pattern and SEM image of $Zn_4V_2O_9$. (c) SEM images of ZnV_2O_6 and CuV_2O_6. (d) Tauc plots (transformed from UV–vis spectra) of ZnV_2O_6, CuV_2O_6 and $Zn_4V_2O_9$. Linear fits (dotted lines) are shown to determine bandgaps. Inset: optical images of ZnV_2O_6 and CuV_2O_6 powders. (e) XPS data of the O 1s and V 2p regions of ZnV_2O_6, CuV_2O_6 and $Zn_4V_2O_9$. Figures are adapted with permission from reference 1 and 2. Copyright 2021 and 2022, American Chemical Society.

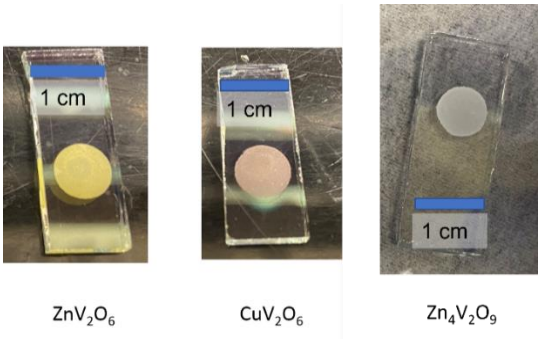

Figure 4.6 Photos of the particle films of CuV_2O_6, ZnV_2O_6 and $Zn_4V_2O_9$ on FTO.

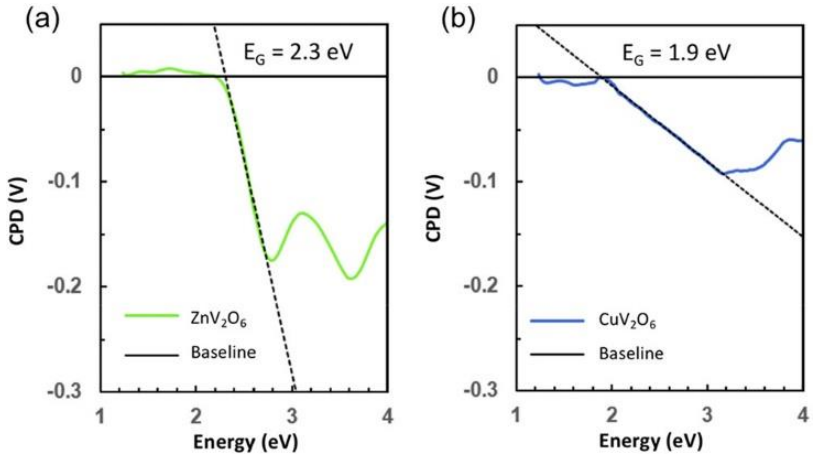

Figure 4.7 SPS data for the vanadate particle films (a, ZnV_2O_6, and b, CuV_2O_6) on gold-coated glass substrates. Adapted with permission from reference 1. Copyright 2021, American Chemical Society.

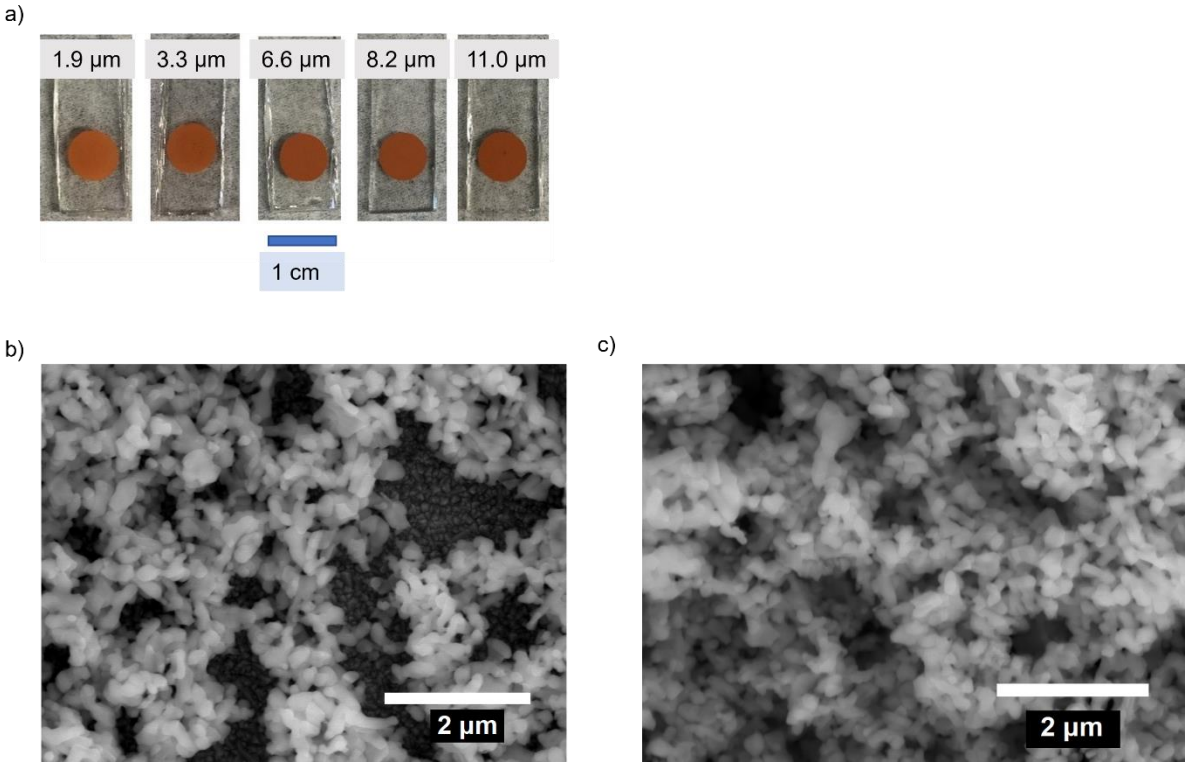

Figure 4.8 (a) Photos of the $CaFe_2O_4$ particle films on FTO. Film thicknesses were measured with a profilometer. (b)(c) SEM image of the 3.3 µm and 11.0 µm thick $CaFe_2O_4$ films, respectively.

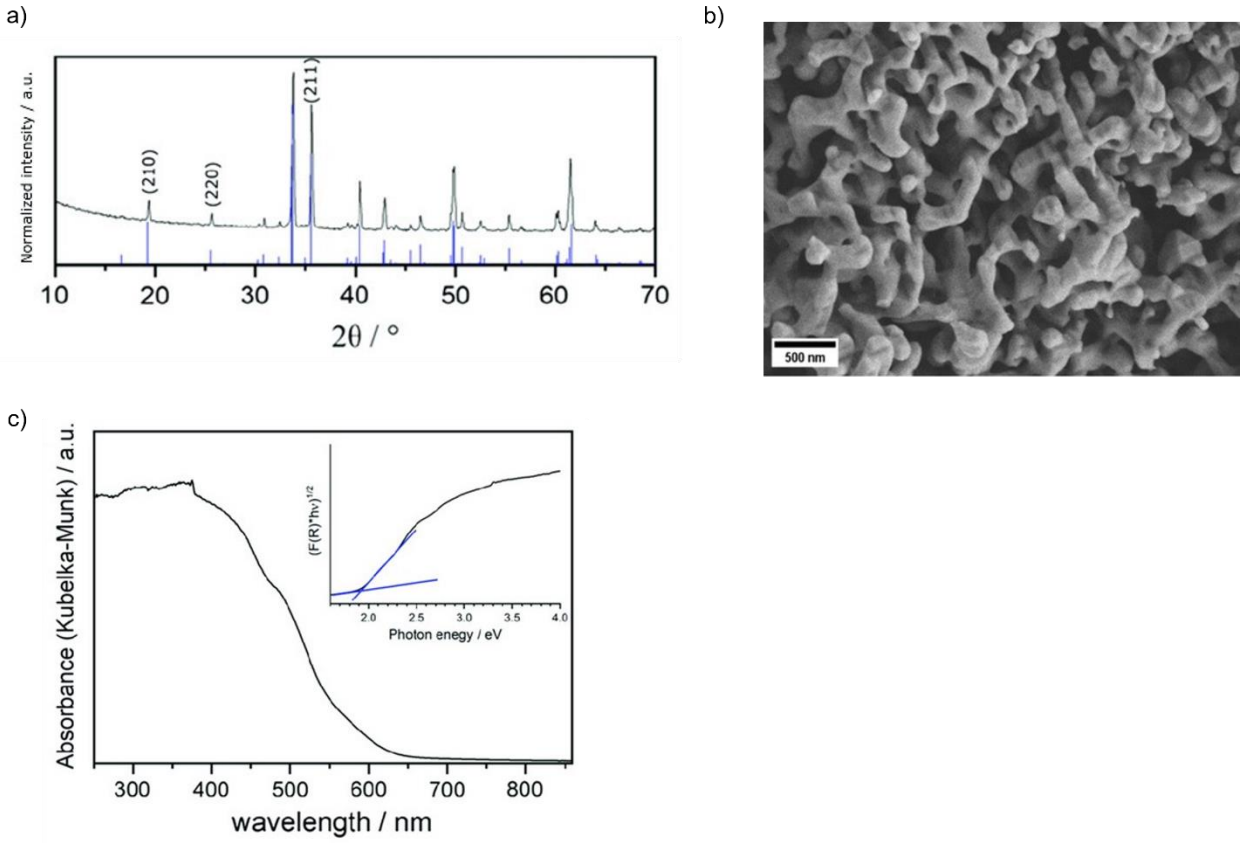

Figure 4.9 (a) PXRD pattern of the synthesized $CaFe_2O_4$. (b) SEM image of the macroporous $CaFe_2O_4$. (c) Kubelka–Munk absorption spectrum of $CaFe_2O_4$. The inset shows the Tauc plot for determination of the indirect optical bandgap of 1.92 eV. Adapted with permission from ref.[32] Copyright 2020 The Authors.

References

1. Hong, S.; Burkhow, S. J.; Doughty, R. M.; Cheng, Y.; Ryan, B. J.; Mantravadi, A.; Roling, L. T.; Panthani, M. G.; Osterloh, F. E.; Smith, E. A.; Zaikina, J. V., Local Structural Disorder in Metavanadates MV_2O_6 (M = Zn and Cu) Synthesized by the Deep Eutectic Solvent Route: Photoactive Oxides with Oxygen Vacancies. *Chemistry of Materials* **2021,** *33* (5), 1667-1682.

2. Hong, S.; Cheng, Y.; Hariyani, S.; Li, J.; Doughty, R. M.; Mantravadi, A.; Adeyemi, A. N.; Smith, E. A.; Brgoch, J.; Osterloh, F. E.; Zaikina, J. V., The Deep Eutectic Solvent Precipitation Synthesis of Metastable $Zn_4V_2O_9$. *Inorganic Chemistry* **2022,** *61* (1), 154-169.

3. Kubacka, A.; Fernández-García, M.; Colón, G., Advanced Nanoarchitectures for Solar Photocatalytic Applications. *Chemical Reviews* **2012,** *112* (3), 1555-1614.

4. Kudo, A.; Miseki, Y., Heterogeneous photocatalyst materials for water splitting. *Chemical Society Reviews* **2009,** *38* (1), 253-278.

5. Hernández-Alonso, M. D.; Fresno, F.; Suárez, S.; Coronado, J. M., Development of alternative photocatalysts to TiO_2: Challenges and opportunities. *Energy & Environmental Science* **2009,** *2* (12), 1231-1257.

6. Kho, Y. K.; Teoh, W. Y.; Iwase, A.; Mädler, L.; Kudo, A.; Amal, R., Flame Preparation of Visible-Light-Responsive $BiVO_4$ Oxygen Evolution Photocatalysts with Subsequent Activation via Aqueous Route. *ACS Applied Materials & Interfaces* **2011,** *3* (6), 1997-2004.

7. Ma, X.; Cui, X.; Zhao, Z.; Melo, M. A.; Roberts, E. J.; Osterloh, F. E., Use of surface photovoltage spectroscopy to probe energy levels and charge carrier dynamics in transition metal (Ni, Cu, Fe, Mn, Rh) doped $SrTiO_3$ photocatalysts for H_2 evolution from water. *Journal of Materials Chemistry A* **2018,** *6* (14), 5774-5781.

8. Boltersdorf, J.; Sullivan, I.; Shelton, T. L.; Wu, Z.; Gray, M.; Zoellner, B.; Osterloh, F. E.; Maggard, P. A., Flux Synthesis, Optical and Photocatalytic Properties of n-type Sn_2TiO_4: Hydrogen and Oxygen Evolution under Visible Light. *Chemistry of Materials* **2016,** *28* (24), 8876-8889.

9. Ni, M.; Leung, M. K. H.; Leung, D. Y. C.; Sumathy, K., A review and recent developments in photocatalytic water-splitting using TiO_2 for hydrogen production. *Renewable and Sustainable Energy Reviews* **2007,** *11* (3), 401-425.

10. Bignozzi, C. A.; Caramori, S.; Cristino, V.; Argazzi, R.; Meda, L.; Tacca, A., Nanostructured photoelectrodes based on WO_3: applications to photooxidation of aqueous electrolytes. *Chemical Society Reviews* **2013,** *42* (6), 2228-2246.

11. Barroso, M.; Pendlebury, S. R.; Cowan, A. J.; Durrant, J. R., Charge carrier trapping, recombination and transfer in hematite (α-Fe_2O_3) water splitting photoanodes. *Chemical Science* **2013,** *4* (7), 2724-2734.

12. Kim Tae, W.; Choi, K.-S., Nanoporous $BiVO_4$ Photoanodes with Dual-Layer Oxygen Evolution Catalysts for Solar Water Splitting. *Science* **2014,** *343* (6174), 990-994.

13. Yan, Q.; Li, G.; Newhouse, P. F.; Yu, J.; Persson, K. A.; Gregoire, J. M.; Neaton, J. B., $Mn_2V_2O_7$: An Earth Abundant Light Absorber for Solar Water Splitting. *Advanced Energy Materials* **2015,** *5* (8), 1401840.

14. Zhou, L.; Yan, Q.; Shinde, A.; Guevarra, D.; Newhouse, P. F.; Becerra-Stasiewicz, N.; Chatman, S. M.; Haber, J. A.; Neaton, J. B.; Gregoire, J. M., High Throughput Discovery of Solar Fuels Photoanodes in the CuO–V_2O_5 System. *Advanced Energy Materials* **2015,** *5* (22), 1500968.

15. Jiang, C.-M.; Segev, G.; Hess, L. H.; Liu, G.; Zaborski, G.; Toma, F. M.; Cooper, J. K.; Sharp, I. D., Composition-Dependent Functionality of Copper Vanadate Photoanodes. *ACS Applied Materials & Interfaces* **2018,** *10* (13), 10627-10633.

16. Guo, W.; Chemelewski, W. D.; Mabayoje, O.; Xiao, P.; Zhang, Y.; Mullins, C. B., Synthesis and Characterization of CuV_2O_6 and $Cu_2V_2O_7$: Two Photoanode Candidates for Photoelectrochemical Water Oxidation. *The Journal of Physical Chemistry C* **2015,** *119* (49), 27220-27227.

17. Khan, I.; Qurashi, A., Shape Controlled Synthesis of Copper Vanadate Platelet Nanostructures, Their Optical Band Edges, and Solar-Driven Water Splitting Properties. *Scientific Reports* **2017,** *7* (1), 14370.

18. Hossain, M. K.; Sotelo, P.; Sarker, H. P.; Galante, M. T.; Kormányos, A.; Longo, C.; Macaluso, R. T.; Huda, M. N.; Janáky, C.; Rajeshwar, K., Rapid One-Pot Synthesis and Photoelectrochemical Properties of Copper Vanadates. *ACS Applied Energy Materials* **2019,** *2* (4), 2837-2847.

19. Jiang, C.-M.; Farmand, M.; Wu, C. H.; Liu, Y.-S.; Guo, J.; Drisdell, W. S.; Cooper, J. K.; Sharp, I. D., Electronic Structure, Optoelectronic Properties, and Photoelectrochemical Characteristics of γ-$Cu_3V_2O_8$ Thin Films. *Chemistry of Materials* **2017,** *29* (7), 3334-3345.

20. Hossain, M. K.; Sarker, H. P.; Sotelo, P.; Dang, U.; Rodríguez-Gutiérrez, I.; Blawat, J.; Vali, A.; Xie, W.; Oskam, G.; Huda, M. N.; Macaluso, R. T.; Rajeshwar, K., Phase-Pure Copper Vanadate (α-CuV_2O_6): Solution Combustion Synthesis and Characterization. *Chemistry of Materials* **2020,** *32* (14), 6247-6255.

21. Sameie, H.; Sabbagh Alvani, A. A.; Naseri, N.; Du, S.; Rosei, F., First-principles study on ZnV_2O_6 and $Zn_2V_2O_7$: Two new photoanode candidates for photoelectrochemical water oxidation. *Ceramics International* **2018,** *44* (6), 6607-6613.

22. Hong, S.; Doughty, R. M.; Osterloh, F. E.; Zaikina, J. V., Deep eutectic solvent route synthesis of zinc and copper vanadate n-type semiconductors – mapping oxygen vacancies and their effect on photovoltage. *Journal of Materials Chemistry A* **2019,** *7* (19), 12303-12316.

23. Wrighton, M. S.; Ellis, A. B.; Wolczanski, P. T.; Morse, D. L.; Abrahamson, H. B.; Ginley, D. S., Strontium titanate photoelectrodes. Efficient photoassisted electrolysis of water at zero applied potential. *Journal of the American Chemical Society* **1976,** *98* (10), 2774-2779.

24. Chen, X.; Liu, L.; Yu Peter, Y.; Mao Samuel, S., Increasing Solar Absorption for Photocatalysis with Black Hydrogenated Titanium Dioxide Nanocrystals. *Science* **2011,** *331* (6018), 746-750.

25. Wang, G.; Ling, Y.; Wang, H.; Yang, X.; Wang, C.; Zhang, J. Z.; Li, Y., Hydrogen-treated WO_3 nanoflakes show enhanced photostability. *Energy & Environmental Science* **2012,** *5* (3), 6180-6187.

26. Wang, G.; Ling, Y.; Lu, X.; Qian, F.; Tong, Y.; Zhang, J. Z.; Lordi, V.; Rocha Leao, C.; Li, Y., Computational and Photoelectrochemical Study of Hydrogenated Bismuth Vanadate. *The Journal of Physical Chemistry C* **2013,** *117* (21), 10957-10964.

27. Clarke, F. W.; Washington, H. S., *The composition of the earth's crust*. US Government Printing Office: 1924; Vol. 127.

28. Kim, J. H.; Kim, H. E.; Kim, J. H.; Lee, J. S., Ferrites: emerging light absorbers for solar water splitting. *Journal of Materials Chemistry A* **2020,** *8* (19), 9447-9482.

29. Matsumoto, Y.; Omae, M.; Sugiyama, K.; Sato, E., New photocathode materials for hydrogen evolution: calcium iron oxide ($CaFe_2O_4$) and strontium iron oxide ($Sr_7Fe_{10}O_{22}$). *The Journal of Physical Chemistry* **1987,** *91* (3), 577-581.

30. Ida, S.; Yamada, K.; Matsunaga, T.; Hagiwara, H.; Matsumoto, Y.; Ishihara, T., Preparation of p-Type $CaFe_2O_4$ Photocathodes for Producing Hydrogen from Water. *Journal of the American Chemical Society* **2010,** *132* (49), 17343-17345.

31. Kirchberg, K.; Marschall, R., Sol-gel synthesis of mesoporous $CaFe_2O_4$ photocathodes with hierarchical pore morphology. *Sustainable Energy & Fuels* **2019,** *3* (5), 1150-1153.

32. Bloesser, A.; Timm, J.; Kurz, H.; Milius, W.; Hayama, S.; Breu, J.; Weber, B.; Marschall, R., A Novel Synthesis Yielding Macroporous $CaFe_2O_4$ Sponges for Solar Energy Conversion. *Solar RRL* **2020,** *4* (8), 1900570.

33. Butler, M. A.; Ginley, D. S., Prediction of Flatband Potentials at Semiconductor-Electrolyte Interfaces from Atomic Electronegativities. *Journal of the Electrochemical Society* **1978,** *125* (2), 228-232.

34. Xu, Y.; Schoonen, M. A. A., The absolute energy positions of conduction and valence bands of selected semiconducting minerals. *American Mineralogist* **2000,** *85* (3-4), 543-556.

35. Takata, T.; Domen, K., Defect Engineering of Photocatalysts by Doping of Aliovalent Metal Cations for Efficient Water Splitting. *The Journal of Physical Chemistry C* **2009,** *113* (45), 19386-19388.

36. Zhao, Z.; Goncalves, R. V.; Barman, S. K.; Willard, E. J.; Byle, E.; Perry, R.; Wu, Z.; Huda, M. N.; Moulé, A. J.; Osterloh, F. E., Electronic structure basis for enhanced overall water splitting photocatalysis with aluminum doped $SrTiO_3$ in natural sunlight. *Energy & Environmental Science* **2019,** *12* (4), 1385-1395.

37. Moniz, S. J. A.; Blackman, C. S.; Southern, P.; Weaver, P. M.; Tang, J.; Carmalt, C. J., Visible-light driven water splitting over BiFeO3 photoanodes grown via the LPCVD reaction of $[Bi(OtBu)_3]$ and $[Fe(OtBu)_3]_2$ and enhanced with a surface nickel oxygen evolution catalyst. *Nanoscale* **2015,** *7* (39), 16343-16353.

38. Guijarro, N.; Bornoz, P.; Prévot, M.; Yu, X.; Zhu, X.; Johnson, M.; Jeanbourquin, X.; Le Formal, F.; Sivula, K., Evaluating spinel ferrites MFe_2O_4 (M = Cu, Mg, Zn) as photoanodes for solar water oxidation: prospects and limitations. *Sustainable Energy & Fuels* **2018,** *2* (1), 103-117.

39. Hufnagel, A. G.; Peters, K.; Müller, A.; Scheu, C.; Fattakhova-Rohlfing, D.; Bein, T., Zinc Ferrite Photoanode Nanomorphologies with Favorable Kinetics for Water-Splitting. *Advanced Functional Materials* **2016,** *26* (25), 4435-4443.

40. Kim, J. H.; Kim, J. H.; Jang, J.-W.; Kim, J. Y.; Choi, S. H.; Magesh, G.; Lee, J.; Lee, J. S., Awakening Solar Water-Splitting Activity of $ZnFe_2O_4$ Nanorods by Hybrid Microwave Annealing. *Advanced Energy Materials* **2015,** *5* (6), 1401933.

41. Zhang, M.; Ma, Y.; Friedrich, D.; van de Krol, R.; Wong, L. H.; Abdi, F. F., Elucidation of the opto-electronic and photoelectrochemical properties of $FeVO_4$ photoanodes for solar water oxidation. *Journal of Materials Chemistry A* **2018,** *6* (2), 548-555.

42. Lohaus, C.; Klein, A.; Jaegermann, W., Limitation of Fermi level shifts by polaron defect states in hematite photoelectrodes. *Nature Communications* **2018,** *9* (1), 4309.

43. Doughty, R. M.; Hodges, B.; Dominguez, J.; Han, R.; Zhao, Z.; Assavachin, S.; Osterloh, F. E., Fermi Level Pinning Controls Band Bending and Photochemical Charge Separation in Particles of n-$SrTiO_3$, n-$SrTiO_3$:Al, and n-GaAs:Te. *The Journal of Physical Chemistry C* **2020,** *124* (34), 18426-18435.

44. Gerischer, H., The impact of semiconductors on the concepts of electrochemistry. *Electrochimica Acta* **1990,** *35* (11), 1677-1699.

45. Gerischer, H., Electrochemical Behavior of Semiconductors under Illumination. *Journal of the Electrochemical Society* **1966,** *113* (11), 1174-1182.

46. Tablero, C., $CaFe_2O_4$ as a self-sufficient solar energy converter. *Journal of Applied Physics* **2017,** *122* (13), 133114.

47. Knyazev, Y. V.; Tarasov, A. S.; Platunov, M. S.; Trigub, A. L.; Bayukov, O. A.; Boronin, A. I.; Solovyov, L. A.; Rabchevskii, E. V.; Shishkina, N. N.; Anshits, A. G., Structural and electron transport

properties of $CaFe_2O_4$ synthesized in air and in helium atmosphere. *Journal of Alloys and Compounds* **2020,** *820*, 153073.

48. Tsipis, E. V.; Pivak, Y. V.; Waerenborgh, J. C.; Kolotygin, V. A.; Viskup, A. P.; Kharton, V. V., Oxygen ionic conductivity, Mössbauer spectra and thermal expansion of $CaFe_2O_{4-\delta}$. *Solid State Ionics* **2007,** *178* (25), 1428-1436.